



Predictive digitization, restoration and degradation assessment
of cultural heritage objects



D5.8 – Final Evaluation Report

Grant Agreement Number	600533
Project Acronym	PRESIOUS
Project Title	PREdictive digitization, reStoration and degradatIOn assessment of cultUral heritage objectS
Funding Scheme	Collaborative Project (STREP)
Final Evaluation Report	
Name, title and organisation of the scientific representative of the project's coordinator	T. Theoharis, Professor, NTNU
Telephone	+47 73591447
Email	theotheo@idi.ntnu.no
Project Website Address	www.presious.eu
Dissemination Level	PU

Address
Sem Sælands vei 5, Gamle fysikk 3rd floor
Gløshaugen, NTNU, NO-7491 Trondheim,
Norway

<http://presious.eu>

Contact person
Karelle Gilbert-Soni
karelle@ime.ntnu.no
+ 47 73591481

Deliverable Identification Sheet

Grant Agreement number	600533
Project Acronym	PRESIOUS
Project Title	PREdictive digitization, reStoration and degradatIOn assessment of cultUral her-itage objectS
Funding Scheme	Collaborative Project (STREP)
Contractual Delivery Date	M36
Deliverable Number	D5.8
Deliverable Name	Final Evaluation Report
Type	Document (L ^A T _E X)
Deliverable Version	1.8
Status	Initial
Associated WP / Task	WP5
Author(s)	<p>NTNU: Theoharis Theoharis, Christian Schellewald, Panagiotis Perakis, Konstantinos Sfikas, Kidane Fanta Gebremariam</p> <p>AUEB-RC: Anthousis Andreadis, Georgios Papaioannou, Pavlos Mavridis</p> <p>ATHENA RC: Ioannis Pratikakis, Fotis Arnaoutoglou, Michalis Savelonas, George Barlas, Pavlos Efraimidis, George Stamatiatos, Panagiotis Theologou, Konstantinos Zagoris</p> <p>UKON: Ivan Sipiran, Robert Gregor, Tobias Schreck</p> <p>BREUCKMANN GMBH: Dirk Rieke-Zapp</p>
Project Officer	Philippe Gelin
Abstract	This document contains the final evaluation report
Circulated to Participants	22. February, 2016
Read by Participants	29. February, 2016
Approved by General Assembly	29. February, 2016

Document Revision History

Date	Version	Author/Editor/Contributor	Summary of Changes
07.01.2016	1.0	Theoharis Theoharis	Very first version
29.01.2016	1.05	Robert Gregor, Ivan Sipiran, Tobias Schreck	Evaluation WP4 Task 4.2
09.02.2016	1.1	Panagiotis Perakis	WP3 Outline & first version
11.02.2016	1.15	Christian Schellewald	WP3 Common erosion
12.02.2016	1.2	Theoharis Theoharis	WP3 Proofreading & corrections
13.02.2016	1.25	Christian Schellewald	WP3 Stone Builder
15.02.2016	1.3	Panagiotis Perakis & Kidane Fanta Gebremariam	WP3 Inclusion of erosion experiments & results
25.02.2016	1.4	Panagiotis Perakis	WP3 Analysis of experimental data & results
29.02.2016	1.5	Panagiotis Perakis & Kidane Fanta Gebremariam	WP3 Proofreading & corrections
01.03.2016	1.6	Theoharis Theoharis	WP3 Proofreading & corrections
08.03.2016	1.7	Michalis Savelonas, Fotis Arnaoutoglou, Ioannis Pratikakis, Pavlos Mavridis	WP2 Draft, proofreading, corrections
23.05.2016	1.8	Panagiotis Perakis & Christian Schellewald	WP3 Proofreading & corrections

Contents

1	Evaluation of WP2	7
1.1	Partial retrieval (T2.1)	7
1.2	Model reshaping (T2.2)	10
1.2.1	Evaluation of symmetry-based completion	11
1.2.2	Evaluation of rigid registration	15
1.2.3	Evaluation of non-rigid registration	16
2	Evaluation of WP3	22
2.1	Evaluation Data	22
2.1.1	Data from the Cultural Heritage Sites	22
2.1.2	Data from Accelerated Erosion Experiments	23
2.1.3	Stone Slabs and Experiment Assignments	24
2.2	Measurement Modalities	28
2.2.1	3D Geometry Measurements	28
2.2.2	QEMSCAN	28
2.2.3	micro-CT	29
2.3	Computation of the Extent of Erosion	30
2.3.1	Mass Measurements	30
2.3.2	Geometric Mean Erosion Computations	31
2.3.3	Computing Mean Erosion Rates	34
2.3.4	Computing Erosion on every Vertex of the Stone Mesh	36
2.3.5	Physico-chemical Aspects of the Erosion	38

2.4	Modeling Erosion	45
2.4.1	Geometric Model of Erosion	46
2.4.2	Chemical Model of Erosion	47
2.4.3	Computing Rain Recession at the CH Sites	49
2.4.4	Equivalent Rain Height and Exposure Time Computations	50
2.4.5	Effects of Common Erosion	52
2.4.6	The Erosion Simulator Module	54
2.4.7	The Stone Builder Module	55
2.5	WP3 Evaluation Experiments and Results	56
2.5.1	Time Reversal	57
2.5.2	C-WP3-1. Erosion prediction geometric accuracy	57
2.5.3	C-WP3-2. Erosion prediction physico-chemical accuracy	65
2.5.4	C-WP3-3. Erosion prediction geometric robustness	65
2.5.5	C-WP3-4. Erosion prediction physico-chemical robustness	66
2.5.6	C-WP3-5. Erosion prediction tolerance against object geometric resolution and scale variations	66
2.5.7	C-WP3-6. Erosion prediction tolerance against object physico-chemical resolution and scale variations	68
2.5.8	C-WP3-7. Erosion prediction procedure complexity and absolute processing time evaluation	69
2.5.9	C-WP3-8. Stone Builder's synthetic stones consistency against real stone materials	70
2.5.10	Concluding Remarks	74
2.6	Deviations and Corrections with respect to WP3 Evaluation Plan	76
2.7	Open Problems and Further Work	77

3	Evaluation of WP4	80
3.1	Evaluation of Object Reassembly (Task 4.1)	80
3.1.1	Multi-part reassembly utilizing contact surface and f-curves	81
3.1.2	Symmetry-based reassembly	82
3.2	Evaluation of Object Repair (Task 4.2)	84
3.2.1	Object Fracturing Methodology and Implementation	84
3.2.2	Fragment Benchmark Based on Hampson Collection	87
3.3	Evaluation of Partial Shape Retrieval	88
3.3.1	Deviations and corrections with respect to WP4 task 4.2 evaluation plan	89
4	Evaluation of WP5	90
4.1	Reassembly Pipeline Evaluation	90
4.1.1	CH Expert's Feedback	90
4.1.2	VRMW Reassembly Improvements	91
4.1.3	Evaluation of the Feature Curve Extraction Process	92
4.2	Evaluation of the complete WP2 pipeline	96
4.2.1	Overall accuracy of predictive scanning tool	97
4.2.2	Efficiency of predictive digitization platform	98
4.2.3	Discussion by archaeologist	98

This document describes the final evaluation of the outcomes of WP2, WP3, WP4 and WP5 based on the Evaluation Plan (D5.1).

1 Evaluation of WP2

This section focuses on the evaluation of final-year developments on the individual modules of WP2. For further information on individual modules' methodologies and evaluation, the reader should refer to D2.4 (Predictive digitization methodology report) and D5.4 (First evaluation report).

1.1 Partial retrieval (T2.1)

In the following, we provide the overall retrieval performance obtained by the Fisher-based and the Panoramic-based method, for various experiments. In Table 1, we provide the retrieval performance on the Hampson pottery dataset, for 20 real queries obtained by the Microsoft Kinect V2 for Windows sensor. The corresponding PR curves for both methods are illustrated in Fig. 1. We also provide the retrieval performance of both methods on the Breuckmann Optoscan scanner. Table 2 presents the retrieval performance, as quantified by NN, FT, ST and DCG. Fig. 2 illustrates the average P-R scores. Finally, we provide the retrieval performance for artificial partial queries (Fig. 3 and Table 3), as well as on SHREC'2013 dataset for large-scale partial 3D object retrieval (Fig. 4 and Table 4).

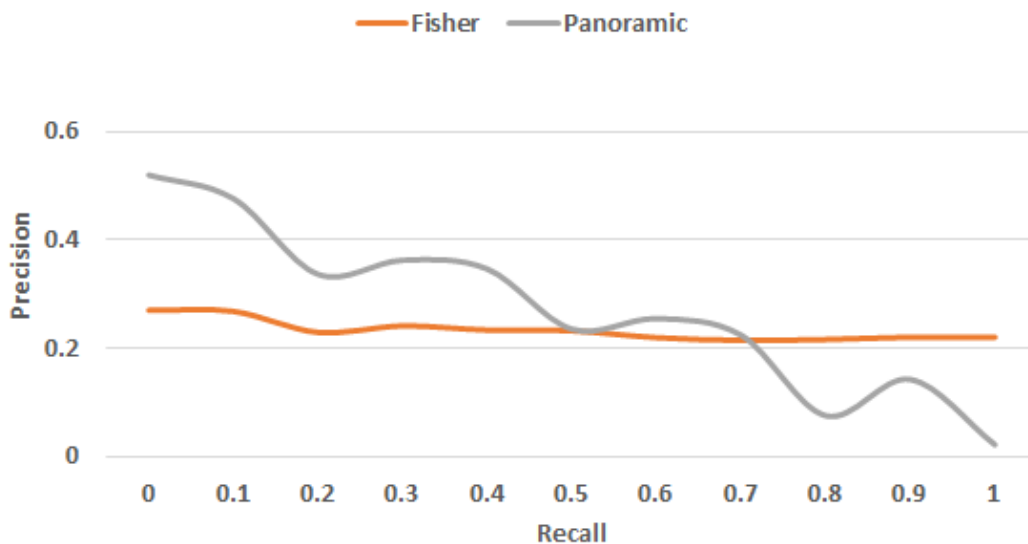


Figure 1: Average P-R for the Fisher-based and the Panoramic-based method on the Hampson pottery dataset, for 20 queries obtained by Microsoft Kinect V2 for Windows sensor.

Method	NN	FT	ST	DCG
Fisher	0.266	0.244	0.431	0.620
Panoramic	0.484	0.329	0.558	0.522

Table 1: Retrieval performance of the Fisher-based and the Panoramic-based method on the Hampson pottery dataset, with 20 real queries obtained by Microsoft Kinect V2 for Windows sensor.

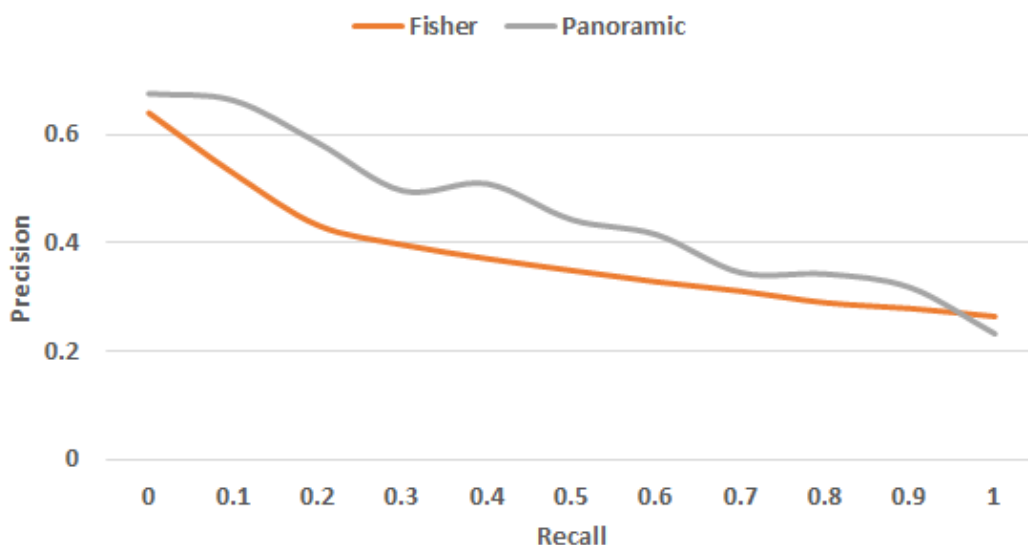


Figure 2: Average P-R for the Fisher-based and the Panoramic-based method applied on the Hampson pottery dataset, for 25 queries obtained by Breuckmann Optoscan scanner.

Method	NN	FT	ST	DCG
Fisher	0.641	0.351	0.554	0.712
Panoramic	0.663	0.363	0.606	0.733

Table 2: Retrieval results of the Fisher-based and the Panoramic-based method on the Hampson pottery dataset with 25 real queries obtained by Breuckmann Optoscan scanner.

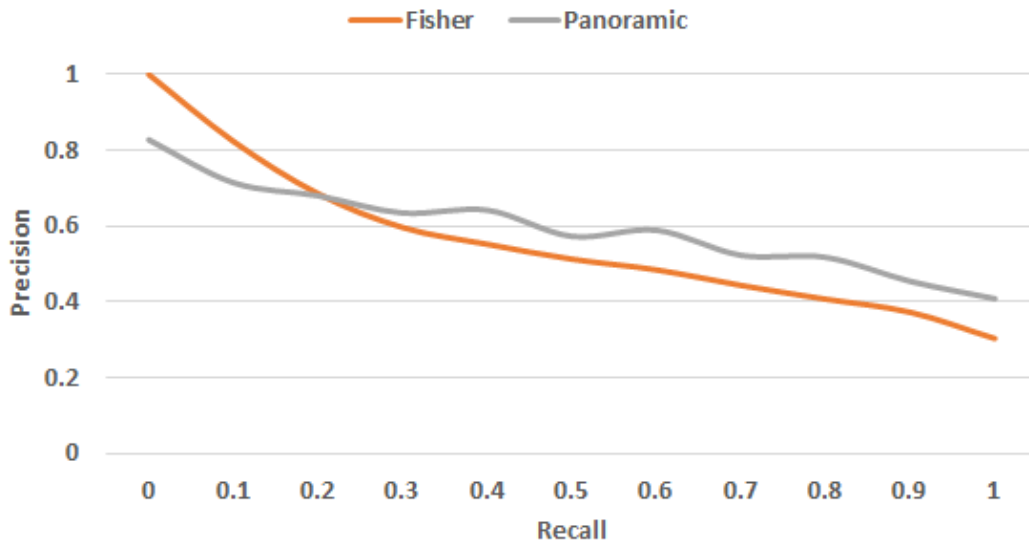


Figure 3: Average P-R for the Fisher-based and the Panoramic-based method applied on the Hampson pottery dataset, for artificial partial queries.

Method	NN	FT	ST	DCG
Fisher	1.000	0.492	0.702	0.827
Panoramic	0.838	0.457	0.685	0.787

Table 3: Average P-R for the Fisher-based and the Panoramic-based method applied on the Hampson pottery dataset, for artificial partial queries.

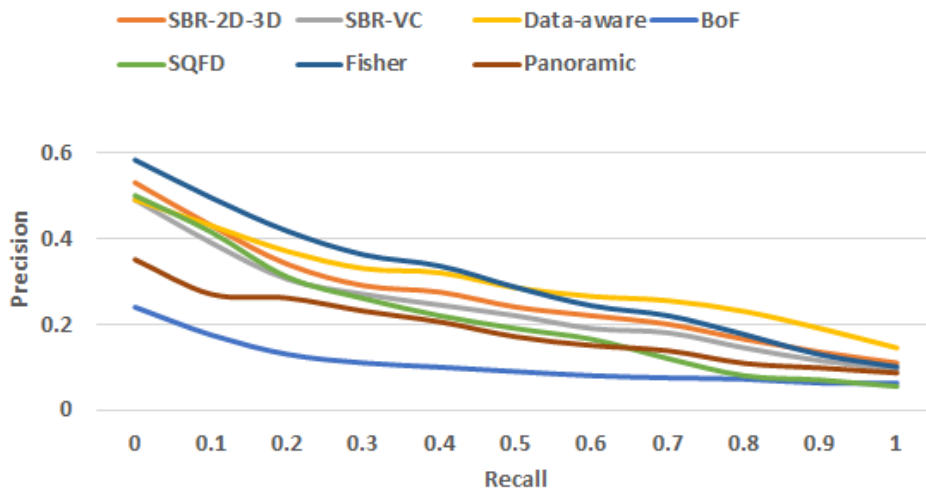


Figure 4: Average P-R for Fisher-based, Panoramic-based and 5 state-of-the-art retrieval methods on SHREC 2013 partial retrieval benchmark.

Method	NN	FT	ST	DCG
Fisher	0.3856	0.2772	0.2135	0.2851
Panoramic	0.3535	0.2290	0.1808	0.2455
SBR-2D-3D	0.2717	0.2016	0.1426	0.1754
SBR-VC	0.3218	0.2065	0.1638	0.2199
Data-aware	0.3457	0.2495	0.2088	0.2836
Polar spin images	0.0931	0.0809	0.0768	0.0968
SQFD	0.3108	0.2043	0.1576	0.1978

Table 4: The results of the Fisher-based and the Panoramic-based method, along with 5 state-of-the-art retrieval methods on SHREC 2013 partial retrieval benchmark.

1.2 Model reshaping (T2.2)

In this section we evaluate the individual components of the model reshaping module. This module takes as input a partial scan and provides a prediction of the complete object, using as reference a template object. The reshaping process takes place in several steps that are highlighted in Fig. 5. A detailed description of the algorithms used in this pipeline has been presented in the methodology report (D2.4).

In the remainder of this section we evaluate the performance and robustness of the main individual components on synthetic and real-world datasets. Please note that, since the first evaluation report (D5.4), new components have been introduced to the pipeline, such as the symmetry completion, and others have been vastly improved, therefore in this report we re-evaluate all components, to reflect the most recent advancements.

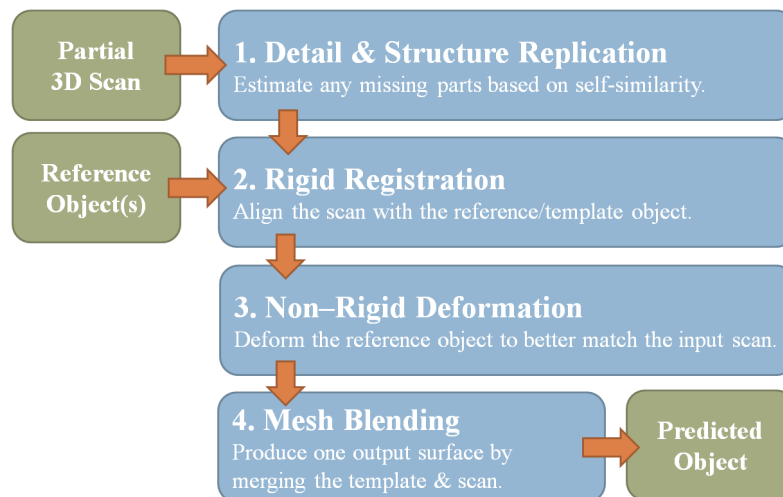


Figure 5: The overall reshaping pipeline. The detail and structure replication step is optional and is performed only for symmetrical objects.

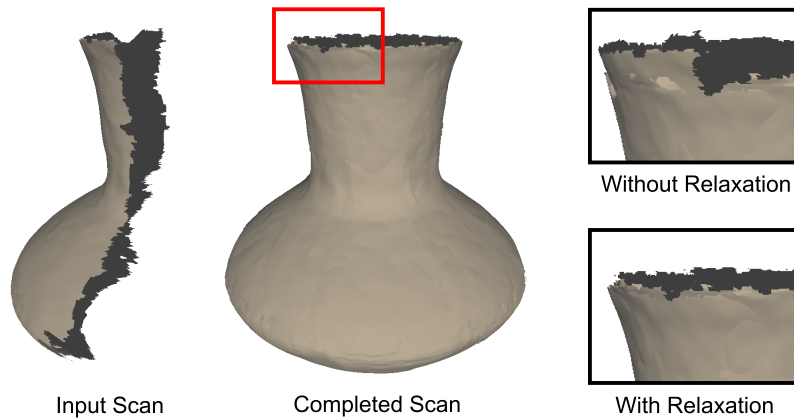


Figure 6: Completion of a pottery vessel from a single partial scan using our approach. After multiple iterations, alignment errors are accumulated and propagated in the replicated geometry. A global error relaxation approach (multi-view ICP) is used to improve the alignment.



Figure 7: Completion of a pottery vessel from a single partial scan. Even though the input scan covers only roughly 30% of the complete object, our approach detects the underlying rotational symmetry and successfully completes the missing geometry.

1.2.1 Evaluation of symmetry-based completion

In this section we demonstrate the effectiveness of the symmetry-based completion on partial 3D scans with varying levels of partiality. This step of the reshaping pipeline is optional and can be omitted when operating on non-symmetric objects.

In Fig. 6 and 7 we demonstrate the results of our algorithm in the completion of pottery vessels of various shapes from a single partial scan. The input partial scans cover only 20 to 30% of the complete object. Our algorithm properly detects the continuous rotational symmetry in the input objects and provides plausible completion results. It is worth noting that the completed pottery objects retain the details and irregularities of the input scans, which are not perfect surfaces of revolution. This completion approach for pottery objects is more general and provides more plausible

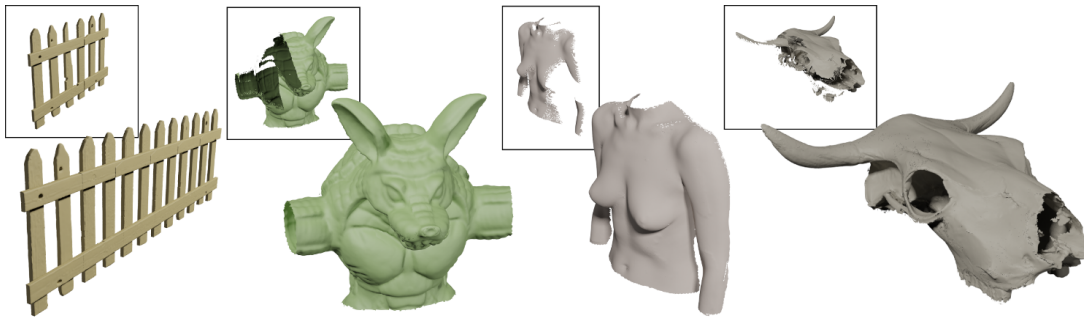


Figure 8: Completion of various partial objects using our method. The insets show the partial input shapes. Translational symmetry is used for the fence shape (three iterations), while the other examples use reflectional symmetry.

results than previous methods [CM02] that extract a profile curve and a symmetry axis from the input data and predict the missing shape using surfaces of revolution. Figure 8 demonstrates our method on the completion of various partial shapes. It should be noted that, while only the fence example uses a purely translational symmetry, even the rotational and reflectional examples include a translational component in the calculated partial symmetries, because the centroid of the incomplete input is not the same as the centroid of the complete shape.

Varying degrees of partiality

In Fig. 9 we test our method in the completion of a wheel-cap object with varying degrees of partiality. When operating with fewer data, more iterations are required by our algorithm to compute the final object and as a result, the accumulated registration errors are higher. This is reflected in the RMS error measurements against the ground truth object. In practice, even when only 25% of the desirable object is provided as input, our method provides plausible completion results. In the same figure we also provide a comparison with another symmetry-based completion method, proposed by Sipiran et al. [SGS14a]. This approach automatically detects and uses the highest scoring symmetry plane to complete the missing part of an object. For the 25% and 50% partiality cases, this method augments the input data, but the object is still not complete. In this case, a natural choice is to apply the algorithm iteratively, until the object is completed. However, by definition the resulting object after the first iteration is perfectly symmetric, thus the highest scoring symmetry plane cannot be used to further augment the available data and the method naturally fails. The same problem also prevents the algorithm from working on the 75% partiality case. It is clear that a symmetry plane with a lower score should be used. Our approach can automatically select such plane using the “*k*-sparse” constraint, without relying on user input. Furthermore, our approach is not limited to planar symmetry, and can properly perform the completion based on the rotational symmetry of the object.

Parameter sensitivity

Figure 10 explores the effect of parameter ϵ_t in the results. When operating on objects with prominent geometric corners and features, our method is not sensitive to the parameter ϵ_t . On the other hand, for smooth surfaces like pottery scans, the of ϵ_t

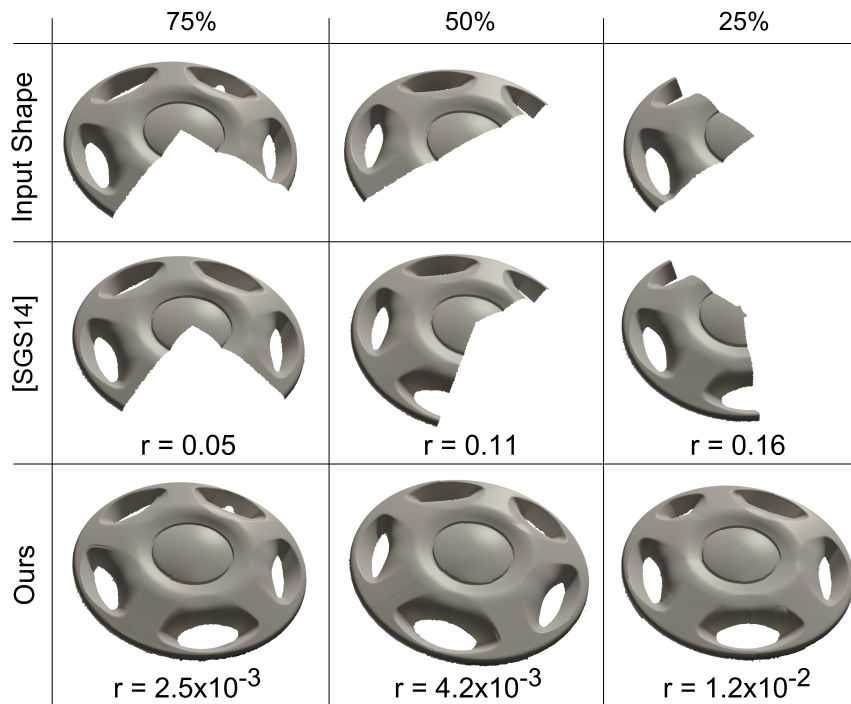


Figure 9: Completion of a partial wheel cap object with varying degrees of partiality and comparison with [SGS14a]. r denotes the Hausdorff RMS distance from the ground truth.

directly affects the number of iterations required to get the complete object, however it does not affect the quality of the final completed object.

Partial symmetry

Our algorithm can also handle and successfully complete partially symmetric objects, as the one shown in Fig. 11, where the vessel that we want to predict has a head figure in one side. When such prominent feature exists in the input object, the scanning should begin with this feature and the completion algorithm can successfully predict the rest of the object, which is symmetric.

Approximate symmetry

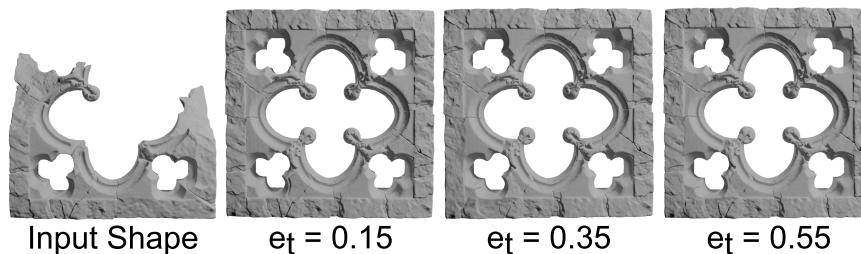


Figure 10: When operating on objects with prominent geometric corners and features, our method is not sensitive to the parameter $\epsilon_t \in [0, 1]$. For smooth objects, this parameter affects the number of iterations required to complete the object, without affecting the quality.

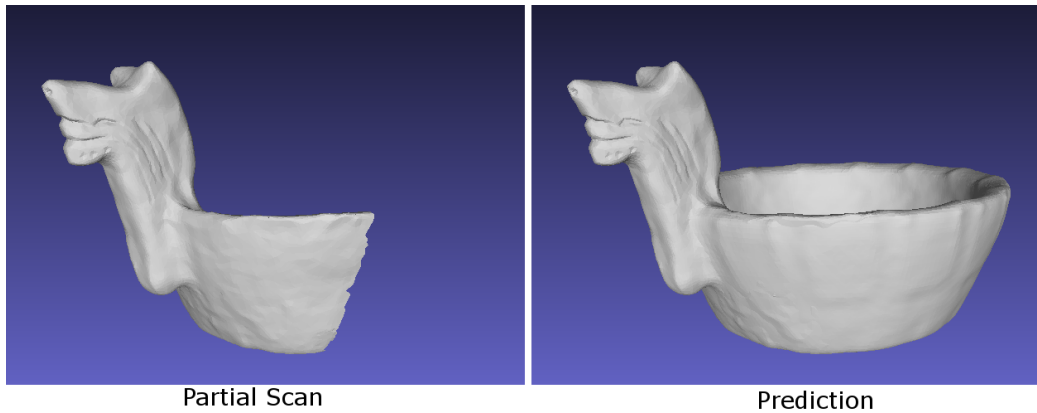


Figure 11: Completion of a partially symmetric object. In this case, the prominent feature should be present in the input scan, and the algorithm can successfully predict the rest of the shape.

Many natural or man-made objects exhibit an approximate symmetry, due to deviations in the biological growth, imprecisions in the manufacturing process or stochastic fluctuations in physical processes. A rigid symmetry transformation cannot be used to successfully complete such objects. To better handle these cases, our algorithm includes a non-rigid alignment step, which properly handles approximate symmetries, as demonstrated in Fig. 12.

Performance

When integrating our algorithm in the final prediction module, we have made some changes in the internal pipeline of the k-sparse symmetry completion, in order to speedup the algorithm and make it practical for interactive systems. In particular, the multi-view non-rigid registration step, which was proposed in the original publication describing the method, has been replaced with a more simple and efficient Poisson reconstruction.

After this change, the k-sparse symmetry detection requires from 6 to 20 seconds per object to detect the underlying symmetries. The exact time depends on the particular shape and the number of the underlying symmetries. It is worth noting that the pottery vessels in our tests are among the worst cases for our algorithm in terms of performance, due to the multiple candidate symmetries that should be tested. If we restrict our search to rotational symmetries along a vertical axis of rotation, which is the case for most pottery scans, then this process can be accelerated by roughly 40%.

The algorithm needs another 5 to 20 seconds to perform the Poisson reconstruction of the final surface from the multiple symmetrically replicated scans. The exact time depends of the quality and resolution of the final reconstructed mesh. The actual implementation has some additional overhead, due to disk I/O and some filtering and clean-up operations on the mesh.

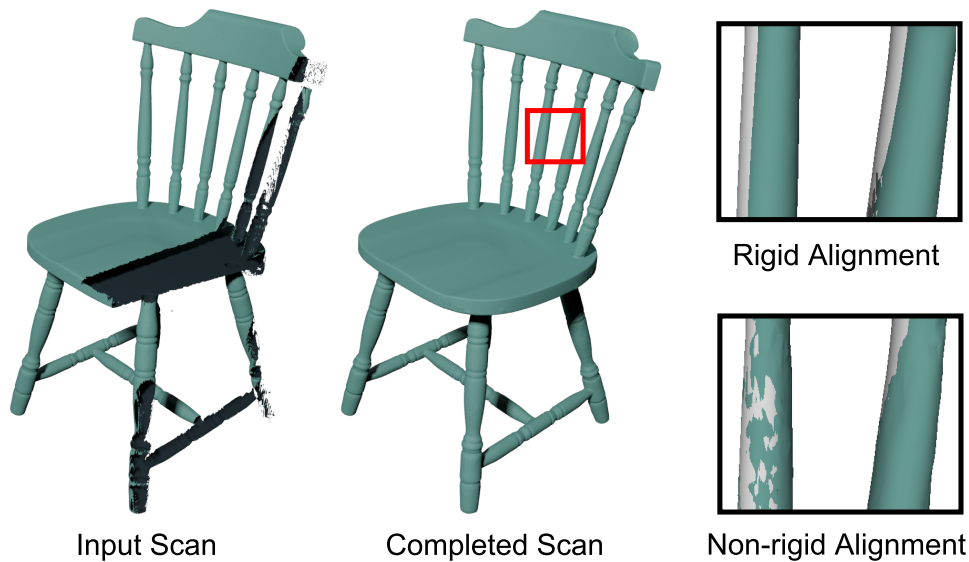


Figure 12: Completion of a partial chair object with our method. Many objects exhibit approximate symmetries, which create alignment errors in the replicated geometry. Our approach properly handles these cases using non-rigid registration.

1.2.2 Evaluation of rigid registration

Our rigid registration component, which is based on ℓ_p norm minimization, has not changed since the last evaluation report (D5.4). For completeness, we present some of the most significant results below. We have also included a discussion on how the inclusion of k-sparse affects the reliability of the rigid registration step. For a more complete evaluation of our rigid registration approach, the interested reader is referred to the relevant publications [MAP15a], [MAP15b] and the first evaluation report (D5.4).

Figure 13 presents a comparison of our registration method with Sparse ICP, in terms of robustness to source and destination outliers. In this experiment, random points have been inserted inside the bounding box of the source and target point clouds. Sparse ICP is known to be robust only to source outliers, therefore it fails to align the two point clouds properly. In contrast, our method demonstrates robustness to both source and destination outliers, and provides a reliable alignment between the two noisy datasets.

Figures 14, 15 and 16 demonstrate the robustness of our rigid registration method in the alignment of various challenging datasets of partially overlapping scans. In all cases our method provides a reliable alignment.

Implication of k-sparse in the rigid registration step It is worth noting that, when the k-sparse completion method is used in our pipeline (for symmetric objects), then the subsequent rigid alignment problem becomes significantly less challenging, because the amount of overlap between the source and the target surface becomes

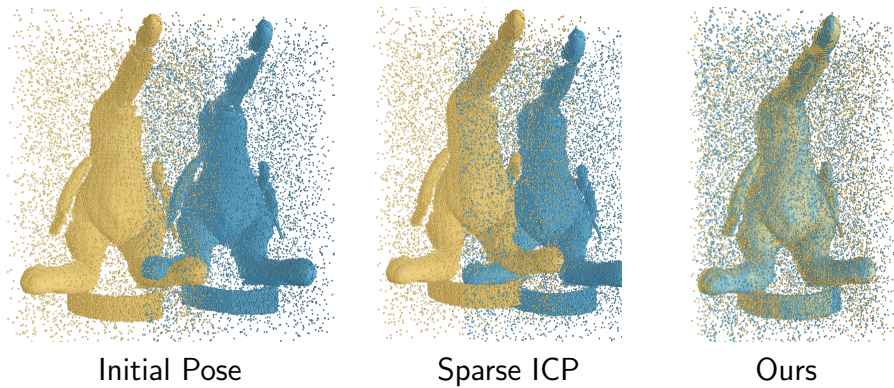


Figure 13: A comparison of our rigid-registration method with Sparse ICP in terms of robustness to source and destination outliers. Left: Initial position of the two surfaces. Middle: The original Sparse ICP method is known to be robust only to source outliers and in the presence of destination outliers the optimizer gets stuck to a suboptimal local minimum solution. Right: Our approach successfully aligns the two datasets, avoiding undesired local minima.

significantly higher. To this end, the amount of iterations used for the rigid registration can be reduced, improving the overall efficiency of our pipeline. Furthermore, the reliability is also improved, since partial scans with high overlap align much more reliably than scans with lower overlap.

1.2.3 Evaluation of non-rigid registration

In this section we evaluate the performance, quality and robustness of our non-rigid registration module when operating on various datasets. Since the first evaluation report, the rigidity constraints that are used during the optimisation process have been vastly improved and the correspondence determination heuristics have been also tuned in order to work better in our data.

Robustness

Non-rigid alignment problems become especially hard when the target mesh or point cloud is not perfect but contains holes and missing regions. Our algorithm is used a set of heuristics (bi-directional search) in order to determine these challenging cases, as shown in Fig. 17.

The grasping hand is a standard benchmarking dataset that is often used to test non-rigid registration algorithms. In our tests, we have made the test-case more challenging, by introducing holes and imperfections in the target mesh. The heuristic that we are using (bi-directional search) correctly identified these regions and provided a final mesh without any stretching. This is better demonstrated in Figure 18, where we examine the resulting point cloud with and without the use of the bi-directional heuristic.

Quality

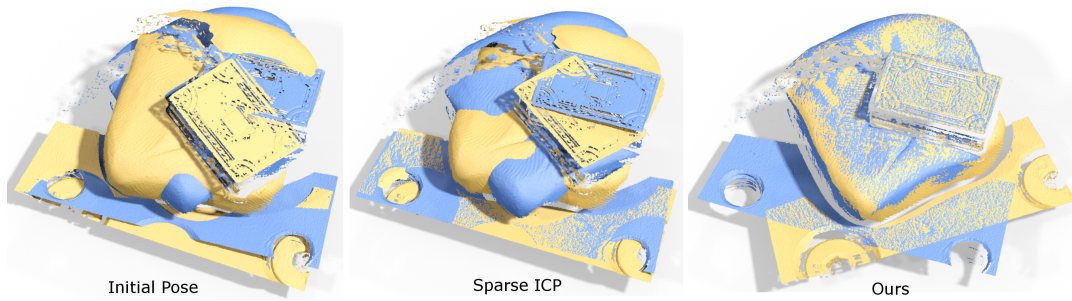


Figure 14: Rigid registration of two partially overlapping scans of a cultural heritage object. In this challenging registration problem, outliers inherently occur due to the partial overlap of the scans, especially at the edges of the scanner’s field of view. Furthermore, reflected light on polished surfaces is misread by the sensor, introducing additional outliers. Left: The input scans in their initial pose. Middle: Pairwise registration using Sparse ICP. The optimizer in this case is trapped in a local minimum, failing to align the book at the middle of the scene. Right: Pairwise registration using our method provides the desired alignment. 3D dataset courtesy of AICON 3D Systems.

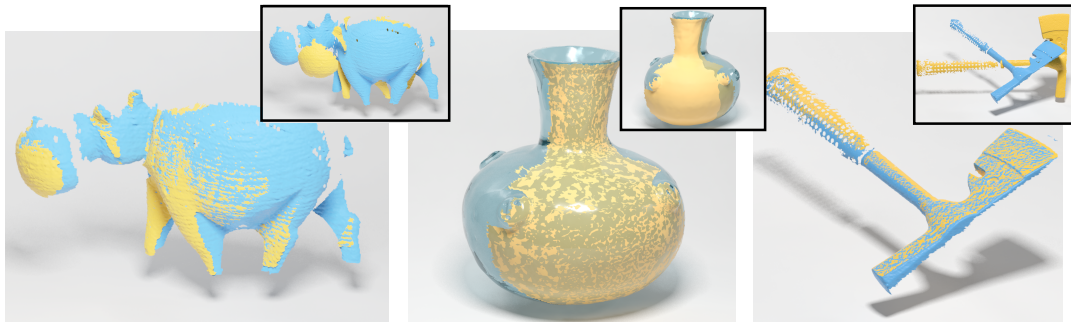


Figure 15: Rigid registration of various datasets computed with our method. Left: Registration of two partial scans with small overlap. Dataset from Mellado et al. [MAM14a]. Middle: A registration problem with many local minima, due to the rotational symmetry of the pottery object. Right: Registration of two partially overlapping scans of an axe. The insets show the initial position of the objects. The axe 3D dataset is courtesy of AICON 3D Systems.

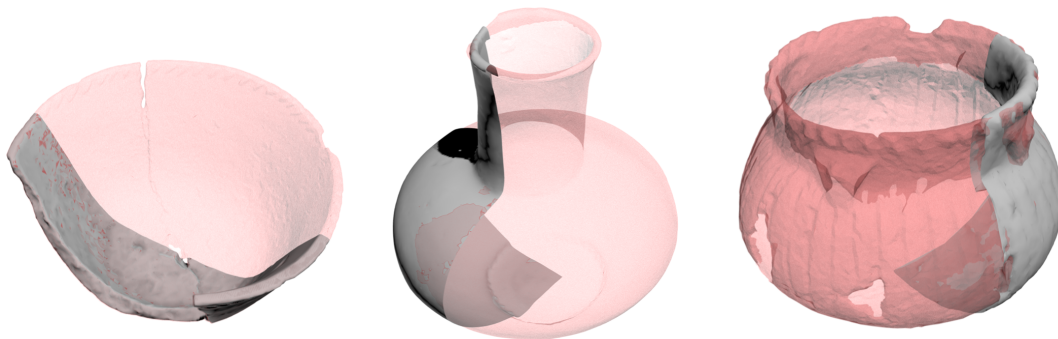


Figure 16: Alignment results using synthetic partial scans from the Virtual Hampson Museum dataset. The synthetic partial scans are shown as opaque and the complete template object is shown as transparent red.

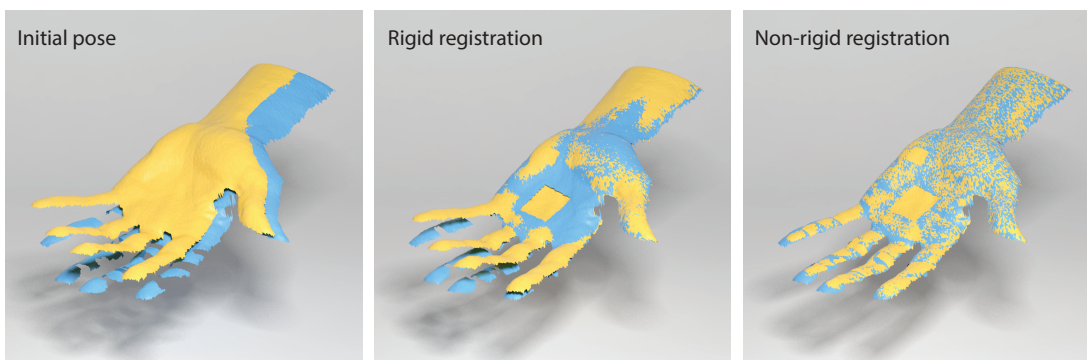


Figure 17: Our non-rigid registration applied to two frames of an animated grasping hand 3D capture, after rigid alignment. Artificial holes are also introduced to further stress this test case.

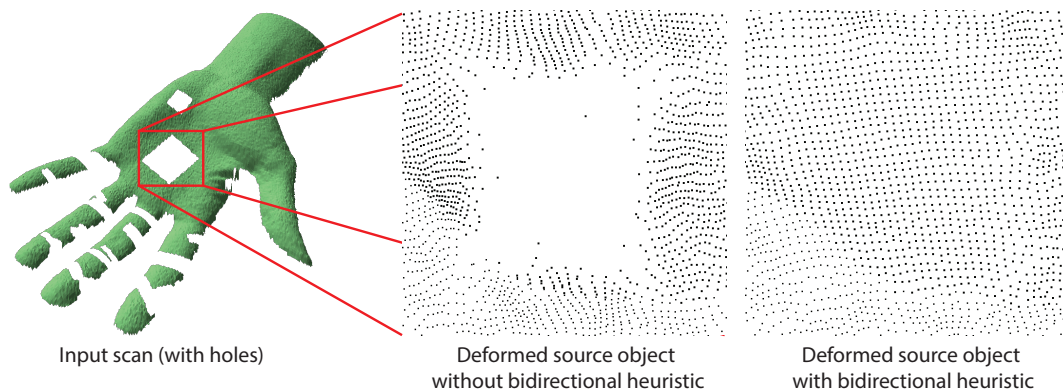


Figure 18: Bidirectional heuristic: Points that correspond to non-overlapping regions have a rigidity of one. Left: the input scan (target). Middle: without the bidirectional heuristic the deformed source is attracted to nearest points, even when source points overlap gaps on the target geometry. Right: correct handling of correspondences using the bidirectional heuristic.

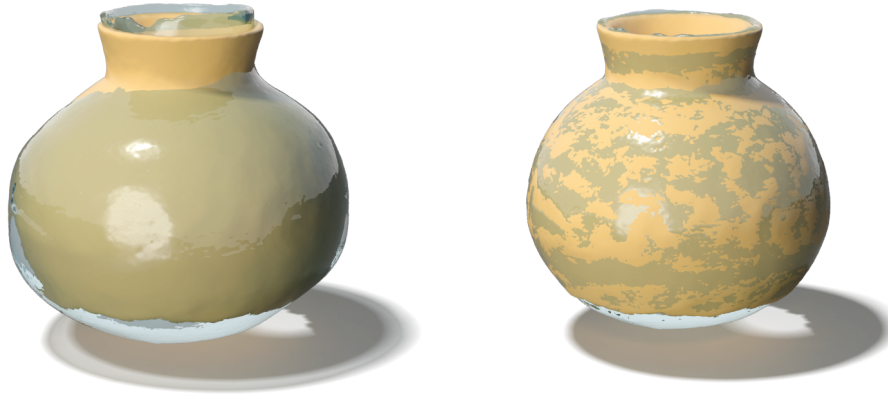


Figure 19: Left: Pair-wise rigid registration of two pots with different shape. The alignment is not perfect, since the pots have different shape. Right: Non-rigid registration of the same dataset results in a perfect alignment.

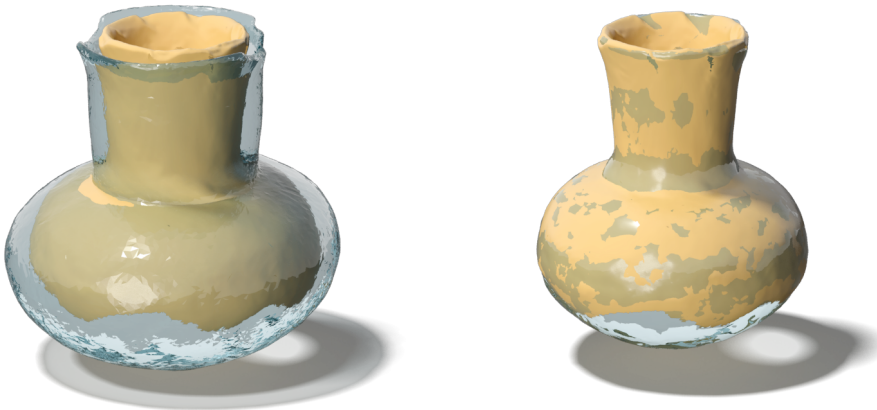


Figure 20: Another set of pots nearly perfectly aligned using initially rigid-registration (left) and afterwards our non-rigid algorithm (right).

Figures 19 and 20 demonstrate the quality of our non-rigid registration algorithm in some pottery datasets. In particular, the target meshes in these examples are outputs of the k -sparse symmetrical completion algorithm from the first stage in our pipeline. As we can see, k -sparse leaves large holes in the bottom of the objects, because the input partial scan does not cover and cannot provide any information about these regions. To this end, we use reference objects, that are deformed in order to complete the missing parts. These examples demonstrate that our deformation algorithm provides a perfect alignment between the source and target surfaces and the results are smooth and distortion-free.

Another interesting experiment was performed with a scan of the Ganymede statue at the Thorvaldsen Museum in Copenhagen. This high-detailed statue was placed close to a wall, so it was impossible to scan some regions at the back side of it. However, a less detailed version of the statue, with less detail could be freely scanned. We



Figure 21: Rigid and non-rigid registration of a high detail partial and a complete low detail version of it. Model courtesy of AICON.

have used our non-rigid registration algorithm to complete the missing regions of the high-detailed version, using the low-detailed version as a reference. Figure 21 demonstrates the results.

Performance

Figure 22 shows the scalability of the non-rigid registration process with relation to the number of points in the template object. For a template object with N vertices, our algorithm has to solve a linear optimisation problem with $3 \times N$ unknowns, so the run-time becomes prohibitively high for large datasets.

Sub-sampling Evaluation

In many of our experiments we are using high-detailed template objects. However, a direct application of the deformation algorithm in the high resolution mesh is impractical, as we have seen in Fig. 22. To this end, we apply the deformation on a uniformly sub-sampled version of the template mesh and then we transfer the deformation to the high-resolution version of the mesh, using interpolation. Figure 23 shows non-rigid registration results with varying levels of sub-sampling.

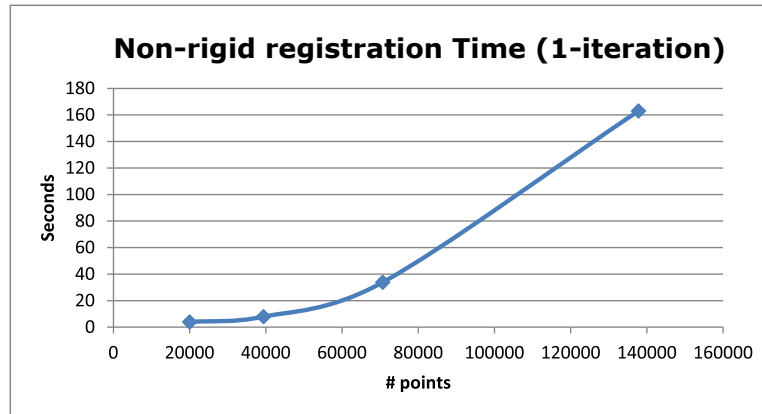


Figure 22: The performance of our non-rigid registration approach w.r.t. the number of points in the retrieved template object. The plot reflects the quadratic relation between the input points and the execution time. This is to be expected, since the computational complexity of our method is $O(n^2)$.

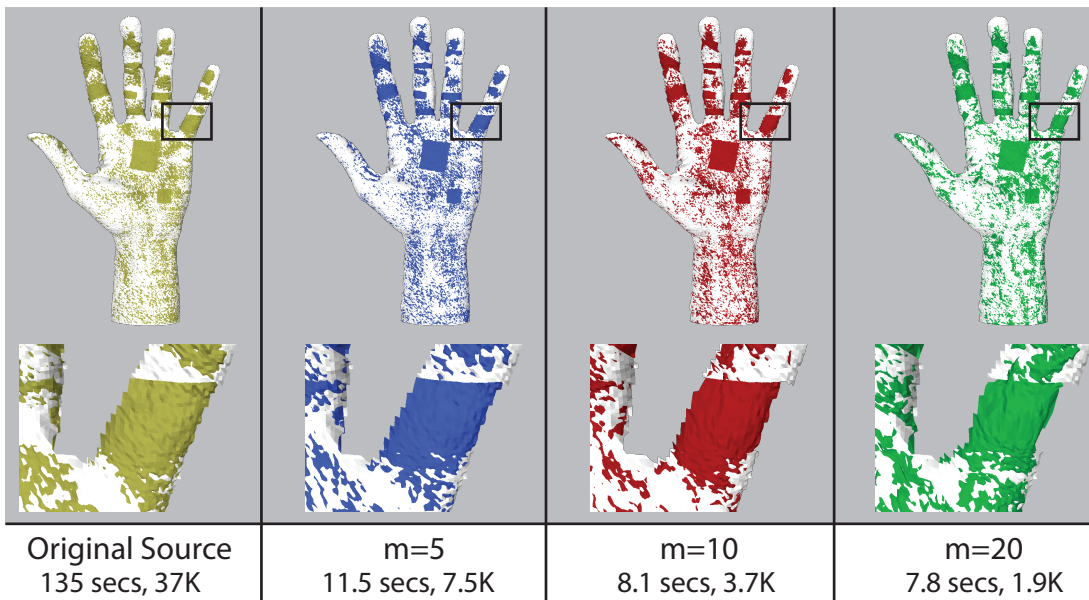


Figure 23: Non-rigid registration results with different levels of sub-sampling. For low values of m we notice substantial gains in performance with low distortions. For large values of m the distortion is easily spotted while the performance gains are smaller, due to the shift of the performance bottleneck.

2 Evaluation of WP3

2.1 Evaluation Data

2.1.1 Data from the Cultural Heritage Sites

For the investigation of the erosion mechanisms that contribute to the degradation of stones, we collected 3D geometric data from the two Cultural Heritage sites, the Demeter Sanctuary in Elefsis, Greece, and the Nidaros Cathedral in Trondheim, Norway (Figure 24). Figure 25 (b) shows the result mesh of the geometric scan of the Elefsis-pillar that took place at Elefsis in March 2013. The areas of the Elefsis-pillar, that are marked with boxes, indicate the patches we selected for illustration of measurements and investigations. The geometric scans were repeated in 2014 and 2015.



The Demeter Sanctuary
in Elefsis, Greece



The Nidaros Cathedral
in Trondheim, Norway

Figure 24: The two Cultural Heritage Monuments under study.

At the Nidaros Cathedral several smaller areas were selected for scanning. These include two wall parts from the Lectorium (Lectorium East, with Mason Marks, and Lectorium North) and two scans from the inside of the North West and South West Tower of the Cathedral. In Figure 25 (a) we illustrate the geometric scan of the east wall of the Lectorium that contains two mason marks. A close-up view of the area with a mason mark is depicted as well.

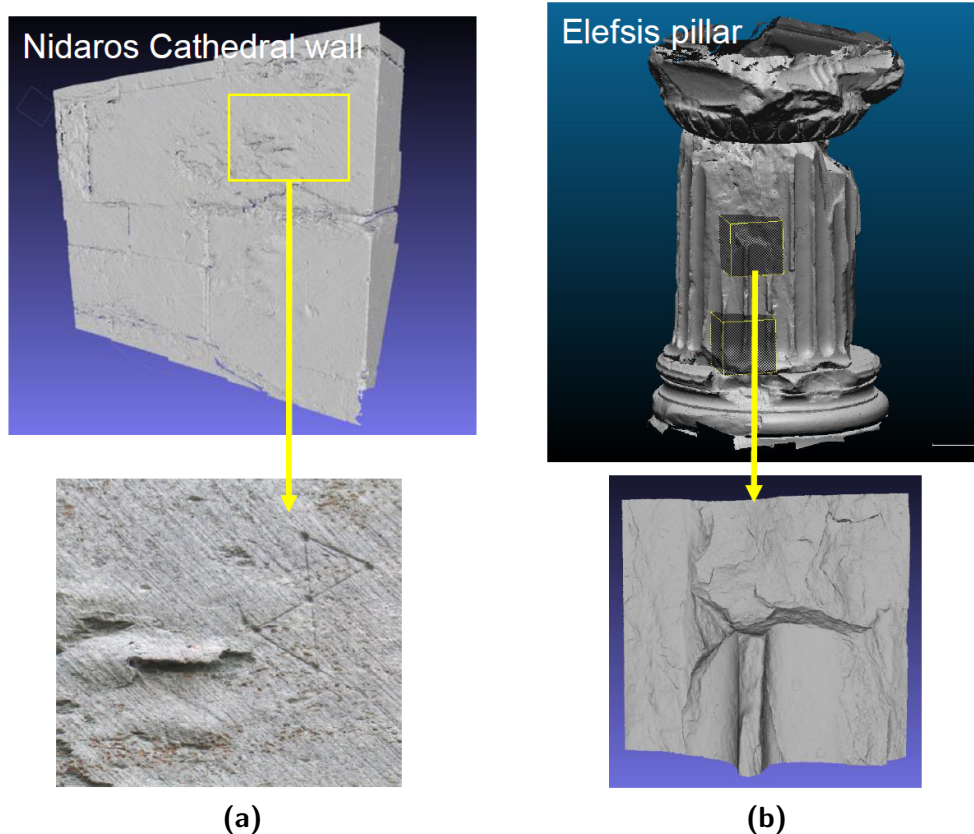


Figure 25: Scanned geometric meshes from the two Monuments. (a) The scanned Nidaros-wall and a patch showing in more detail the X mason mark that is present on the east wall of the Lectorium of the Nidaros Cathedral; (b) The scanned Elefsis-pillar and a patch showing in more detail the column area inside the upper box.

2.1.2 Data from Accelerated Erosion Experiments

The unavailability of chemical data and the small amount of recession observed at the Cultural Heritage sites themselves, made it necessary to complement these measurements with data obtained from accelerated erosion experiments, that study erosion parameters in isolation. Considered weathering experiments include effects that originate from polluted environments and from naturally occurring climatic conditions. The experiments that we finally decided to perform, include the Salt effect (using sodium sulfate Na_2SO_4), the Freeze-and-Thaw effect, that simulate mechanical effects and two chemical experiments simulating polluted industrial environments, rich in SO_2 and NO_2 (using aqueous solutions of sulfuric acid $\text{H}_2\text{SO}_4(\text{aq})$ and combined sulfuric and nitric acid $\text{H}_2\text{SO}_4+\text{HNO}_3(\text{aq})$).

In addition to the Salt and Freeze-and-Thaw weathering experiments, the acid weathering experiments were carried out to study the effects of polluting gases such as SO_2 and NO_2 in solution form. Cyclic soaking experiments in acidic solutions of sulfuric and nitric acids, with alternating wetting and drying stages, were used to simulate the accelerated weathering. Physico-chemical changes at macroscopic and microscopic

levels were monitored through characterizations using multiple analytical techniques.

The accelerated erosion experiments themselves are described in more detail in deliverable D1.2 (2nd Annual Project Review). Here we describe these experiments in a brief form with focus on the data obtained from the different measurement methods. Therefore in the next sections we provide a (non-exhaustive) list of the data we acquired so far.

2.1.3 Stone Slabs and Experiment Assignments

In this section we briefly describe the stone slabs and the performed erosion experiments. The stone slabs that were used in the experiments relate to stones that are similar to the ones used at the two Cultural Heritage sites. The stone samples that were used in the experiments carried out in our accelerated erosion chambers are stone slabs similar to the stones used at the two Cultural Heritage sites; the Demeter Sanctuary in Elefsis, Greece, and the Nidaros Cathedral in Trondheim, Norway (Figure 24). Pentelic marble was used at the Demeter Sanctuary [MBT*98] and Grytdal soapstone was used in the Nidaros Cathedral [Sto97].

Pentelic Marble: dense metamorphic rock; homogeneous; almost entirely made of calcite (96% $CaCO_3$); with low porosity (3.64 vol%) [MBT*98].

Grytdal Soapstone: dense metamorphic rock; non homogeneous; made mostly of chlorite (20% – 60%) and talc (5% – 20%); with low porosity (3.60 vol%) [Sto97].

The stone slabs were named according to their origin (Elefsis, Nidaros); furthermore the soapstone slabs labeled with reference to the stone quality (Good, Bad) and finally according to their size (Large, Small) (see Figure 26). Details concerning the labeling of the specific stone samples used in each of the erosion experiments are listed in Table 5.



Figure 26: Photos of some stone slabs used in the accelerated erosion experiments.

Experiments we finally decided to perform, include the Salt-effect (Na_2SO_4), the Freeze and Thaw effect and two chemical experiments simulating polluted environments ($\text{H}_2\text{SO}_4(\text{aq})$ and $\text{H}_2\text{SO}_4+\text{HNO}_3(\text{aq})$). Also, for a real on-site environmental erosion assessment we exposed some stone slabs on certain spots at the CH sites.

Stone Slabs		
Stone Slab	Material	Experiment
EL1	Elefsis Large 01	<i>Pentelic Marble</i>
EL2	Elefsis Large 02	<i>Pentelic Marble</i>
EL3	Elefsis Large 03	<i>Pentelic Marble</i>
ES1	Elefsis Small 01	<i>Pentelic Marble</i>
ES2	Elefsis Small 02	<i>Pentelic Marble</i>
ES3	Elefsis Small 03	<i>Pentelic Marble</i>
NBL1	Nidaros Bad Large 01	<i>Grytdal Soapstone</i>
NBL2	Nidaros Bad Large 02	<i>Grytdal Soapstone</i>
NBL3	Nidaros Bad Large 03	<i>Grytdal Soapstone</i>
NBS1	Nidaros Bad Small 01	<i>Grytdal Soapstone</i>
NBS2	Nidaros Bad Small 02	<i>Grytdal Soapstone</i>
NBS3	Nidaros Bad Small 03	<i>Grytdal Soapstone</i>
NGL1	Nidaros Good Large 01	<i>Grytdal Soapstone</i>
NGL2	Nidaros Good Large 02	<i>Grytdal Soapstone</i>
NGL3	Nidaros Good Large 03	<i>Grytdal Soapstone</i>
NGS1	Nidaros Good Small 01	<i>Grytdal Soapstone</i>
NGS2	Nidaros Good Small 02	<i>Grytdal Soapstone</i>
NGS3	Nidaros Good Small 03	<i>Grytdal Soapstone</i>

Table 5: Stone slabs labeling, material and associate experiment.

2.1.3.1 Acid Experiments For simulating acid rain in an accelerated weathering experiment two acidic conditions were selected: Sulfuric acid weathering (H_2SO_4) and combined Sulfuric/Nitric acid weathering ($\text{H}_2\text{SO}_4+\text{HNO}_3$); the first one to simulate the effects of acid rain due to SO_2 concentrations and the second one due to combined SO_2 and NO_2 concentrations. Each experiment consists of repeated cycles, so that in every cycle the stones are submerged for a prolonged time ($\approx 5 - 10$ days) in the chemical solutions and dried right afterwards (≈ 24 hours). The purpose of these periodic shocking experiments, with alternating wetting and drying steps, is to simulate accelerated acid weathering conditions.

Sulfuric Acid Experiment ($\text{H}_2\text{SO}_4(\text{aq})$) For this experiment an acid solution, H_2SO_4 , of pH 4 was prepared from reagent grade concentrated sulfuric acid. In each weathering container three samples from the same type of stone were totally immersed in the solution. The volumes of the solution V_{sol} for each group of identical stone types, Elefsis, Nidaros Good and Nidaros Bad, were 4 L each, kept in plastic containers of 7 L in size. The containers were closed during the soaking phase to minimize the effect of evaporation.

The stones were immersed in the solution with the pH adjusted at 4 on a daily basis. The weathering experiment was conducted at room temperature and humidity. The CO_2 level in the laboratory was continuously measured with a help of a data logger. In every experimental cycle, after 5 – 10 *days* intervals, the samples were taken out of the solution, and dried for 24 *hours* at 105°C in a desiccator and weighted afterwards. The stones after each experimental period were characterized by multi-analytical techniques. The combined Sulfuric/Nitric Acid erosion experiment has parameters that are shown in Table 6.

Parameters for the $\text{H}_2\text{SO}_4(\text{aq})$ Experiment					
Stone		duration <i>days</i>	num of cycles	V_{sol} <i>L</i>	pH
ES1	1 st <i>Period</i> (R01-R02)	45	4	4	4
	2 nd <i>Period</i> (R02-R03)	30	4	4	4
NBS1	1 st <i>Period</i> (R01-R02)	37	4	4	4
	2 nd <i>Period</i> (R02-R03)	30	4	4	4
NGS1	1 st <i>Period</i> (R01-R02)	42	3	4	4
	2 nd <i>Period</i> (R02-R03)	30	4	4	4

Table 6: Parameters for the $\text{H}_2\text{SO}_4(\text{aq})$ Experiment.

Combined Sulfuric/Nitric Acid Experiment ($\text{H}_2\text{SO}_4+\text{HNO}_3(\text{aq})$) The acid solution was prepared by mixing H_2SO_4 and HNO_3 solutions in the ratio of 2/3 and adjusting the pH to 4. The chemicals used are all reagent grade. The volumes of the solution V_{sol} for each group of identical stone types, Elefsis, Nidaros Good and Nidaros Bad, were 4 *L* each kept in a closed plastic container of 7 *L* in size. The containers were closed during the soaking phase to minimize the effect of evaporation.

The stones were immersed in the solution with the pH adjusted at 4 on a daily basis. The weathering experiment was conducted at room temperature and humidity. The CO_2 level in the laboratory was continuously measured with a help of a data logger. In every experimental cycle, after 5 – 10 *days* intervals, the samples were taken out of the solution, and dried for 24 *hours* at 105°C in a desiccator and weighted afterwards. The stones after each experimental period were characterized by multi-analytical techniques. The combined Sulfuric/Nitric Acid erosion experiment has parameters that are shown in Table 7.

2.1.3.2 Salt and Freeze-and-Thaw Experiments In order to investigate the Salt, and the Freeze-and-Thaw effects, we designed and constructed two erosion chambers for accelerated erosion experiments. They are controlled by Arduino micro-controllers [Ard15] and continuous measurements are taken over USB connections.

Parameters for the H ₂ SO ₄ +HNO ₃ (aq) Experiment					
Stone		duration <i>days</i>	num of cycles	<i>V_{sol}</i> <i>L</i>	pH
EL3	1 st Period (R01-R02)	41	4	4	4
	2 nd Period (R02-R03)	24	4	4	4
NBL3	1 st Period (R01-R02)	41	4	4	4
	2 nd Period (R02-R03)	24	4	4	4
NGL3	1 st Period (R01-R02)	41	4	4	4
	2 nd Period (R02-R03)	24	4	4	4

Table 7: Parameters for the H₂SO₄+HNO₃(aq) Experiment.

Salt Experiment The Salt Chamber is constructed out of a small Plexiglas box which contains the salt solution and a suspended base which can be submerged into the solution and raised out of it automatically. The stones are placed on the suspended base. Small fans are used for drying the stones as long as they are out of the solution.

One cycle within the Salt Chamber takes 6 *hours* and consists of submerging the stones in the salt solution, of Na₂SO₄ decahydrate, for 3 *hours* and drying them for 3 *hours* in a constant light airflow created by the fans attached to the chamber. Note that 3 *hours* is approximately the amount of time taken for the chambers to enter into a steady state of humidity variation. The temperature and humidity of the chamber are continuously monitored over the lifetime of the experiments. The accelerated Salt effect erosion experiment has parameters that are shown in Table 8.

Parameters for the Salt Experiment						
Stone		duration <i>days</i>	num of cycles	cycle <i>sec</i>	wetting <i>sec</i>	drying <i>sec</i>
EL2	1 st Period (R01-R02)	32	128	21,600	10,800	10,800
	2 nd Period (R02-R03)	16	64	21,600	10,800	10,800
NBL2	1 st Period (R01-R02)	32	128	21,600	10,800	10,800
	2 nd Period (R02-R03)	16	64	21,600	10,800	10,800
NGL2	1 st Period (R01-R02)	32	128	21,600	10,800	10,800
	2 nd Period (R02-R03)	16	64	21,600	10,800	10,800

Table 8: Parameters for the Salt Experiment.

Freeze-and-Thaw Experiment The Freeze-and-Thaw Chamber is constructed out of a small refrigerator and a water purification system. The stones are placed in a compartment inside the refrigerator, covered with a rain basin which is supplied with purified water to simulate rain drops falling. The whole system is controlled by an Arduino micro-controller. A separate Arduino micro-controller is used for continuously measuring the temperature.

One cycle within the Freeze-and-Thaw Chamber takes 8 *hours*. This includes 3 *hours* of freezing and 5 *hours* of warming up. The length of the warm cycle was selected so that the chamber reaches a temperature of about 5°C. The freezing cycle guarantees a long state where the temperature is below –5°C. Within the last 30 *minutes* of the warming phase, purified water drops onto the stones. The accelerated Freeze-and-Thaw erosion experiment has parameters that are shown in Table 9.

Parameters for the Freeze-and-Thaw Experiment							
Stone		duration <i>days</i>	num of cycles	cycle <i>sec</i>	warming <i>sec</i>	raining <i>sec</i>	freezing <i>sec</i>
EL1	1 st <i>Period</i> (R01-R02)	24	72	28,800	18,000	1,800	10,800
	2 nd <i>Period</i> (R02-R03)	56	168	28,800	18,000	1,800	10,800
NBL1	1 st <i>Period</i> (R01-R02)	24	72	28,800	18,000	1,800	10,800
	2 nd <i>Period</i> (R02-R03)	56	168	28,800	18,000	1,800	10,800
NGL1	1 st <i>Period</i> (R01-R02)	24	72	28,800	18,000	1,800	10,800
	2 nd <i>Period</i> (R02-R03)	56	168	28,800	18,000	1,800	10,800

Table 9: Parameters for the Freeze-and-Thaw Experiment.

2.2 Measurement Modalities

Several measurement techniques are used to characterize the changes that occur on the stone samples during the accelerated erosion cycles. The measurements consist of mass measurements, 3D Geometric Scans, Quantitative Evaluation of Minerals by SCANNing electron microscopy (QEMSCAN), Scanning Electron Microscopy with X-ray microanalysis (SEM-EDS), 3D microscopy, micro Computed Tomography (micro-CT), X-Ray Diffraction (XRD) and Petrography. Below we summarize the data sets collected from these measurements that were also exploited for the evaluation, benchmarking and operation of the erosion simulator, excluding data sets used solely for the chemical characterization and analysis of the erosion process.

2.2.1 3D Geometry Measurements

The 3D scans of the stone slabs in high resolution surface meshes of the 3D geometry of the stones, were performed by Aicon – our industrial partner in the PRESIOUS project – using a Breuckmann Scanner [AIC15]. An example of the resulting mesh data is depicted in Figure 27.

2.2.2 QEMSCAN

Quantitative Evaluation of Minerals by SCANNing electron microscopy is a technique that uses a Scanning Electron Microscope (SEM) combined with X-ray spectroscopy

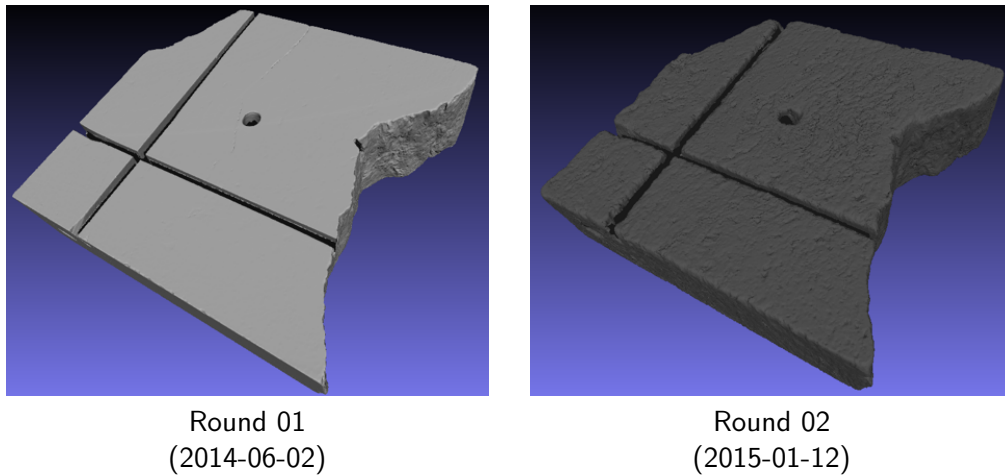


Figure 27: Depiction of the 3D scans of the Nidaros Bad Large 02 stone slab; Notice the roughness of the surface of the Round 02 scan compared to that of Round 01 due to the erosion.

and a database to obtain accurate mineral maps for a measured stone surface, performed by Robertson CGG [Rob15]. The results of the QEMSCAN of some of the stone slabs is shown in Figure 28. The used color codes and labeling of the mineral map is also depicted.

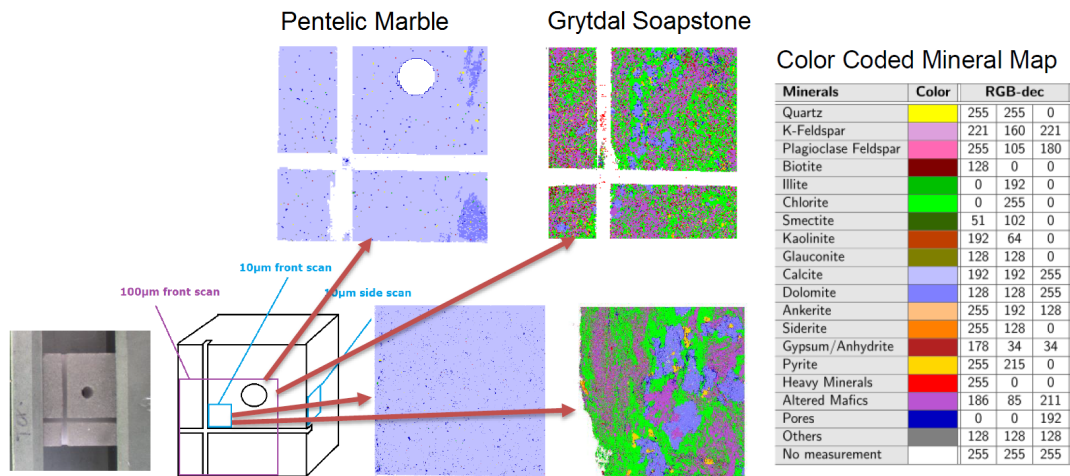


Figure 28: Depiction of the mineral maps from the QEMSCAN of “Pentelic Marble” and “Grytdal Soapstone” stone slabs; Table of color codes of minerals that appear in the QEMSCAN mineral maps.

2.2.3 micro-CT

Micro computed tomography is a technique similar to the well known CT scans performed in medicine. It provides x-ray images in 3D for small scale objects at a high resolution. It provides density information about the inner structure of the stone

material and could be helpful when analyzing the 3D pore structure and volume changes of the stones. Figure 29 shows a slice from the micro-CT data acquired for the “Nidaros Bad Large 2” stone slab.

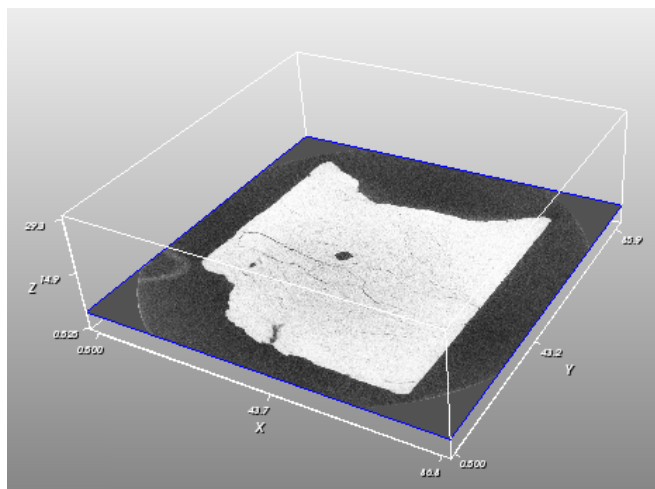


Figure 29: Depiction of a slice from the micro-CT data of “NBL2” stone slab.

2.3 Computation of the Extent of Erosion

2.3.1 Mass Measurements

After removal of the samples from the Salt Chamber, the stone samples were rinsed thoroughly with deionized water, dried for *24 hours* at 105°C and cooled to room temperature in a desiccator before mass measurements. The same procedure, except rinsing with deionized water, was followed for the stone samples from the Freeze-and-Thaw Chamber. For the Acid Chambers, the samples were taken out of the solution, dried for *24 hours* at 105°C and cooled to room temperature in a desiccator before weighting.

Mass measurements from both Rounds 01/02 and 02/03 confirm our intuition that stones suffer more erosion, under the specific experimental conditions, in the following order:

$$\textit{Nidaros Good} < \textit{Marble} < \textit{Nidaros Bad}$$

. Also the order of effectiveness of the erosion cause, under the specific experimental conditions, is the following:

$$\textit{Freeze - Thaw} < \textit{Acid H}_2\text{SO}_4 + \textit{HNO}_3(\textit{aq}) < \textit{Acid H}_2\text{SO}_4(\textit{aq}) < \textit{Salt}$$

Note that the Salt effects are more dramatic than the Freeze-Thaw effects, even worse than the Acidic effects, and Nidaros Bad is the most sensitive stone type (see Tables 10 and 11).

Mass Loss Δm (gr)				
Stone	m_1 gr	m_2 gr	Δm gr	$\Delta m/m$ %
EL1 <i>Freeze – Thaw</i>	29.1283	29.0847	-0.0436	-0.15
EL2 <i>Salt</i>	25.0409	24.8459	-0.1950	-0.78
EL3 <i>Acid H₂SO₄+HNO₃(aq)</i>	27.7475	27.5328	-0.2147	-0.77
ES1 <i>Acid H₂SO₄(aq)</i>	27.8519	27.5989	-0.2530	-0.91
NBL1 <i>Freeze – Thaw</i>	169.2780	168.8975	-0.3805	-0.22
NBL2 <i>Salt</i>	195.8884	188.9025	-6.9859	-3.57
NBL3 <i>Acid H₂SO₄+HNO₃(aq)</i>	140.1745	139.3690	-0.8055	-0.57
NBS1 <i>Acid H₂SO₄(aq)</i>	29.9790	29.6084	-0.3706	-1.24
NGL1 <i>Freeze – Thaw</i>	101.7920	101.7464	-0.0456	-0.04
NGL2 <i>Salt</i>	161.2788	160.5487	-0.7301	-0.45
NGL3 <i>Acid H₂SO₄+HNO₃(aq)</i>	143.4905	143.2244	-0.2661	-0.19
NGS1 <i>Acid H₂SO₄(aq)</i>	20.7092	20.6273	-0.0819	-0.40

Table 10: Measurements of the mass loss for the different stone slabs; m_1 initial mass (Round 01) and m_2 final mass (Round 02) of 1st accelerated erosion period.

Mass Loss Δm (gr)				
Stone	m_2 gr	m_3 gr	Δm gr	$\Delta m/m$ %
EL1 <i>Freeze – Thaw</i>	29.0847	29.0739	-0.0108	-0.04
EL2 <i>Salt</i>	24.8459	24.7049	-0.1410	-0.57
EL3 <i>Acid H₂SO₄+HNO₃(aq)</i>	27.5131	27.4734	-0.0397	-0.14
ES1 <i>Acid H₂SO₄(aq)</i>	27.5872	27.5156	-0.0716	-0.26
NBL1 <i>Freeze – Thaw</i>	168.8975	168.0539	-0.8436	-0.50
NBL2 <i>Salt</i>	188.9025	179.8329	-9.0696	-4.80
NBL3 <i>Acid H₂SO₄+HNO₃(aq)</i>	138.7807	138.3482	-0.4325	-0.31
NBS1 <i>Acid H₂SO₄(aq)</i>	29.5553	29.4115	-0.1438	-0.49
NGL1 <i>Freeze – Thaw</i>	101.7464	101.6972	-0.0492	-0.05
NGL2 <i>Salt</i>	160.5487	159.4037	-1.1450	-0.71
NGL3 <i>Acid H₂SO₄+HNO₃(aq)</i>	143.1609	143.1279	-0.0330	-0.02
NGS1 <i>Acid H₂SO₄(aq)</i>	20.6227	20.5998	-0.0229	-0.11

Table 11: Measurements of the mass loss for the different stone slabs; m_2 initial mass (Round 02) and m_3 final mass (Round 03) of 2nd accelerated erosion period.

2.3.2 Geometric Mean Erosion Computations

Computing mean erosion using Cubic Volume approximations One way of computing the mean erosion δ is to assume that the erosion takes place evenly on all faces of the slab and that the slab can be approximated as a cube of edge h . Then $\delta = \frac{1}{2}\Delta h$.

Thus, for computing Δh we use the volumes V_1 and V_2 of the slab before and after erosion respectively and assume that erosion took place equally in all directions and that the volume of the slab is cubical. Then Δh is computed from the slab volumes as $\Delta h = \sqrt[3]{V_2} - \sqrt[3]{V_1} = h_2 - h_1$, where h_1 and h_2 represent the cube edge lengths before and after erosion respectively. The volumes V_1 and V_2 were computed using non-void voxels counting on the micro-CT scans of the slabs.

Computing mean erosion using Volume and Surface Area approximations

Another way of computing the mean erosion rate δ is to use the surface areas S_1 and S_2 of the mesh and the corresponding volumes V_1 and V_2 of the stone slabs before and after erosion respectively. Assuming that the surface area doesn't change too much we can use the differential equation $\Delta V = S\Delta h$, and have

$$\delta = \Delta V/S, \quad (1)$$

where $\delta = \Delta h$, $\Delta V = V_2 - V_1$ and $S = S_{avg} = (S_1 + S_2)/2$.

The surface areas S were computed using the summation of the triangles area of the scanned mesh. The volumes V_1 and V_2 were computed counting the non-void voxels of the micro-CT scans of the slabs.

Mean Erosion δ (mm)						
Stone	V_1 cm^3	V_2 cm^3	ΔV cm^3	S cm^2	$\delta^{(a)}$ mm	$\delta^{(b)}$ mm
EL1 <i>Freeze – Thaw</i>	10.8250	10.7281	-0.0969	31.3598	-0.0331	-0.0309
EL2 <i>Salt</i>	9.3050	9.1773	-0.1277	28.3975	-0.0483	-0.0450
EL3 <i>Acid H₂SO₄+HNO₃(aq)</i>	10.2961	10.1391	-0.1570	29.7689	-0.0556	-0.0527
ES1 <i>Acid H₂SO₄(aq)</i>	10.3216	10.1510	-0.1706	29.9718	-0.0603	-0.0569
NBL1 <i>Freeze – Thaw</i>	61.9314	61.7922	-0.1392	120.5537	-0.0148	-0.0115
NBL2 <i>Salt</i>	70.3382	68.6979	-1.6403	126.5692	-0.1617	-0.1296
NBL3 <i>Acid H₂SO₄+HNO₃(aq)</i>	49.6610	50.6684	1.0074	97.4351	0.1234	0.1034
NBS1 <i>Acid H₂SO₄(aq)</i>	10.8753	11.1004	0.2251	32.9741	0.0759	0.0683
NGL1 <i>Freeze – Thaw</i>	35.4548	35.4389	-0.0159	72.1983	-0.0025	-0.0022
NGL2 <i>Salt</i>	55.5347	55.2833	-0.2514	102.9147	-0.0288	-0.0244
NGL3 <i>Acid H₂SO₄+HNO₃(aq)</i>	49.2560	49.3007	0.0447	103.6453	0.0055	0.0043
NGS1 <i>Acid H₂SO₄(aq)</i>	7.1383	7.1294	-0.0089	24.6578	-0.0040	-0.0036

Table 12: Estimations of Erosion δ by Volume and Surface Area computations: (a) Cubic approximation; and (b) Surface area approximation; V_1 initial volume (Round 01) and V_2 final volume (Round 02) of 1st accelerated erosion period.

We have computed the mean erosion δ using the previously described methods for the first period of accelerated experiments (Round 01 to Round 02) and for the second period of accelerated experiments (Round 02 to Round 03). The results for the various slabs are presented in Tables 12, 13.

Mean Erosion δ (mm)						
Stone	V_2 cm^3	V_3 cm^3	ΔV cm^3	S cm^2	$\delta^{(a)}$ mm	$\delta^{(b)}$ mm
EL1 <i>Freeze – Thaw</i>	10.7281	10.6283	-0.0998	31.1203	-0.0343	-0.0321
EL2 <i>Salt</i>	9.1773	9.1590	-0.0183	28.3975	-0.0070	-0.0064
EL3 <i>Acid H₂SO₄+HNO₃(aq)</i>	10.1391	10.1575	0.0184	29.7689	0.0065	0.0062
ES1 <i>Acid H₂SO₄(aq)</i>	10.1510	10.1497	-0.0013	29.9718	-0.0005	-0.0004
NBL1 <i>Freeze – Thaw</i>	61.7922	61.9740	0.1818	120.4163	0.0194	0.0151
NBL2 <i>Salt</i>	68.6979	66.6648	-2.0331	125.6727	-0.2040	-0.1618
NBL3 <i>Acid H₂SO₄+HNO₃(aq)</i>	50.6684	51.5121	0.8437	98.0255	0.1021	0.0861
NBS1 <i>Acid H₂SO₄(aq)</i>	11.1004	11.2041	0.1037	32.9741	0.0346	0.0314
NGL1 <i>Freeze – Thaw</i>	35.4389	35.0046	-0.4343	71.9148	-0.0674	-0.0604
NGL2 <i>Salt</i>	55.2833	55.1410	-0.1423	102.5810	-0.0164	-0.0139
NGL3 <i>Acid H₂SO₄+HNO₃(aq)</i>	49.3007	49.2904	-0.0103	103.5942	-0.0013	-0.0010
NGS1 <i>Acid H₂SO₄(aq)</i>	7.1294	7.1398	0.0104	24.6578	0.0047	0.0042

Table 13: Estimations of Erosion δ by Volume and Surface Area computations: (a) Cubic approximation; and (b) Surface area approximation; V_2 initial volume (Round 02) and V_3 final volume (Round 03) of 2nd accelerated erosion period.

Note that the above two ways of computing mean δ are based on different measurements (3D scans and micro-CT). We have computed δ in both ways and the results for the various slabs are quite close to each other, confirming the reliability of the proposed computations (see Tables 12, 13).

Remarks Since the micro-CT data did in some cases not cover the whole volume of the slabs (in particular some large stone slabs were not properly positioned into the micro-CT device measurement space) during the Round 01 measurements, V_1 could not be directly computed from them, so finally it was computed from the first round mass m_1 using the second round density ρ_2 , which was considered constant between the two cycles. Thus, NBL1, NGL1 and NGL2, R01 volumes, V_1 , surface erosion computations between R01 and R02 may not be reliable. On the contrary, during Round 03, all stone slabs were fitted into the micro-CT device measurement space, thus, surface erosion computations between R02 and R03 can be considered more reliable.

Since the back face of some slabs (particularly EL3, ES1 NBS1 and NGS1) was not scanned at Round 01, S_1 could not be directly computed. For this reason, we finally used surface area S_2 of (Round 02) for all the computations as more reliable, instead of the average area $S_{avg} = (S_1 + S_2)/2$.

Finally, stone slabs NBL3 and NBS1 under acid weathering (R01 to R02) exhibit swelling which overcomes the recession of material from their surfaces. Stone slabs NGL3 and NGS1 under acid weathering exhibit swelling as well but not so intense

which almost equalizes the recession of materials from their surfaces. This swelling phenomenon exhibited also on Pentelic marble under acid weathering during the second period (R02 to R03). This swelling phenomenon opposed recession and actually supersedes second period's recession computations for the acid experiments.

2.3.3 Computing Mean Erosion Rates

In this section we present the erosion rates computed for every experiment and in relation to mass, volume and recession. The purpose of these computations is to reveal any "canonical" behaviour that is hidden behind the computations of total recession values irrespective of the cycles that each accelerated experiment is repeated.

Stone		duration <i>days</i>	cycles <i>c</i>	$\Delta m/c$ <i>gr/c</i>	$\frac{\Delta m}{m}/c$ <i>%/c</i>	$\Delta V/c$ <i>cm³/c</i>	$\frac{\Delta V}{V}/c$ <i>%/c</i>	$\delta = \frac{\Delta V}{S}$ <i>mm</i>	δ/c <i>μm/c</i>
<i>Freeze-and-Thaw Experiment</i>									
EL1	1 st (R01-R02)	24	72	-0.0006	-0.0021	-0.0013	-0.0124	-0.0309	-0.43
	2 nd (R02-R03)	56	168	-0.0001	-0.0002	-0.0006	-0.0055	-0.0321	-0.19
NBL1	1 st (R01-R02)	24	72	-0.0053	-0.0031	-0.0019	-0.0031	-0.0115	-0.16
	2 nd (R02-R03)	56	168	-0.0050	-0.0030	-0.0011	-0.0018	-0.0151	-0.09
NGL1	1 st (R01-R02)	24	72	-0.0006	-0.0006	-0.0002	-0.0006	-0.0022	-0.03
	2 nd (R02-R03)	56	168	-0.0003	-0.0003	-0.0026	-0.0073	-0.0604	-0.36
<i>Salt Experiment</i>									
EL2	1 st (R01-R02)	32	128	-0.0015	-0.0061	-0.0010	-0.0107	-0.0450	-0.35
	2 nd (R02-R03)	16	64	-0.0022	-0.0089	-0.0003	-0.0031	-0.0064	-0.10
NBL2	1 st (R01-R02)	32	128	-0.0546	-0.0279	-0.0128	-0.0182	-0.1296	-1.01
	2 nd (R02-R03)	16	64	-0.1417	-0.0750	-0.0318	-0.0462	-0.1618	-2.53
NGL2	1 st (R01-R02)	32	128	-0.0057	-0.0035	-0.0020	-0.0035	-0.0244	-0.19
	2 nd (R02-R03)	16	64	-0.0179	-0.0111	-0.0022	-0.0040	-0.0139	-0.22

Table 14: Erosion rates for the Salt and the Freeze-and-Thaw experiments.

The erosion rates of the physical/mechanical accelerated experiments are presented in Table 14 and that of the chemical accelerated experiments in Table 15. The mass change per cycle $\Delta m/c$ and the relative mass change per cycle $\frac{\Delta m}{m}/c$ are presented; the volume change per cycle $\Delta V/c$ and the relative volume change per cycle $\frac{\Delta V}{V}/c$ are also presented, and finally, the total erosion $\delta = \frac{\Delta V}{S}$ and the erosion per cycle δ/c .

The results do not show any "canonical" behaviour that can be modeled reliably. For example, mass loss rates for marble samples (EL3 and ES1) in acidic solutions seem to slow down from 1st to 2nd Period, concurrently volume exhibits swelling behaviours, resulting in unreliable recession rates. The "Nidaros Bad" soapstone samples (NBL3 and NBS1) exhibit opposite behaviours in acidic solutions, with swelling rates close to one another between the 1st and 2nd Period for NBL3, but a dramatic slow down in the swelling rate of NBS1. Only, the "Nidaros Good" soapstone samples (NGL3 and

Stone	duration <i>days</i>	cycles <i>c</i>	$\Delta m/c$ <i>gr/c</i>	$\frac{\Delta m}{m}/c$ <i>%/c</i>	$\Delta V/c$ <i>cm³/c</i>	$\frac{\Delta V}{V}/c$ <i>%/c</i>	$\delta = \frac{\Delta V}{S}$ <i>mm</i>	δ/c <i>μm/c</i>
<i>Acid H₂SO₄+HNO₃(aq)</i>								
EL3 1 st (R01-R02)	41	4	-0.0537	-0.19	-0.0393	-0.38	-0.0527	-13.19
2 nd (R02-R03)	24	4	-0.0099	-0.04	0.0046	0.05	0.0062	1.55
NBL3 1 st (R01-R02)	41	4	-0.2014	-0.14	0.2518	0.51	0.1034	25.85
2 nd (R02-R03)	24	4	-0.1081	-0.08	0.2109	0.42	0.0861	21.52
NGL3 1 st (R01-R02)	41	4	-0.0665	-0.05	0.0112	0.02	0.0043	1.08
2 nd (R02-R03)	24	4	-0.0082	-0.01	-0.0026	-0.01	-0.0010	-0.25
<i>Acid H₂SO₄(aq)</i>								
ES1 1 st (R01-R02)	45	4	-0.0633	-0.23	-0.0427	-0.41	-0.0569	-14.23
2 nd (R02-R03)	30	4	-0.0179	-0.07	-0.0003	-0.00	-0.0004	-0.11
NBS1 1 st (R01-R02)	37	4	-0.0926	-0.31	0.0563	0.52	0.0683	17.07
2 nd (R02-R03)	30	4	-0.0359	-0.12	0.0259	0.23	0.0314	1.05
NGS1 1 st (R01-R02)	42	3	-0.0273	-0.13	-0.0030	-0.04	-0.0036	-1.20
2 nd (R02-R03)	30	4	-0.0057	-0.03	0.0026	0.04	0.0042	1.05

Table 15: Erosion rates for the *Acid H₂SO₄+HNO₃(aq)* and *H₂SO₄(aq)* experiments.

NGS1) exhibit a slight consistent behaviour in acidic solutions, with recession rates close to one another between the 1st and 2nd Period. Non “canonical” behaviour is also observed in the case of the Salt and Freeze-and-Thaw experiments.

Remarks The same Remarks as expressed in 2.3.2 apply here as well. Furthermore, mass measurement deviations due to the carbon coating used in QEMSCAN measurements are described. For the freeze-and-thaw weathering, except for NBL1, the other two showed slight decrease in mass-loss rates. For such a case the carbon coating from the QEMSCAN measurements could be one factor to consider. Actually, there was observable carbon deposition on the samples; much more clearly visible in the case of EL1. The relatively less porous samples (EL1 and NGL1) are, as expected, less affected by the freeze-thaw weathering than NBL1. The effect of the carbon coating seems to be more pronounced for the more porous ones.

The carbon coating used in QEMSCAN measurements is one of the reasons for the observed mass discrepancies in all the experiments. The impact of the carbon coating appears to be more significant when it comes to weathering conditions, like the freeze-and-thaw, that led to relatively lower mass loss/surface recession. Of course, there is some influence of the coating on other samples in the salt and acid weathering. However, its contribution, in these cases, is apparently relatively low. Appearances of the samples before and after weathering is a clear indicator of the extent to which the coating affected the mass measurements and other properties observed. However, the whole unexpected/unpredicted observations can not be attributed to the carbon coating alone. The later observations, in the case of salt and acid weathering experiments, are indicators.

2.3.4 Computing Erosion on every Vertex of the Stone Mesh

A key problem in measuring erosion based on scans made across time is the difficulty in registering these scans. Due to the absence of an external reference frame, a typical registration algorithm, such as Iterative Closest Point (ICP) [BM92], will align the scans so as to minimize the RMS error between them, which is not an ideal solution in case of erosion, since it diminishes the common erosion that has to be measured. Thus, for the case of the large monumental scans for which we do not have any other information except the surface mesh, the two consecutive scans are at first registered using ICP and then the per vertex erosion is computed in a relative manner having positive and negative values with respect to the reference mesh (see Figure 30).

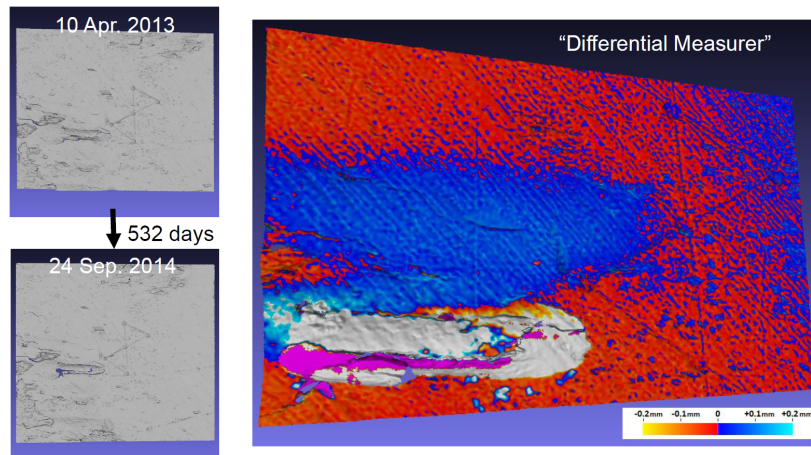


Figure 30: The “Differential Measurer” computes the distance map between two scanned meshes; here the 3D geometry meshes of the two X mason mark patches of Round 01 (2013-04-10) and Round 02 (2014-09-24) scans are depicted. The meshes are at first registered, and then distances are computed and mapped as textures onto the Round 01 mesh.

The same is actually true for the stone slabs (see Figure 31 (a)). A key problem in measuring erosion based on scans made across time is the difficulty in registering these scans. Due to the absence of an external reference frame, a typical registration algorithm, such as ICP, will align the scans so as to minimize the RMS error between them, which is not an ideal solution in case of erosion, see Figure 31 (a). See Section 2.4.5 for how we handled this problem in the case of large monumental scans; here is how we handled this problem in the case of the erosion chamber slabs.

We first register the top surface of the slabs using ICP and assume that this registration is sufficient in terms of the X and Y dimensions that define the top surface. The question is by how much to displace the slab in Z in order to accurately describe the erosion effect, see Figure 31 (b). Let us call this necessary displacement ΔZ . This should be equal to the computed mean erosion δ .

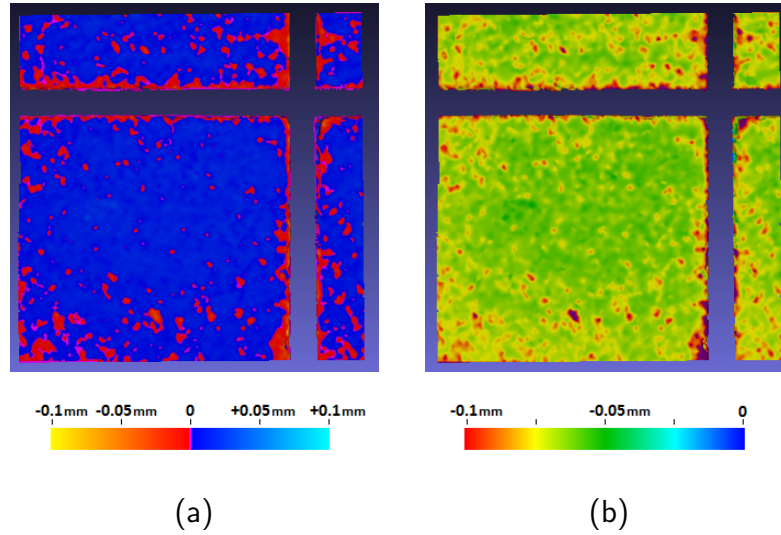


Figure 31: Differential Map of initial to eroded mesh for the frontal surface of the stone slab Elefsis Large 3 (EL3): (a) Slabs registered using ICP (blue indicates positive distances and red indicates negative distances); and (b) Slabs displaced in Z using estimated erosion value (red indicates most eroded areas and blue least eroded areas).

Hausdorff distance as a metric of stone erosion Consider two point sets:

$$M = \{\mathbf{m}_1, \mathbf{m}_2, \dots, \mathbf{m}_p\}$$

that represents the initial surface of a stone, and

$$T = \{\mathbf{t}_1, \mathbf{t}_2, \dots, \mathbf{t}_q\}$$

that represents the weathered surface of the same stone, where $\mathbf{m}_i, \mathbf{t}_j \in \mathbb{R}^3$.

The *standard Hausdorff* distance is defined as:

$$D_H(M, T) = \max(D_h(M, T), D_h(T, M)) ,$$

where

$$D_h(M, T) = \max_i \left(\min_j (\|\mathbf{m}_i - \mathbf{t}_j\|) \right) ,$$

is the *directed Hausdorff* distance from M to T .

The directed Hausdorff distance expresses the Euclidean distance $\|\mathbf{m}_i - \mathbf{t}_j\|$ of the farthest point of M from any point of T , i.e., the maximum value of the minimum Euclidean distances of the points of M from any point of T .

The *average directed Hausdorff distance* D_{MH} , of an initial stone model M to an eroded stone model T , can be defined, as:

$$D_{MH}(M, T) = \frac{1}{p} \sum_{i=1}^p \min_j (\|\mathbf{m}_i - \mathbf{t}_j\|) , \quad (2)$$

where $\|\mathbf{m}_i - \mathbf{t}_j\|$ is the Euclidean distance between the initial model vertices \mathbf{m}_i and the eroded model vertices \mathbf{t}_j , and p the number of the model vertices. D_{MH} expresses the mean value of the minimum Euclidean distances $\|\mathbf{m}_i - \mathbf{t}_j\|$ of the points of M from any point of T .

The average directed Hausdorff distance D_{MH} can be used as an overall mean erosion measure for the whole stone or a portion of it.

The distance

$$d_e(\mathbf{m}_i) = \min_j(\|\mathbf{m}_i - \mathbf{t}_j\|) \tag{3}$$

can be used as a local erosion measure which expresses at each vertex of the initial model M the distance of the closest vertex of the eroded model T , and is a scalar mapping of the erosion measure at each vertex of the initial stone model M , to which the eroded model T is registered.

2.3.5 Physico-chemical Aspects of the Erosion

The physico-chemical aspects of the erosion involve geometrical information and physico-chemical data on the surface of the object being eroded. A crucial first step for this procedure is the registration of the acquired geometric mesh data with the QEMSCAN mineral map texture data (Figure 32).



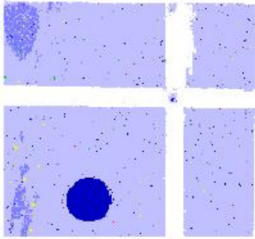

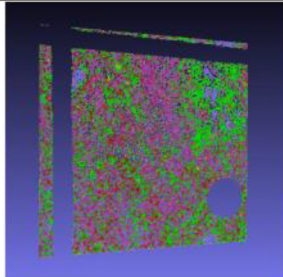
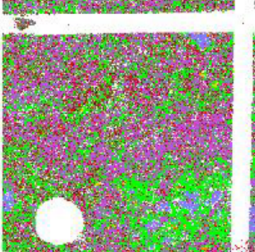
<u>3D mesh after regular resampling</u> @ 1024x1024 pxls	<u>3D mesh and mineral texture</u> @ 460x460 pxls after registration	<u>CGG Mineral map (100µm)</u> @ 230x230 pxls
Elefsis_Large_1	180.90° / 3.04 / 18.92x17.68 / 0.052	Freeze-Thaw + Rain Effect
		
Nidaros_Bad_Large_1	89.62° / 1.21 / 19.19x19.19 / 0.052	Freeze-Thaw + Rain Effect
		

Figure 32: Depiction of geometry and QEMSCAN registration results for the Elefsis Large 1 (EL1) marble slab and the Nidaros Bad Large 1 (NBL1) soapstone slab.

The general registration transformation matches landmark points annotated on the geometry image of the scanned 3D mesh, and the corresponding landmark points annotated on the QEMSCAN texture, which are considered as the invariant reference points under the correspondence transformation. These points are localized using the hole and the cross which are engraved onto the slabs for this purpose (Figure 33).

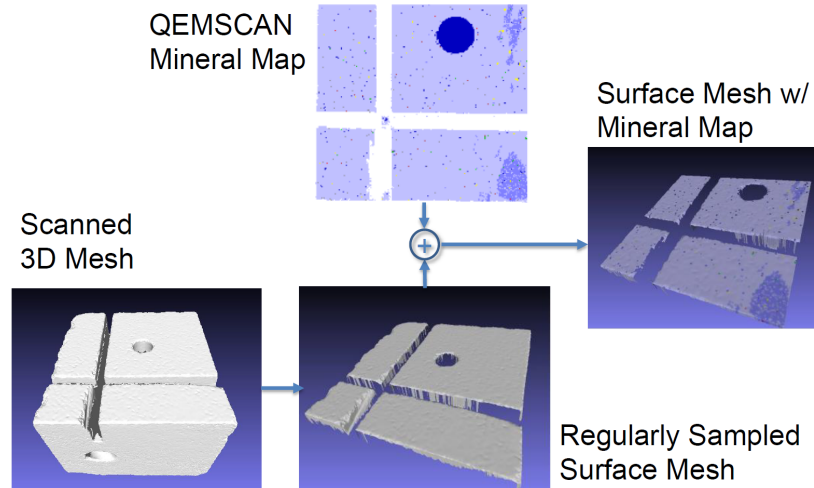


Figure 33: Depiction of 3D geometry and QEMSCAN registration results for the Elefsis Large 1 (EL1) marble slab.

Computing mineral related erosion using the QEMSCAN data In order to compute the erosion that every mineral exhibits, we apply the methodology that is presented in 2.3.4 and 2.3.2. Thus, after an ICP registration between the slab surfaces under consideration, the eroded mesh is shifted in the z direction so that the mean erosion resulting from averaging the per vertex computed erosion according to Section 2.3.4 and Eq. 2 equals the mean erosion computed according to Section 2.3.2 and Eq. 1. This methodology is applied to the EL3 and ES1 stone slabs, since the other slabs do not exhibit reliable erosion measurements.

To compute the mineral related erosion for EL3 undergone the *Acid* $\text{H}_2\text{SO}_4 + \text{HNO}_3(\text{aq})$ experiment we used the following approach: since the initial total average erosion (after the ICP registration of R01 and R02 meshes), using the per vertex distance is computed at 0.0175 mm a Z-shift value of -0.0702 mm was used to calibrate the mean erosion at -0.0527 mm .

To compute the mineral related erosion for ES1 undergone the *Acid* $\text{H}_2\text{SO}_4(\text{aq})$ experiment we used the following approach: since the initial total average erosion (after the ICP registration of R01 and R02 meshes), using the per vertex distance is computed at 0.0123 mm a Z-shift value of -0.0692 mm was used to calibrate the mean erosion at -0.0569 mm .

The results of the per mineral erosion computations are presented in Table 16. In this Table the mean and the standard deviation of the erosion per mineral are presented.

Minerals	EL3			ES1		
	mean mm	sigma mm	rel	mean mm	sigma mm	rel
Quartz	-0.04852	0.011712	0.94	-0.05851	0.015375	1.04
K-Feldspar	-	-	-	-	-	-
P-Feldspar	0.0	0.0	0.00	0.0	0.0	0.00
Biotite	0.0	0.0	0.00	0.0	0.0	0.00
Illite	-0.05156	0.011084	1.00	-0.04051	0.020525	0.72
Chlorite	-0.03424	0.004234	0.66	0.0	0.0	0.00
Smectite	0.0	0.0	0.00	0.0	0.0	0.00
Kaolinite	-	-	-	-	-	-
Glauconite	-	-	-	-	-	-
Calcite	-0.05179	0.015954	1.00	-0.05634	0.012067	1.00
Dolomite	-0.04185	0.016331	0.81	-0.04083	0.013836	0.72
Ankerite	-	-	-	-	-	-
Siderite	0.0	0.0	0.00	0.0	0.0	0.00
Gypsum	-0.04350	0.021000	0.84	-0.05228	0.006127	0.93
Pyrite	-0.04711	0.003215	0.91	0.0	0.0	0.00
H-Minerals	0.0	0.0	0.00	-0.05638	0.004156	1.00
Alt-Mafics	-0.05290	0.004777	1.02	-0.04996	0.016873	0.89
Total	-0.05175	0.016005		-0.05632	0.012467	

Table 16: The per mineral erosion computed between the two measurement rounds R01 and R02 for EL3 undergone the Acid $H_2SO_4 + HNO_3(aq)$ experiment and ES1 undergone the Acid $H_2SO_4(aq)$ experiment.

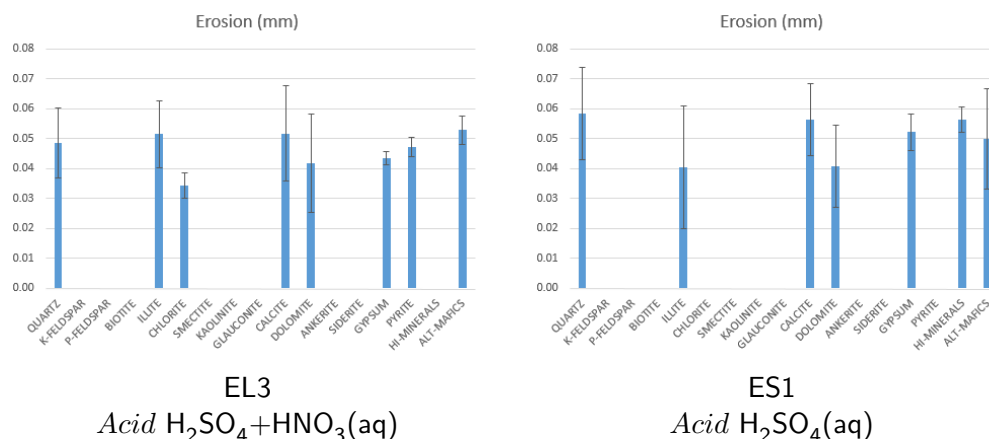


Figure 34: Depiction of the per mineral erosion for the EL3 and ES1 marble stones undergone the acid accelerated erosion experiment.

Also a column “rel” presents the relative erosion for every mineral w.r.t the erosion that “Calcite” exhibits, since calcite is the mineral for which an established erosion model exists (see 2.4.2). A graph of the per mineral erosion is depicted in Figure 34. Notice that “Dolomite” is eroded at a rate of 72% – 81% w.r.t that of “Calcite”, and “Gypsum” at a rate of 84% – 93% w.r.t that of “Calcite”.

We have to note that the main components of the marble samples are calcite, dolomite and gypsum (as a possible reaction product). The other components do not contribute significantly to the composition of the marble stones and their erosion computations

are of minor importance.

Computing Mineral Composition using the QEMSCAN data One way of computing the mineral composition of each stone is by computing the occurrences of each mineral on the QEMSCAN textures. This gives the relative surface coverage for each mineral which is actually related to the volume composition of each stone % v/v. In Tables 17 and 18 the mineral composition for the two first measurement rounds (Round 01 and Round 02) of the stone slabs undergone the accelerated erosion experiments is presented.

Minerals	EL1		EL2		NBL1		NBL2		NGL1		NGL2	
	R01	R02	R01	R02	R01	R02	R01	R02	R01	R02	R01	R02
Quartz	0.21	0.17	0.03	0.01	1.27	1.42	1.71	0.71	1.90	1.48	2.22	1.83
K-Feldspar	-	-	-	-	-	-	-	-	-	-	-	-
P-Feldspar	0.00	0.00	0.00	0.00	0.01	0.00	0.00	0.00	0.00	0.00	0.00	0.00
Biotite	0.00	0.00	0.00	0.00	4.55	4.98	4.20	2.75	1.22	1.91	1.50	1.18
Illite	0.10	0.05	0.46	0.37	0.00	0.00	0.00	0.00	0.00	0.00	0.00	0.00
Chlorite	0.01	0.00	0.00	0.01	31.35	29.19	31.23	11.82	39.09	37.69	18.84	12.95
Smectite	0.00	0.00	0.00	0.00	0.94	0.94	0.74	0.37	0.46	0.46	0.76	0.98
Kaolinite	-	-	-	-	-	-	-	-	-	-	-	-
Glauconite	-	-	-	-	-	-	-	-	-	-	-	-
Calcite	93.89	89.86	98.06	97.07	0.21	0.20	0.00	0.04	0.32	0.16	0.52	0.65
Dolomite	4.13	4.28	0.20	0.42	2.34	1.62	0.13	0.17	2.85	2.54	9.67	8.85
Ankerite	-	-	-	-	-	-	-	-	-	-	-	-
Siderite	0.00	0.00	0.00	0.00	0.36	0.53	0.26	1.24	0.14	0.11	0.06	0.40
Gypsum	0.08	0.05	0.06	0.40	7.31	10.24	3.86	7.16	0.02	0.10	0.03	4.24
Pyrite	0.00	0.00	0.01	0.03	0.30	0.18	1.24	0.57	0.23	0.25	0.13	0.34
H-Minerals	0.02	0.02	0.03	0.01	5.93	6.76	5.30	6.71	4.51	7.23	5.18	6.41
Alt-Mafics	0.00	0.01	0.00	0.02	40.20	34.16	40.82	32.66	42.98	38.55	56.89	48.81
Pores/Void	1.32	5.52	1.14	1.62	3.18	6.65	2.34	30.62	5.70	5.76	3.81	9.39
Others	0.25	0.02	0.36	0.77	2.06	2.93	8.18	5.17	0.58	3.74	0.37	3.97

Table 17: Surface coverage (% v/v composition) of the minerals that appear in the mineral maps of the various stone slabs for the two measurement rounds R01 and R02 of the Freeze-and-Thaw (EL1, NBL1 and NGL1 stone slabs) and the Salt (EL2, NBL2 and NGL2 stone slabs) experiments.

From the composition tables we can affirm the classification of the stone slabs:

Elefsis stones: consist almost entirely of Calcite (93% – 99%), some Dolomite (under 4%); with very low porosity (under 1.5%). These results are consistent with the *Pentelic Marble* characteristics [MBT*98].

Nidaros Good stones: consist mostly of Altered Mafics (43% – 57%) and Chlorite (19% – 39%), some High Minerals (4% – 6%) and Dolomite (3% – 10%); with low porosity (3.8% – 5.7%). These results are consistent with the *Grytdal Soapstone* characteristics [Sto97].

Nidaros Bad stones: consist mostly of Altered Mafics (38% – 46%) and Chlorite (31% – 35%), some High Minerals (3% – 6%) and Dolomite (under 7%); with low porosity (1.8% – 3.5%). These results are consistent with the *Grytdal Soapstone* characteristics [Sto97].

Minerals	EL3		ES1		NBL3		NBS1		NGL3		NGS1	
	R01	R02	R01	R02	R01	R02	R01	R02	R01	R02	R01	R02
Quartz	0.08	0.00	0.12	0.09	1.38	1.55	1.54	0.72	1.65	1.93	3.06	2.98
K-Feldspar	-	-	-	-	-	-	-	-	-	-	-	-
P-Feldspar	0.00	0.00	0.00	0.00	0.01	0.01	0.00	0.00	0.00	0.00	0.00	0.01
Biotite	0.00	0.00	0.00	0.00	4.58	5.70	4.20	2.84	1.41	2.82	1.51	1.90
Illite	0.03	0.16	0.28	0.46	0.01	0.01	0.00	0.00	0.00	0.01	0.00	0.02
Chlorite	0.02	0.00	0.00	0.00	35.27	32.04	31.23	39.77	38.49	36.77	29.72	29.69
Smectite	0.00	0.00	0.00	0.00	0.56	0.54	0.74	1.28	0.46	0.51	0.70	0.73
Kaolinite	-	-	-	-	-	-	-	-	-	-	-	-
Glauconite	-	-	-	-	-	-	-	-	-	-	-	-
Calcite	99.10	97.55	98.41	95.81	0.00	0.01	0.30	0.18	0.27	0.05	0.42	0.06
Dolomite	0.39	0.99	0.53	2.03	0.14	0.21	6.70	0.46	3.18	0.25	8.06	0.27
Ankerite	-	-	-	-	-	-	-	-	-	-	-	-
Siderite	0.00	0.00	0.00	0.00	0.43	0.46	0.29	0.95	0.09	0.54	0.17	4.77
Gypsum	0.03	0.12	0.01	0.49	0.53	6.11	1.19	24.76	0.03	0.02	0.08	0.88
Pyrite	0.01	0.00	0.00	0.00	0.76	0.87	1.00	1.18	0.43	0.51	0.22	0.27
H-Minerals	0.00	0.06	0.03	0.06	5.67	7.58	3.31	6.87	4.44	6.73	6.09	7.69
Alt-Mafics	0.01	0.02	0.01	0.03	46.04	38.18	38.37	23.81	44.11	36.63	45.52	42.13
Pores/Void	0.31	1.07	0.39	0.69	3.54	3.04	1.76	7.72	5.00	10.03	4.02	6.70
Others	0.02	0.03	0.21	0.27	1.08	3.69	1.63	4.14	0.44	3.20	0.47	1.92

Table 18: Surface coverage (% v/v composition) of the minerals that appear in the mineral maps of the various stone slabs for the two measurement rounds R01 and R02 of the Acid $H_2SO_4 + HNO_3(aq)$ (EL3, NBL3 and NGL3 stone slabs) and the Acid $H_2SO_4(aq)$ (ES1, NBS1 and NGS1 stone slabs) experiments.

Note the slight decrease of Calcite concentration in the marble slabs undergone the acidic experiments. Actually a respective increase in Gypsum is not observed since the slabs are washed with deionized water before the measurements. The same holds true for marble undergone the salt experiment. On the contrary a slight decrease of Calcite concentration for marble undergone the Freeze-and-Thaw experiment is attributed to the slight increase of porosity.

For the soapstone slabs the things are much more complicated. A slight decrease in Altered Mafics concentration is observed for the stone slabs undergone the acidic and the salt experiments. The concentration of Chlorite looks unaffected and slight decrease can be attributed to the increase of porosity. Also a significant increase in porosity is observed for all soapstone slabs irrespective of the erosion experiment. One can suppose that it is the loss of the dominant minerals which contributes to the increased porosity observed in addition to the mechanical effects.

Computing mineral changes using the QEMSCAN data To have a detailed description about the mineral changes that happen on the surface of the stone slabs the transition matrix (Right Stochastic Matrix) of the minerals for every stone slab is computed. The transition matrix shows the percentages of each stone mineral that are transformed into another stone mineral during the erosion process. Since every row of this matrix equals unity (i.e. 100%) it is a right stochastic matrix. This matrix can also be interpreted as the probability that one mineral can be transformed into another by the erosion.

EL3 (R01\R02)	UKNOW	QUARTZ	K-FELDSPAR	P-FELDSPAR	BIOTITE	ILLITE	CHLORITE	SMECTITE	KAOLINITE	GLAUCONITE	CALCITE	DOLOMITE	ANKERITE	SIDERITE	GYPSUM	PYRITE	HI-MINERALS	ALT-MAFICS	PORES	OTHER	VOID	Cmp R01
UKNOW																						0.00%
QUARTZ											100.00%											0.08%
K-FELDSPAR																						0.00%
P-FELDSPAR																						0.00%
BIOTITE																						0.00%
ILLITE											95.00%										5.00%	0.03%
CHLORITE											100.00%											0.02%
SMECTITE																						0.00%
KAOLINITE																						0.00%
GLAUCONITE																						0.00%
CALCITE					0.16%	0.00%					97.62%	0.92%			0.11%		0.06%	0.02%	0.30%	0.03%	0.77%	99.10%
DOLOMITE											80.05%	18.61%			0.43%				0.43%			0.39%
ANKERITE																						0.00%
SIDERITE																						0.00%
GYPSUM											100.00%											0.03%
PYRITE											100.00%											0.01%
HI-MINERALS																						0.00%
ALT-MAFICS											100.00%											0.01%
PORES											95.98%	2.30%			1.72%							0.29%
OTHER											100.00%											0.02%
VOID											71.43%	14.29%										14.29%
Comp R02	0.00%	0.00%	0.00%	0.00%	0.00%	0.16%	0.00%	0.00%	0.00%	0.00%	97.55%	0.99%	0.00%	0.00%	0.12%	0.00%	0.06%	0.02%	0.30%	0.03%	0.77%	100.00%

Figure 35: Transition Matrix of minerals between the R01 and R02 measurements for the EL3 marble slab undergone the *Acid* H₂SO₄+HNO₃(aq) experiment.

ES1 (R01\R02)	UKNOW	QUARTZ	K-FELDSPAR	P-FELDSPAR	BIOTITE	ILLITE	CHLORITE	SMECTITE	KAOLINITE	GLAUCONITE	CALCITE	DOLOMITE	ANKERITE	SIDERITE	GYPSUM	PYRITE	HI-MINERALS	ALT-MAFICS	PORES	OTHER	VOID	Cmp R01
UKNOW																						0.00%
QUARTZ		12.00%									88.00%											0.12%
K-FELDSPAR																						0.00%
P-FELDSPAR																						0.00%
BIOTITE																						0.00%
ILLITE						19.43%	1.71%				66.29%	8.00%			3.43%						1.14%	0.28%
CHLORITE																						0.00%
SMECTITE																						0.00%
KAOLINITE																						0.00%
GLAUCONITE																						0.00%
CALCITE		0.07%			0.36%	0.01%					96.23%	1.87%	0.00%		0.48%		0.06%	0.03%	0.65%	0.05%	0.17%	98.41%
DOLOMITE					5.04%						57.57%	27.60%							9.20%	0.59%		0.53%
ANKERITE																						0.00%
SIDERITE																						0.00%
GYPSUM											75.00%	25.00%										0.01%
PYRITE																						0.00%
HI-MINERALS											100.00%											0.03%
ALT-MAFICS											100.00%											0.01%
PORES						4.84%					90.73%	3.23%							1.21%			0.39%
OTHER																						0.00%
VOID											49.24%	3.03%			3.79%							43.94%
Comp R02	0.00%	0.09%	0.00%	0.00%	0.00%	0.46%	0.02%	0.00%	0.00%	0.00%	95.81%	2.03%	0.00%	0.00%	0.49%	0.00%	0.06%	0.03%	0.69%	0.06%	0.27%	100.00%

Figure 36: Transition Matrix of minerals between the R01 and R02 measurements for the ES1 marble slab undergone the *Acid* H₂SO₄(aq) experiment.

To compute the transition matrices the 3D meshes textured with the QEMSCAN data are first registered, and for each vertex of the initial mesh with an identified mineral a corresponding vertex from the final mesh is localized according to Eq. 3 and its mineral is identified, thus the initial mineral - final mineral conjunction is created. By counting these occurrences for every pair of minerals the transition matrix is computed.

The transition matrices of marble slabs (EL3 and ES1) exhibited in the acid experiments are presented in Figures 35 and 36. The transition matrices reveal that most of the changes in the mineral composition have to be attributed to physical/mechanical changes rather than chemical ones. For example the “transition” of Quartz to Calcite by 100% for EL3 and by 88% for ES1 is not a feasible chemical transformation, because Quartz is the most chemically stable mineral. This phenomenon can be attributed to the removal of the Quartz grains from the surface of the stone and the revealing of the layer underneath consisting of Calcite grains. The same holds true for the transitions of Dolomite and other minerals to Calcite. On the other hand, Gypsum tends to dissolve more readily, revealing the Calcite of a deeper layer.

NGL3 (R01\R02)	UKNOW	QUARTZ	K-FELDSPAR	P-FELDSPAR	BIOTITE	ILLITE	CHLORITE	SMECTITE	KAOLINITE	GLAUCONITE	CALCITE	DOLOMITE	ANKERITE	SIDERITE	GYPSUM	PYRITE	HI-MINERALS	ALT-MAFICS	PORES	OTHER	VOID	Cmp R01
UKNOW																						0.00%
QUARTZ		4.35%			2.32%		19.73%	0.39%						0.39%		0.77%	9.77%	50.48%	8.90%	2.90%		1.65%
K-FELDSPAR																						0.00%
P-FELDSPAR																						0.00%
BIOTITE		1.01%			2.93%		35.70%	1.01%				0.11%		0.11%	0.45%	8.67%	37.39%	9.12%	3.49%			1.41%
ILLITE																						0.00%
CHLORITE		1.08%			3.08%	0.02%	54.44%	0.52%			0.03%	0.04%		0.21%	0.03%	0.43%	4.12%	21.93%	9.43%	4.49%	0.16%	38.49%
SMECTITE		0.35%			4.88%		36.24%										9.06%	41.11%	5.57%	2.79%		4.67%
KAOLINITE																						0.00%
GLAUCONITE																						0.00%
CALCITE		2.33%			1.16%		28.49%					1.74%		2.91%		0.58%	4.65%	29.65%	18.60%	9.88%		0.27%
DOLOMITE		0.75%			2.35%		32.67%	0.25%			0.30%	5.71%		10.07%		0.50%	2.86%	19.89%	23.55%	1.10%		3.18%
ANKERITE																						0.00%
SIDERITE		3.57%			3.57%		37.50%									5.36%	3.57%	39.29%	3.57%	3.57%		0.09%
GYPSUM							55.00%									35.00%	10.00%					0.03%
PYRITE						2.95%	31.73%									39.11%	5.17%	11.44%	7.01%	2.58%		0.43%
HI-MINERALS		2.72%			3.19%		24.44%	0.61%			0.29%	0.04%		0.39%		0.07%	10.18%	45.91%	9.75%	2.37%	0.04%	4.44%
ALT-MAFICS		2.59%		0.00%	2.62%	0.01%	24.04%	0.52%			0.03%	0.10%		0.21%	0.02%	0.19%	8.69%	49.43%	9.24%	2.28%	0.03%	44.11%
PORES		2.47%			2.47%		32.17%	0.51%			0.13%			0.22%		0.93%	7.34%	38.07%	12.06%	3.30%	0.32%	4.97%
OTHER					4.35%		50.36%							1.45%			7.97%	21.74%	10.51%	1.81%	1.09%	0.44%
VOID					8.70%		26.09%										8.70%	13.04%	8.70%	4.35%	30.43%	0.04%
Comp R02	0.00%	1.93%	0.00%	0.00%	2.82%	0.01%	36.77%	0.51%	0.00%	0.00%	0.05%	0.25%	0.00%	0.54%	0.02%	0.51%	6.73%	36.63%	9.92%	3.20%	0.11%	100.00%

Figure 37: Transition Matrix of minerals between the R01 and R02 measurements for the NGL3 marble slab undergone the $Acid\ H_2SO_4 + HNO_3(aq)$ experiment.

NGS1 (R01\R02)	UKNOW	QUARTZ	K-FELDSPAR	P-FELDSPAR	BIOTITE	ILLITE	CHLORITE	SMECTITE	KAOLINITE	GLAUCONITE	CALCITE	DOLOMITE	ANKERITE	SIDERITE	GYPSUM	PYRITE	HI-MINERALS	ALT-MAFICS	PORES	OTHER	VOID	Cmp R01
UKNOW																						0.00%
QUARTZ		8.74%			0.68%		14.25%	0.42%						4.24%	0.93%	0.25%	15.27%	49.02%	4.33%	1.44%	0.42%	3.06%
K-FELDSPAR																						0.00%
P-FELDSPAR																						0.00%
BIOTITE		3.26%			0.86%		36.94%	0.86%						1.55%	0.69%		7.90%	38.49%	7.56%	1.37%	0.52%	1.51%
ILLITE																						0.00%
CHLORITE		1.36%		0.02%	1.96%		54.84%	0.67%			0.17%			1.89%	0.72%	0.14%	4.85%	24.93%	4.39%	3.16%	0.89%	29.72%
SMECTITE		0.75%			1.49%		20.15%	1.49%						5.22%			7.09%	57.09%	5.60%	0.75%	0.37%	0.70%
KAOLINITE																						0.00%
GLAUCONITE																						0.00%
CALCITE		1.24%					16.77%							18.01%			6.83%	37.89%	9.94%	3.11%	6.21%	0.42%
DOLOMITE		1.54%			1.03%		19.18%	0.39%			0.45%	2.19%		34.86%	0.48%	0.87%	6.28%	20.82%	10.14%	0.71%	1.06%	8.06%
ANKERITE																						0.00%
SIDERITE		3.57%			5.36%		32.14%							7.14%			3.57%	33.93%	7.14%	3.57%	3.57%	0.15%
GYPSUM		3.13%					12.50%							6.25%		6.25%	3.13%	53.13%	15.63%			0.08%
PYRITE							10.84%							9.64%	4.82%	24.10%	7.23%	36.14%	3.61%	2.41%	1.20%	0.22%
HI-MINERALS		5.03%			2.60%	0.09%	20.93%	0.72%			0.17%			1.11%	1.53%	0.13%	12.66%	46.55%	4.65%	2.69%	1.15%	6.09%
ALT-MAFICS		3.57%			2.07%	0.02%	17.32%	0.83%			0.06%	0.05%		2.09%	0.99%	0.20%	8.81%	56.27%	5.33%	1.21%	1.17%	45.52%
PORES		4.39%			1.62%		29.71%	0.81%			0.27%			1.96%	0.74%		6.08%	42.88%	9.32%	1.82%	0.41%	3.84%
OTHER		1.66%			1.66%		49.72%	1.10%							1.10%		6.08%	20.99%	4.42%	8.29%	4.97%	0.47%
VOID		1.45%			2.90%		15.94%							1.45%			5.80%	26.09%	5.80%	1.45%	39.13%	0.18%
Comp R02	0.00%	2.98%	0.00%	0.01%	1.90%	0.02%	29.69%	0.73%	0.00%	0.00%	0.06%	0.27%	0.00%	4.77%	0.88%	0.27%	7.69%	42.13%	5.58%	1.92%	1.12%	100.00%

Figure 38: Transition Matrix of minerals between the R01 and R02 measurements for the NGS1 marble slab undergone the $Acid\ H_2SO_4(aq)$ experiment.

The transition matrices of good soapstone slabs (NGL3 and NGS1) exhibited in the acid experiments are presented in Figures 37 and 38. In this case Quartz remains unaltered with a percentage under 9% showing a major transition to other minerals. This is also the case for the dominant minerals in soapstone; Chlorite remains unaltered with a percentage of 55%, and Altered Mafics remain unaltered with a percentage of 50% – 54%. There are also transitions for the rest of the minerals in a more chaotic way making the transition modeling an infeasible task.

The transition matrices of bad soapstone slabs (NBL3 and NBS1) exhibited in the acid experiments are presented in Figures 39 and 40. In this case Quartz remains unaltered with a percentage under 1% showing a major transition to other minerals. This is also the case for the dominant minerals in soapstone; Chlorite remains unaltered with a percentage of 32% – 38%, and Altered Mafics remain unaltered with a percentage of 31% – 43%. There are also transitions for the rest of the minerals in a more chaotic way making the transition modeling for this case an infeasible task as well.

We have to note also the heterogeneous nature of soapstones. As a new layer is

NBL3 (R01\R02)	UKNOW	QUARTZ	K-FELDSPAR	P-FELDSPAR	BIOTITE	ILLITE	CHLORITE	SMECTITE	KAOLINITE	GLAUCONITE	CALCITE	DOLOMITE	ANKERITE	SIDERITE	GYPSUM	PYRITE	HI-MINERALS	ALT-MAFICS	PORES	OTHER	VOID	Cmp R01
UKNOW																						0.00%
QUARTZ		1.47%			4.65%		31.29%	0.34%					0.11%		9.98%	0.57%	8.05%	39.34%	2.04%	2.15%		1.38%
K-FELDSPAR																						0.00%
P-FELDSPAR							50.00%											50.00%				0.01%
BIOTITE		1.84%			6.79%		33.91%	0.89%					0.07%	0.24%	5.90%	0.58%	6.86%	37.80%	2.63%	2.49%		4.58%
ILLITE																		100.00%				0.01%
CHLORITE		1.40%		0.01%	5.51%	0.02%	38.42%	0.40%					0.24%	0.49%	6.19%	0.99%	6.77%	32.14%	2.92%	4.49%		35.27%
SMECTITE		1.96%			6.16%		30.53%								4.20%	1.68%	10.64%	35.29%	4.48%	5.04%		0.56%
KAOLINITE																						0.00%
GLAUCONITE																						0.00%
CALCITE																						0.00%
DOLOMITE					2.30%		41.38%								2.30%		5.75%	41.38%	3.45%	3.45%		0.14%
ANKERITE																						0.00%
SIDERITE					7.27%		20.73%							0.36%	2.18%	3.27%	8.00%	50.18%	3.64%	4.36%		0.43%
GYPSUM		1.48%			6.51%		34.62%	0.59%						0.30%	4.73%	0.59%	9.76%	34.62%	2.66%	4.14%		0.53%
PYRITE		0.62%			4.96%		30.37%	1.03%						0.21%	5.79%	17.98%	4.34%	23.76%	8.06%	2.89%		0.76%
HI-MINERALS		1.79%		0.03%	4.85%		29.47%	0.55%			0.03%	0.08%		0.28%	6.53%	0.41%	7.44%	41.09%	3.36%	4.10%		5.67%
ALT-MAFICS		1.63%		0.01%	5.80%		27.18%	0.64%			0.01%	0.22%		0.52%	5.91%	0.55%	8.33%	42.91%	3.03%	3.25%		46.04%
PORES		1.77%			6.27%		33.16%	0.44%					0.13%	0.49%	6.75%	0.04%	7.20%	36.69%	3.36%	3.71%		3.54%
OTHER		1.44%			6.63%		37.32%	0.29%					0.86%	0.29%	8.21%	4.18%	6.20%	30.69%	2.88%	1.01%		1.08%
VOID																						0.00%
Comp R02	0.00%	1.55%	0.00%	0.01%	5.70%	0.01%	32.04%	0.54%	0.00%	0.00%	0.01%	0.21%	0.00%	0.46%	6.11%	0.87%	7.58%	38.18%	3.04%	3.69%	0.00%	100.00%

Figure 39: Transition Matrix of minerals between the R01 and R02 measurements for the NBL3 marble slab undergone the $Acid\ H_2SO_4 + HNO_3(aq)$ experiment.

NBS1 (R01\R02)	UKNOW	QUARTZ	K-FELDSPAR	P-FELDSPAR	BIOTITE	ILLITE	CHLORITE	SMECTITE	KAOLINITE	GLAUCONITE	CALCITE	DOLOMITE	ANKERITE	SIDERITE	GYPSUM	PYRITE	HI-MINERALS	ALT-MAFICS	PORES	OTHER	VOID	Cmp R01
UKNOW																						0.00%
QUARTZ		0.14%			2.47%		21.02%	0.41%						1.24%	30.22%	0.55%	6.59%	26.79%	3.43%	7.14%		1.54%
K-FELDSPAR																						0.00%
P-FELDSPAR																						0.00%
BIOTITE		1.34%			3.65%		22.07%	0.89%					0.37%	0.30%	27.96%	1.27%	7.16%	25.95%	5.15%	3.73%	0.15%	2.84%
ILLITE																						0.00%
CHLORITE		0.74%			3.41%		32.17%	0.62%			0.08%	0.29%		0.64%	24.83%	0.88%	5.30%	19.76%	6.09%	4.89%	0.31%	39.77%
SMECTITE		0.17%			5.45%		22.31%							0.33%	24.96%	0.33%	5.29%	31.74%	4.96%	4.13%	0.33%	1.28%
KAOLINITE																						0.00%
GLAUCONITE																						0.00%
CALCITE					4.26%		12.77%				4.96%	2.84%		8.51%	17.73%	1.42%	11.35%	4.96%	30.50%	0.71%		0.30%
DOLOMITE		0.47%			1.58%		16.28%	0.09%			1.23%	3.00%		4.84%	16.78%	4.68%	14.73%	7.11%	26.23%	2.72%	0.25%	6.70%
ANKERITE																						0.00%
SIDERITE		1.45%					26.81%							7.25%	24.64%	10.14%	4.35%	7.25%	10.14%	5.07%	2.90%	0.29%
GYPSUM		1.07%			4.09%		27.40%						0.36%	1.78%	24.38%	1.96%	5.16%	16.37%	13.17%	4.09%	0.18%	1.19%
PYRITE					1.05%		26.58%	0.84%						1.48%	19.41%	12.87%	3.38%	16.03%	16.03%	2.32%		1.00%
HI-MINERALS		1.02%			3.46%		25.03%	0.51%			0.13%	0.26%		0.51%	23.30%	0.45%	5.83%	27.46%	6.02%	5.83%	0.19%	3.31%
ALT-MAFICS		0.78%			3.00%		20.33%	0.94%			0.07%	0.23%		0.40%	26.33%	0.50%	7.30%	31.49%	4.85%	3.51%	0.28%	38.37%
PORES					1.87%		25.16%				1.49%	1.49%		3.24%	20.30%	2.49%	8.84%	15.32%	18.56%	1.25%		1.70%
OTHER		0.26%			2.99%		33.12%	0.26%						1.95%	20.26%	1.69%	6.49%	16.49%	7.79%	5.58%	3.12%	1.63%
VOID							17.86%							3.57%	25.00%		7.14%	14.29%	10.71%	3.57%	17.86%	0.06%
Comp R02	0.00%	0.72%	0.00%	0.00%	3.09%	0.00%	25.44%	0.67%	0.00%	0.00%	0.18%	0.46%	0.00%	0.95%	24.76%	1.18%	6.87%	23.81%	7.39%	4.14%	0.33%	100.00%

Figure 40: Transition Matrix of minerals between the R01 and R02 measurements for the NBS1 marble slab undergone the $Acid\ H_2SO_4(aq)$ experiment.

exposed due to the weathering, the whole structure and composition can be quite different. Some of the changes can be attributed to mechanical causals, but others to chemical ones. This makes comparisons difficult for highly heterogeneous samples like the soapstones. The only valid assumption is that the more inert components to the weathering remain intact.

2.4 Modeling Erosion

The main weathering processes responsible for the erosion of rocks and stones are of chemical and physical nature. **Chemical weathering** describes the decay of the stone material into new chemical products by the chemical reactions of the stone material with water and atmospheric gases like carbon dioxide (CO_2), sulfur dioxide (SO_2) and nitrogen dioxide (NO_2). These processes are simulated through the accelerated erosion experiments using the acid chambers. **Physical or mechanical weathering** describes the disintegration of the stone material into smaller particles under the action of heat, water and pressure on the stone, which then can be removed by

gravity, wind, water or ice. The two different mechanical weathering scenarios that are usually distinguished are the weathering caused by soluble salts and the weathering caused by wet/dry and freeze/thaw cycles which are simulated by Salt and Freeze-and-Thaw accelerated erosion experiments.

The formulas which describe the surface weathering provide usually a measure for the change of the surface geometry (deposition/recession δ) of the object surface which depends on the environmental parameters (such as the amount of rain fall, the concentrations of the involved pollution gases, the temperature, the humidity etc.) and the stone material. This suggests a simple procedure to simulate erosion acting just on the object surface mesh: For each vertex of the surface mesh one has to calculate the recession rate of the erosion according to the various environmental parameters with adoptions to the local stone material parameters. Then the surface mesh change is performed along the normal direction of the surface.

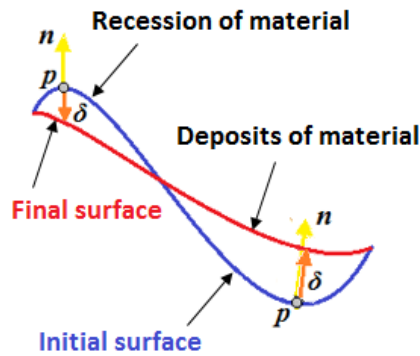


Figure 41: Modeling of an erosion process on the surface of a stone.

2.4.1 Geometric Model of Erosion

Defining the initial surface of a stone as a set of 3D points $S = \{\mathbf{p}_1, \mathbf{p}_2, \dots, \mathbf{p}_n\}$ and the weathered surface of the same stone in a similar way as $S' = \{\mathbf{p}'_1, \mathbf{p}'_2, \dots, \mathbf{p}'_n\}$ with $\mathbf{p}_i, \mathbf{p}'_j \in \mathbb{R}^3$ one can describe the surface deposition/recession as an offsetting procedure with the help of the diffusion equation.

The diffusion equation

$$\frac{\partial \mathbf{p}}{\partial t} = \mu \nabla^2 \mathbf{p} = \delta \mathbf{n} , \quad (4)$$

leads to a simple update rule for computing the offset of the mesh vertices \mathbf{p}_i

1. iterate
2. $\mathbf{p}'_i = \mathbf{p}_i + \delta_i \mathbf{n}_i dt$,
3. until # of epochs (of dt duration each)

Here \mathbf{n}_i is the normal vector at the surface vertex \mathbf{p}_i and δ_i is the surface recession ($\delta_i < 0$) or deposition ($\delta_i > 0$) at this point (see Figure 41). The corresponding time interval of each epoch is denoted as dt . *Epochs* denote time intervals where different environmental conditions, such as pollution concentration and/or rain fall, can be defined. The number of epochs denotes the total time over which the object is exposed to weathering.

2.4.2 Chemical Model of Erosion

The value of the surface off-setting rate δ_i ideally should be determined by the accelerated erosion experiments. The theoretical background of the chemical processes are modeled by the unreacted-core model, which leads to the computation of the mesh offsetting δ for the cases of dry deposition of crust due to $SO_2 + NO_2$ and surface recession by acid rain due to $SO_2 + NO_2 + CO_2$ is described in detail in [GB99, YCJ*96, YJCG94, BR93].

Chemical processes are modeled by the unreacted-core model, which leads to the computation of the mesh offset δ for the following weathering cases:

1. Reaction model for dry deposition of crust due to SO_2

$$\left(\frac{1}{2D_e}\right)\delta^2 + \left(\frac{1}{h_d} + \frac{1}{k_s}\right)\delta = C_{SO_2} \frac{M_B}{\rho_B} t, \quad (5)$$

2. Reaction model for dry deposition of crust due to $SO_2 + NO_2$

$$\left(\frac{1}{2D_{en}}\right)\delta^2 + \left(\frac{1}{k_{sn}}\right)\delta = 2 a_m (C_{SO_2})^{\alpha_1} (C_{NO_2})^{\alpha_2} \frac{M_B}{\rho_B} t, \quad (6)$$

3. Reaction model for surface recession by acid rain due to $SO_2 + NO_2 + CO_2$

$$\delta = [6.56 + 27.38 \times 10^{(3.0 - R_{pH})}] R_V t + 2 k_r (C_{SO_2})^{\alpha_1} (C_{NO_2})^{\alpha_2} \frac{M_B}{\rho_B} t \quad (7)$$

where

δ : the overall crust deposition or the overall surface recession (in *cm*)

D_e : internal diffusivity (in cm^2/h)

D_{en} : internal diffusivity (in cm^2/h)

h_d : mass transfer coefficient (in cm/h)

k_s : kinetic rate constant (in cm/h)

k_{sn} : kinetic rate constant (in cm/h)

k_r : kinetic rate constant for dry deposition and run-off effect (in cm/h)

M_B : gram-molecular weight of mineral - $M_B = 100.9 \text{ g/mol}$ for calcite

ρ_B : density of stone (in g/cm^3) - $\rho_B = 2.714 \text{ g/cm}^3$ for marble

a_m : 2.1 (ratio of molar volume of product to reactant)

α_1 : 0.7 (relative proportion of sulfate/nitrate)
 α_2 : 0.3 (relative proportion of sulfate/nitrate)
 C_{SO_2} : atmospheric concentration of SO_2 (in mol/cm^3)
 C_{NO_2} : atmospheric concentration of NO_2 (in mol/cm^3)
 R_V : rain height (in $m/year$)
 R_{pH} : rain pH
 t : time (in *hours*)

Stone dependent parameters are experimentally calculated in [GB99, YCJ*96, YJCG94]

D_e : 0.14 cm^2/h for marble and 0.37 cm^2/h for dolomite

D_{en} : 0.11 cm^2/h for marble

h_d : 544.27 cm/h

k_s : 312 cm/h for marble and 183 cm/h for dolomite

k_{sn} : 375 cm/h for marble

k_r : 2452 cm/h for marble.



Figure 42: Erosion rates computed on marble under certain environmental conditions for the comparison of the different weathering cases.

An example of the erosion rates (deposition/recession) of marble under certain environmental conditions is depicted in Figure 42, using:

$M_B = 100.9 \text{ g/mol}$ (molecular weight of calcite)

$\rho_B = 2.714 \text{ g/cm}^3$ (density of marble)

$C_{SO_2} = 4.09 \times 10^{-13} \text{ mol/cm}^3$, for 10 *ppb* SO_2 air pollution

$C_{NO_2} = 10.23 \times 10^{-13} \text{ mol/cm}^3$, for 25 *ppb* NO_2 air pollution

pH = 4.5 for rain acidity

$R_V = 1.13 \text{ m}$ rainfall in one year period

Note how dramatically high the recession rates due to acid rain are, compared to the deposition rates of crust in dry environments. This indicates that acid rain recession is the most significant component in the erosion model.

2.4.3 Computing Rain Recession at the CH Sites

Acid rain recession described by Eq. 7 consists of two components:

The recession due to the rain runoff of Ca^{2+} , during the rainy periods, i.e. the wet component [BR93]

$$\delta_{wet} = [6.56 + 27.38 \times 10^{(3.0 - R_{pH})}] R_V t \quad (8)$$

The recession due to the rain runoff of the deposits during the dry periods, i.e. the dry component [GB99, YCJ*96, YJCG94]

$$\delta_{dry} = 2 k_r (C_{SO_2})^{\alpha_1} (C_{NO_2})^{\alpha_2} \frac{M_B}{\rho_B} t \quad (9)$$

with

$$\delta_{tot} = \delta_{wet} + \delta_{dry}. \quad (10)$$

The environmental parameters for Elefsis are:

$$C_{SO_2} = 0.34 \times 10^{-13} \text{ mol/cm}^3$$

$$C_{NO_2} = 3.74 \times 10^{-13} \text{ mol/cm}^3$$

pH = 4.5 for rain acidity

$$R_V = 32.2 \text{ cm/yr rainfall}$$

For Elefsis and for a three year period, applying Equation 10 on marble, the wet component of recession is computed at $\delta_{wet} = 4.15 \mu m$, the dry component at $\delta_{dry} = 2.14 \mu m$, and the total at $\delta_{tot} = 6.29 \mu m$. For the exposure time of 979 days (Round 01: 20/03/2013 to Round 03: 24/11/2015) for the CH objects at Elefsis between the two scanning rounds, we get a value of total recession at $\delta_{tot} = 5.62 \mu m$.

The environmental parameters for Trondheim are:

$$C_{SO_2} = 9.11 \times 10^{-13} \text{ mol/cm}^3$$

$$C_{NO_2} = 9.11 \times 10^{-13} \text{ mol/cm}^3$$

pH = 4.5 for rain acidity

$$R_V = 85.4 \text{ cm/yr rainfall}$$

For Trondheim and for a three year period, applying Equation 10 on marble, the wet component of recession is computed at $\delta_{wet} = 19.05 \mu m$, the dry component

at $\delta_{dry} = 3.07 \mu m$, and the total at $\delta_{tot} = 22.12 \mu m$. For the exposure time of 967 days (Round 01: 10/04/2013 to Round 03: 03/12/2015) for the CH objects at Trondheim between the two scanning rounds, we get a value of total recession at $\delta_{tot} = 19.54 \mu m$.

The above results indicate that the rain recession is significantly more intensive in Trondheim than in Elefsis for the same type of stone (i.e. marble).

Remarks Since the unavailability of environmental data for recent years, a five year average (2010-2014) is used for the above environmental parameters for both sites. Also, since there are no measurements of C_{SO_2} in Trondheim, the C_{SO_2} value of Elefsis is used instead. Finally, due to the unavailability of the rain acidity at both locations a typical value of $pH = 4.5$ is used.

2.4.4 Equivalent Rain Height and Exposure Time Computations

For the accelerated acid experiments the exposure times in the solution can be projected in environmental exposure times using Equation 10 for the rain recession model. Since, the stone slabs were immersed into the acidic solutions all the time, only the "wet" part of the model's equation applies, i.e. Equation 8:

$$\delta_{wet} = -(9.29 \mu m/m) R_V t , \quad (11)$$

where the pH value of the acid solutions $pH = 4.0$ is used as the rain acidity, for the calculation of the constant factor $-9.29 \mu m/m$.

Since R_V is the rain height rate, i.e.

$$R_V = H_{rain}/t , \quad (12)$$

we have:

$$\delta_{wet} = -(9.29 \mu m/m) H_{rain} . \quad (13)$$

where H_{rain} is the rain height responsible for the recession. Since the rain height H_{rain} is defined as the rain volume V_{rain} per unit surface area, and assuming that $V_{rain} = V_{sol}$, i.e.

$$H_{rain} = V_{rain}/S_{stone} = V_{sol}/S_{stone} , \quad (14)$$

we have:

$$\delta_{wet} = -(9.29 \mu m/m) V_{sol}/S_{stone} . \quad (15)$$

where V_{sol} is the acidic solution volume and S_{stone} the stone's surface area.

Finally, since the recession is calculated according to Eq. 1, i.e.

$$\delta = \Delta V_{stone}/S_{stone} ,$$

we have:

$$\Delta V_{stone} = -(9.29 \mu m/m) V_{sol} . \quad (16)$$

where ΔV_{stone} is the stone's volume change during the recession.

Note that the stone's volume change during erosion depends only on the solution's volume, considering that the chemical recession products are continuously removed from the surface. Thus, deviations from the above law may be exhibited for a stone sample inside a still solution.

We can apply the above equations in the case of marble stone slabs (EL3 and ES1) undergone the acid accelerated experiments, and get some useful results. Using Eq. 14 or Eq. 12 we can compute the effective real time w.r.t. experiment exposure time for the acid accelerated experiments. For this computation the rainfall height at Elefsis is used, i.e. $H_{site}/t = 32.2 \text{ cm/yr}$; thus, the effective time represents the equivalent time that a marble stone should be exposed in Elefsis' environment to exhibit the same erosion as in the accelerated erosion chamber. The results are presented in Table 19. Note that 1 *day* in the acid accelerated chamber is equivalent to 3.0 – 3.6 *years* in the Elefsis environment.

Effective Time for the Acid Experiments							
Stone	t_{exp} days	V_{sol} L	S_{stone} cm^2	H_{rain} cm	H_{rain}/t cm/yr	H_{site}/t cm/yr	t_{eff} yrs
EL3 Acid $H_2SO_4 + HNO_3(aq)$	41	16	29.77	537.5	4784.8	32.2	148.6
ES1 Acid $H_2SO_4(aq)$	45	16	29.97	533.8	4330.0	32.2	134.5

Table 19: Computation of the effective time - exposure time relationship for the acid experiment.

Using Eq. 15 or Eq. 13 we can compute the effective erosion, i.e. the one that is being derived from the theoretical model and compare it with the experimental one. The results are presented in Table 20. These results affirm the compliance of the theoretically (model based) derived and experimentally measured values for erosion, for the case of the marble stone slabs EL3 and ES1 undergone the acidic accelerated experiments, since the absolute error is below $7.3 \mu m$, under the scanning precision.

Effective Erosion for the Acid Experiments				
Stone	δ_{eff} mm	δ_{exp} mm	$\Delta\delta$ mm	$\Delta\delta/\delta$ %
EL3 Acid $H_2SO_4 + HNO_3(aq)$	-0.0499	-0.0527	0.0028	5.3
ES1 Acid $H_2SO_4(aq)$	-0.0496	-0.0569	0.0073	12.9

Table 20: Comparison of the theoretical and experimental erosion values.

2.4.5 Effects of Common Erosion

In this section we are concerned with the problem of identifying whether or not a surface has been exposed to a common recession along the normal direction. The main issue lies in the fact that geometric measurements of eroding surfaces – that are taken over time – are missing an absolute reference frame. Manual and automatic registering methods naturally try to bring the surfaces as close as possible, thereby ignoring the common part of the surface-recession. In particular tools like ICP try to minimize the distance between two surface meshes which brings the meshes as close as possible to each other. That means that large "flat" corresponding areas are registered by this approach directly on top of each other and one loses the information about the absolute recession that took place in normal direction of the surface. However, in the following part we explain which effects still are observable if a common recession is present.

Illustration of the Measurable Effects of Common Erosion

In order to investigate how a common surface recession (resulting from erosion) exposes itself, we designed a basic simulation experiment and show the effect on artificial and measured meshes. Below we first illustrate and explain this on a 1D surface.

1D Illustration The measurable effect of a common erosion after surface registration can be already determined and explained using a 1D surface. In figure 43 the common erosion in normal direction of a simple 1D surface with a Gaussian shaped hole is illustrated. The top image shows the original uneroded surface along with the eroded surface. For the shown surface we assumed and simulated that a common recession along the surface-normal is happening. The material that is removed by this recession is shown as a red stripe. After a significant erosion of the surface the eroded surface lies behind (here under) the original surface. A registration that minimizes the distance between the surface points results in the registration that is shown in the bottom image of figure 43. There we can see that the recession perpendicular to the normal orientation of the surface has a widening effect (remaining red part) on the Gaussian shaped hole while the common surface recession (yellow stripe) is no longer directly observable.

Mesh Simulation We naturally observe the same if we perform an erosion simulation along the surface-normals of a surface that contains an artificial Gaussian bell-shaped 2D surface hole. The left image of figure 44 shows a color-coded difference between the uneroded and eroded surface. The light blue (turquoise) areas show no measurable difference while the red area shows the observable difference. After an alignment of the surfaces one can only detect the widening (red-blue colored) of the hole and we are not able to observe the common surface recession directly within the

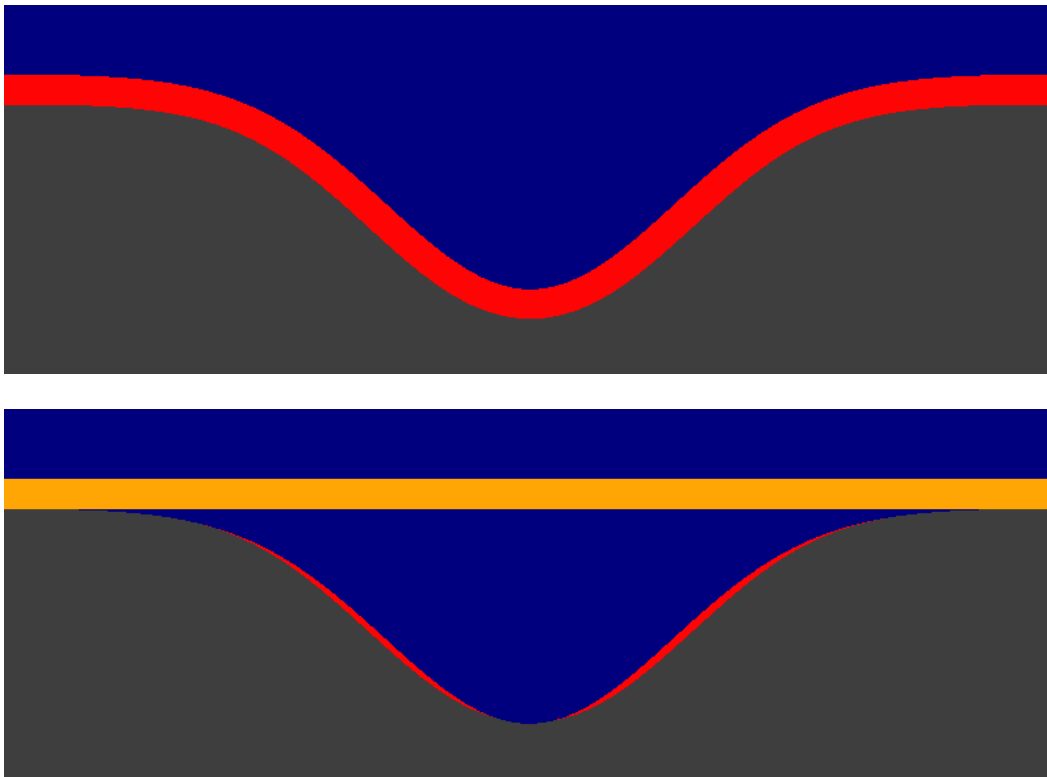
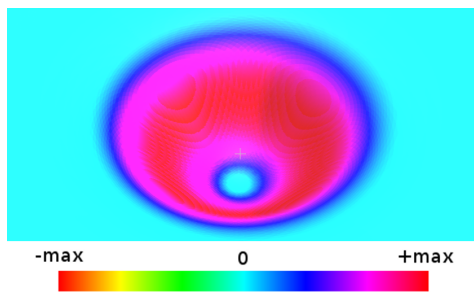
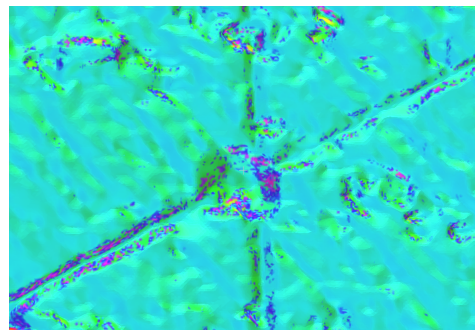


Figure 43: 1D Illustration of a recession along the normal of the surface. **Top:** Initial Shape representing a surface with a Gaussian shaped hole together with the surface shape after a significant erosion along the normal direction of the surface. The red stripe represents the material that is removed by this recession. **Bottom:** The two surfaces after registration. The remaining observable difference is represented by the red areas and shows that there is a widening effect of the original hole. Note that the information about the common erosion (yellow stripe) is lost.



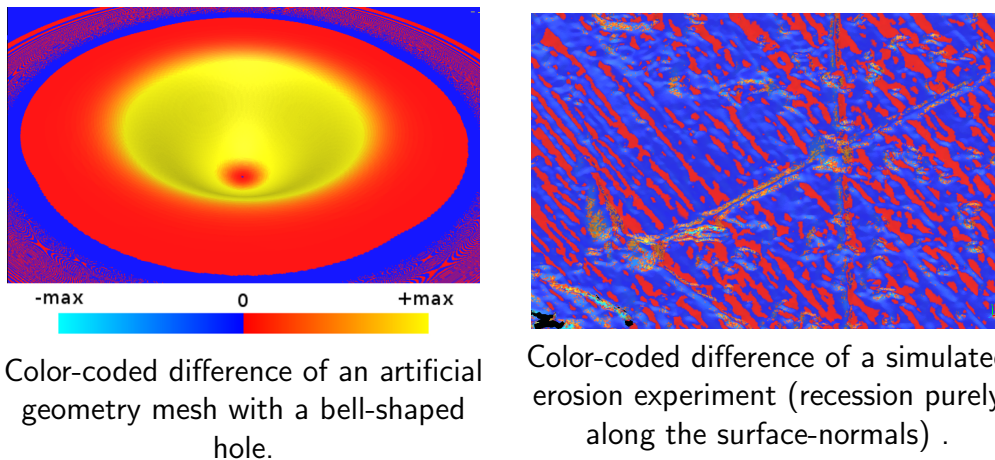
Color-coded difference of an artificial geometry mesh with a bell-shaped hole.



Color-coded difference of a simulated erosion experiment (recession purely along the surface-normals) .

Figure 44: Color-coded difference of two artificially eroded geometry meshes. On the left side a flat surface with a bell-shaped hole and on the right side a surface patch that is taken from a measurement of the X-Mason Mark.

flat parts (turquoise colored). The right image of figure 44 shows what we expect to see if common erosion is taking place on a real mesh of a stone wall. This example is created by an artificial erosion in normal direction of a real measurement mesh of the Nidaros Cathedral (The wall patch with the X-mason mark). We can observe a widening effect perpendicular to the grooves and in the center area with the hole. Figure 45 shows essentially the same as figure 44, but using a different color-code to visualize the mesh-differences in a more sensitive way. Zero-crossings are visible by a (discrete) change from red to blue and extreme values appear turquoise and yellow.



Color-coded difference of an artificial geometry mesh with a bell-shaped hole.

Color-coded difference of a simulated erosion experiment (recession purely along the surface-normals) .

Figure 45: More sensitive color-code to visualize the difference of the two artificially eroded geometry meshes also shown in figure 44. Zero-crossings are visible as a hard transition between red and blue.

2.4.6 The Erosion Simulator Module

The Erosion Simulator Module is the software implementation of the erosion modeling as described in section 2.4. The final version of the software application operates in four “operating modes”:

Mesh Offsetting: assumes a 3D surface mesh data and applies a simple offsetting model, for simulating a pre-calculated recession or deposition process occurring on a stone surface.

Mesh Data Only: assumes 3D surface mesh data and homogeneous stones; applies a chemical model, the same on every vertex, for simulating the chemical degradation processes that occur on a stone surface.

Mesh & QEMSCAN Mineral Data: assumes 3D surface mesh data textured with mineral map QEMSCAN data for non-homogeneous stones; applies a chemical model, different on every vertex according to its chemical attributes, simulating the chemical degradation processes that occur on a stone surface.

Mesh & “Stone Builder” Mineral Data: assumes 3D surface mesh data textured with mineral map data generated with the “Stone Builder” for non-homogeneous stones.

Chemical processes are modeled according to the aforementioned “Weathering models” (see Section 2.4.2). Offsetting processes are modeled according to three different “Weathering models”, which leads to the computation of the mesh offsetting δ_i for the following cases:

Constant offsetting: with δ_i a pre-defined constant value.

Random offsetting: with δ_i values that come from a normal distribution with pre-defined mean value and standard deviation.

Smoothing/Roughening: with δ_i values that come from the equation $\delta = \mu \|\nabla^2 \mathbf{p}\|$, where μ is a user-defined rate.

This extension is included to simulate simple mechanical erosion mechanisms (due to wind or water), which have a smoothing or roughening result or even constant or random recession effects on stone’s surface.

2.4.7 The Stone Builder Module

The stone builder module is used to synthetically create physico-chemical stone data. It synthesizes stone-material – in terms of a defined chemical color-code – from a given 2D stone-texture-image onto an irregular surface-mesh. One of the goals/constraints of the implemented sampling method is to preserve the original mesh and we adopted a sampling approach that works reasonably well for regular pixel-grids. In its current version the stone-builder allows the synthesis of stone-material which resembles the statistically correct distribution of the chemicals along with a synthesis that incorporates longer range correlations. The latter approach leads to a more realistic looking surface of the stone-material but influences the original given distribution of the chemicals. The stone-builder accepts an arbitrary texture image as input. If the physico-chemical stone data (i.e. a QEMSCAN-image) is used as input the resulting textured mesh can be subsequently used for the stone degradation simulation.

Brief Methodological Description

We briefly summarize the two main concepts behind the used methods to sample stone material onto an arbitrary mesh. Exploiting the inverse of the cumulative distribution function $F(x) = \int_{-\infty}^x h(t) dt$ of the distribution/histogram $h(t)$ of the material we can transform uniform distributed random variables such that they appear to be drawn from the initial distribution/histogram function $h(x)$. In our implementation this allows us to use standard uniform random variables $u \in [0, 1]$ to create random variables that follow a given histogram distribution. Applying this method to an arbitrary mesh each vertex of the object is sampled independent from its neighborhood. In order to incorporate also longer range correlations that are present in the initial

texture image we implemented a texture synthesis approach that is based on a variant of non-parametric sampling approaches (introduced by Efros and Leung [EL99]). In this approach the local neighborhood of a vertex in the object-mesh is projected onto a regular 2D grid which serves as template for finding good material candidates with a similar neighborhood in the given example texture image. The finally selected material is randomly sampled from the candidate list. This sampling approach can be seen as a simplification of Markov Random Field (MRF) based sampling and leads to visual improved stone-texture. We evaluate the output of these methods in section 2.5.9.

2.5 WP3 Evaluation Experiments and Results

According to the [Evaluation Plan \(D5.1\)](#) the method of evaluation is based upon application scenaria, i.e. realistic scenaria that are defined to address WP3 objectives. An application scenario is parameterized for execution by defining the data that it will operate upon and the ground truth data that it will be evaluated against; it thus forms an experiment. The relationship between application scenaria and experiments is 1-many. A scenario and consequently, an experiment, is evaluated through evaluation criteria which provide the evaluation feedback.

The objectives of WP3 are the estimation and prediction of monument degradation. The following application scenaria are typical use-cases that correspond to these objectives as described in the [Evaluation Plan \(D5.1\)](#):

Object Erosion - Surface Geometry Only (E-GE): In the Erosion-GEometry only (E-GE) scenario the input is geometric surface data of a known stone type. The erosion simulator produces the eroded surface geometry after certain period(s) of time, given a set of erosion parameters. The output surface can be displayed.

Object Erosion - Surface Geometry and surface physico-chemical data (E-GESC): In the Erosion-GEometry and Surface Chemistry (E-GESC) scenario, the input is physico-chemical data samples over the surface geometry. The surface monitored will be limited to an area of a few millimeters provided by the QEMSCAN mineral analysis. The surface physico-chemical data for larger areas may be synthetically generated (by the Stone Builder) from known QEMSCAN samples.

The experiments planned for WP3 follow and are based on the application scenaria defined above and the description of the fulfillment of the evaluation criteria for these scenaria experiments follows.

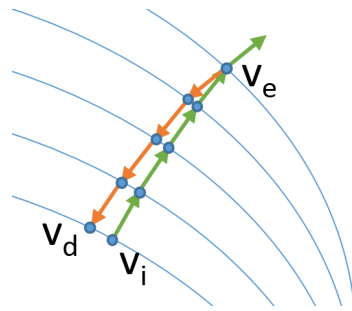


Figure 46: Vertex v_i movement during erosion v_e and dilation v_d .

2.5.1 Time Reversal

The aforementioned scenario concerned the forward (in time) projection of the erosion prediction process as well as reverse erosion prediction (going back in time), according to the [Evaluation Plan \(D5.1\)](#). However, since erosion is a non-deterministic physico-chemical process with inherent loss of information, reverse erosion is a highly divergent approximate process.

Generally speaking the mesh offsetting Equation 4 is not reversible by just reversing the sign of the erosion rate. This is actually true, since for every iteration the normals of the vertices in the new state are changed in direction, and thus going back to the vertex of the initial state where you came from is not feasible, by just reversing the sign of the moving direction (see Figure 46).

In practice, when the erosion rate is infinitesimally small and the iterations not so many, reversing the sign of the erosion rate would lead to the initial state with typically negligible error. This resulting error is typical in situations where a path integral has to be computed, such as in a single mass movement in a force field.

This phenomenon is presented in Figure 47, where the dragon model is eroded and then dilated back to the original. The error in such a procedure is negligible as one can notice, but this is not true for the general case. In such a case the object can be actually deformed by the dilation process and the result be not at all realistic.

2.5.2 C-WP3-1. Erosion prediction geometric accuracy

E-GE-1 & E-GE-2 experiments In this section we show our evaluations concerning the ground truth geometric measurement data of the cultural heritage sites. For visualizing the changes that are observable in the differential scan data we used selected patches of the cultural heritage sites and computed the surface distance between the measurement rounds. The Elefsis column was scanned 3 times:

Round01: 20.03.2013, Round02: 14.10.2014, Round03: 24.11.2015

The part of the wall at the Lectorium East with the masonmarks at Nidaros were scanned three times:

Round01: 10.04.2013, Round02: 24.09.2014, Round03: 03.12.2015

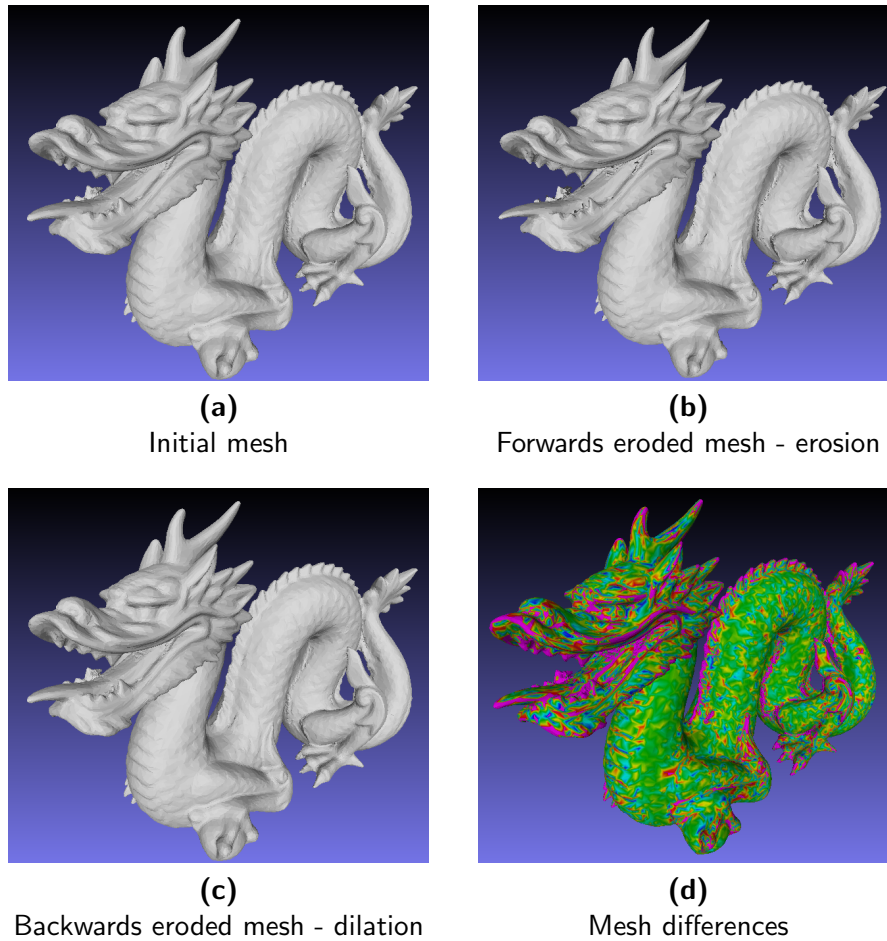


Figure 47: Depiction of mesh erosion and mesh restoration by erosion reversal i.e. dilation on the dragon model: **(a)** Initial mesh; **(b)** Eroded mesh by applying an offset of -0.008 for 10 cycles; **(c)** Restored mesh by applying an offset of $+0.008$ for 10 cycles on the eroded model (b); and **(d)** Depiction of the mesh differences (colour-coded for the range ± 0.0001) between the initial model (a) and the restored one (c).

In figure 48 the color-coded differences (see figure 49 for the legend) of four selected patches (two for each Cultural Heritage site) between the measurement rounds are shown. In the first column the differences between the meshes from the first and third measurement round (round 01 and round 03) are displayed. The second column shows the differences between measurement round 01 and round 02 and the last column shows the differences between round 02 and round 03.

Figure 49 shows a close-up-view for one mesh from the Elefsis-column and one from the Nidaros Cathedral. One main observation we can make when we look closer onto the surfaces of the cultural heritage objects (see figure 49) is that on a microscopic level the erosion happens in a more non-predictable fashion with randomly distributed grain-removals.

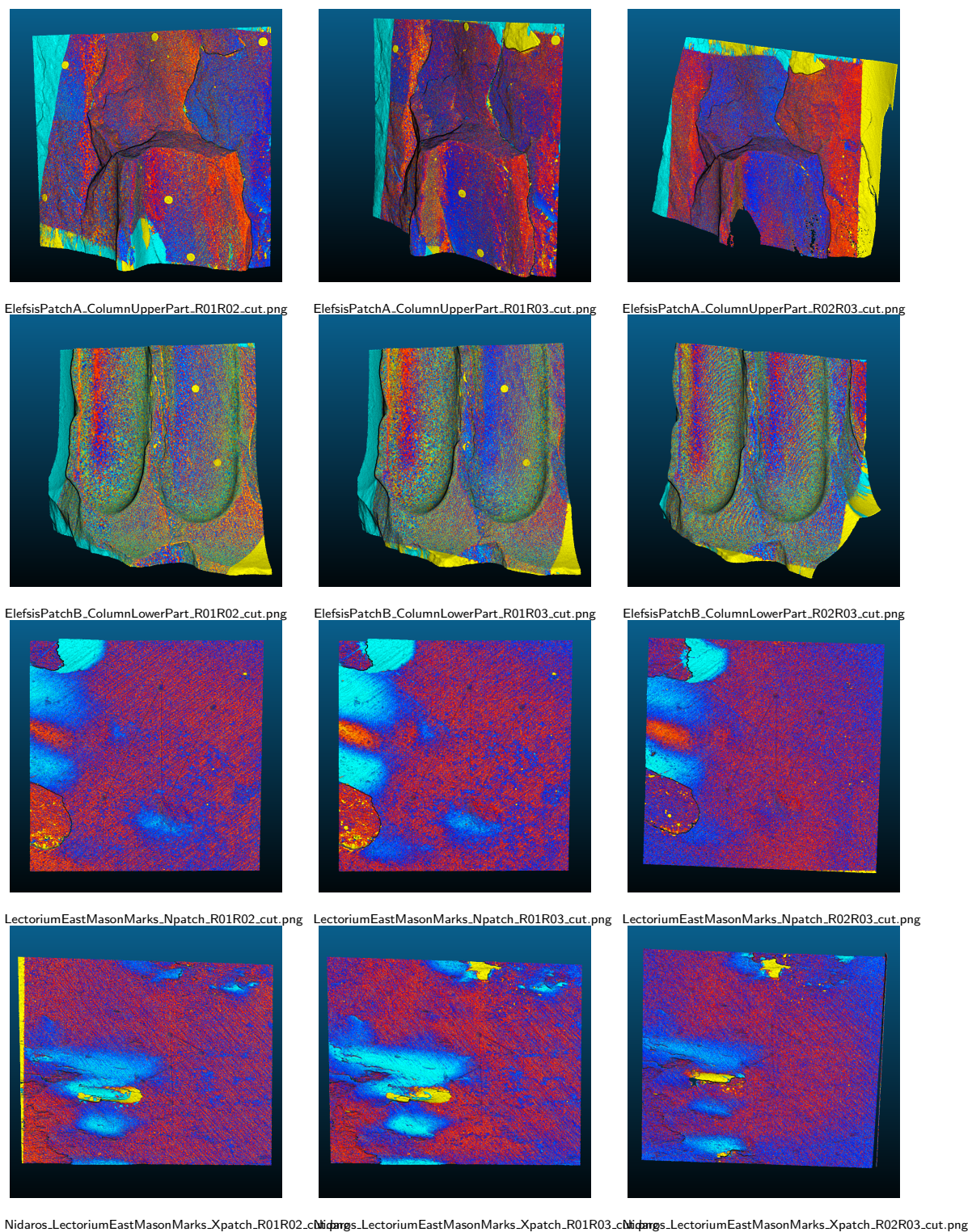


Figure 48: Differences on selected patches from the cultural heritage sites. The first two rows show patches from Elefsis and the last two rows from Nidaros. The first column shows the differences between the first and the second round of scans. The middle column shows the difference between the first and third round. The last column indicates the change from second to third scanning round.

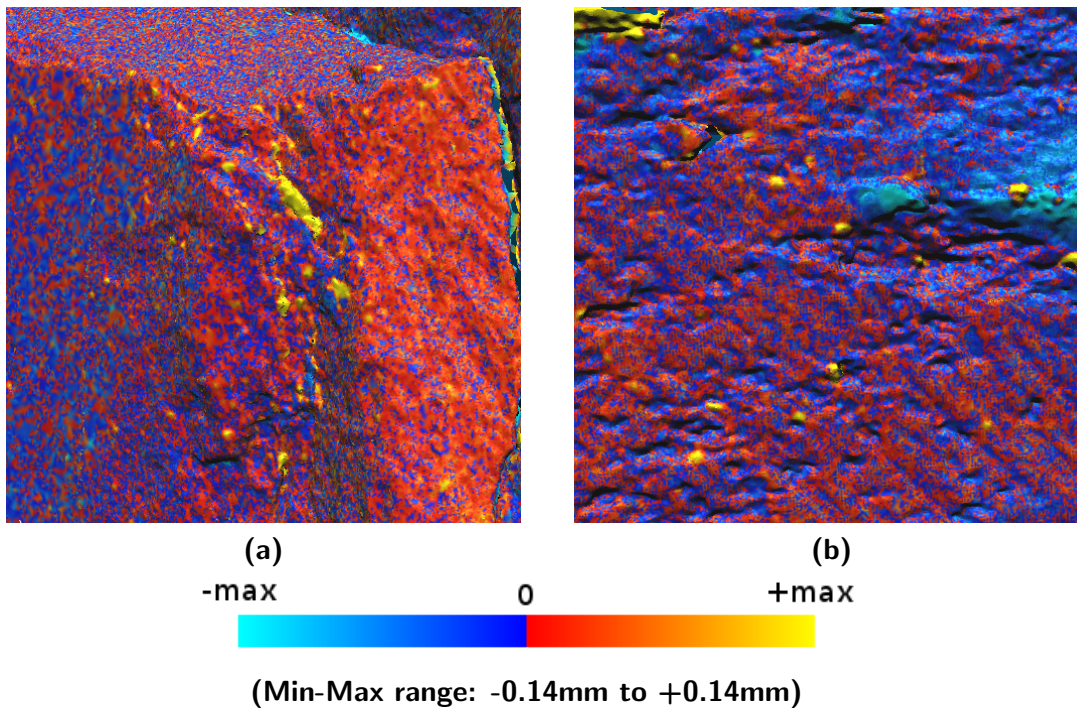


Figure 49: Close-up view for one mesh from the Elefsis-column (a) and one from the Nidaros Cathedral (b). One can observe that the erosion is taking place by the removal of small randomly distributed parts (yellow).

Common Erosion Evaluation on Real Measurement Data Over time a common erosion might have happened at the cultural heritage sites and we searched for signs (discussed in section 2.4.5) on the difference meshes (figure 48) that indicate the presence of this type of erosion. However, when we compare the measurable effects that a common erosion has on the artificial erosion experiments (shown in figure 45) with real differential measurements (see in particular the close-up view in figure 50) we find that such effects are not yet observable on our real cultural heritage objects. It seems that the observation time has to be longer for being able to observe and measure common erosion on the measurements. This is even more understandable when we look at the magnitude of erosion we expect to have happened within the time-frame of the project:

According to the computations of section 2.4.3, the erosion due to rain recession at the two CH sites is in the range of $6 \mu m - 20 \mu m$ which is just about the same as the scanner accuracy. And as we expect the widening effect to be just a fraction of this length (compare figure 43) we see that this is below the accuracy of the scanner and also below the ICP registration error, or the accuracy of the differential measurer (due to the data and the way the distance is computed, see Eq. 3).

However, in the measurements of the Nidaros wall with the mason marks we observe much change in the already present flake area and we see likely a new flake developing (light blue). Some of the other changes we see come from material removal but many are due to measurement noise introduced during the scanning process and as the meshes also differ slightly in the resolution, the mesh differences appear more

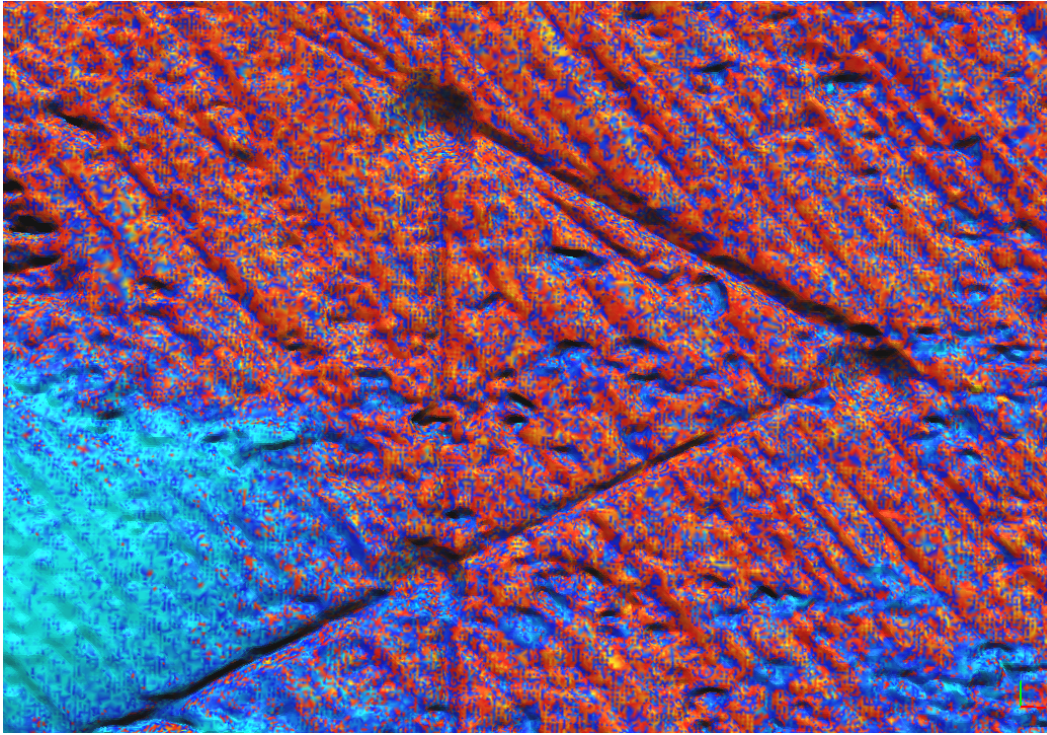


Figure 50: Difference of the real measurement geometry meshes from round 1 and round 3 (respectively 2013-04-10 and 2015-12-03) of the Nidaros Cathedral. The patch includes the X-Mason Mark.

randomly. Therefore, at this stage we conclude that we do not observe a common erosion as a systematic widening of the structures within the time-frame of our measurements (2 years, 7 months, 24 days) is not clearly present. The main erosion process on microscopic level seems to be the removal of very small randomly distributed particles and an observable common erosion develops as a result of this more chaotic grain-removal over a long time.

E-GE-3 experiments In this kind of experiments, the surface geometry of the Nidaros slabs and Elefsis slabs is measured. The slabs are subjected to accelerated aging and their surface geometry is measured again. The erosion simulator is parameterized and applied to the above data. The measured experimental values are compared against the erosion simulator output.

We have performed all the E-GE-3 experiments, according to the [Evaluation Plan \(D5.1\)](#), (see Section 2.1.3 and Table 5), we have taken all the appropriate measurements and computed the relevant mean erosion values (see Section 2.3). As it is already described some deviations and difficulties arose from the performed experiments and measurements, difficulties which eventually made the evaluation process infeasible in a number of cases, for the following reasons:

- The erosion model (see Eq. 7), which has been implemented in the erosion

simulator, is only applicable to calcium carbonate stones (i.e. marble) exposed to acid rain polluted by SO_2 and NO_2 . Thus actually, there is no model for such as “complicated” stones as soapstones to be evaluated.

- For a strict evaluation of the erosion model, the acidic accelerated erosion chambers should be consistent with the chambers described in [GB99, YCJ*96], thus allowing SO_2 and NO_2 in gas form to enter the chambers and perform the erosion, but this was not allowed by the Chemistry Dept. for safety reasons. Thus, using SO_2 and NO_2 dissolved in aqua solutions can not be used for fully evaluating the erosion model, but only the “wet” part that is caused by the rain only, i.e. the Baedeker part (see Eq. 8).
- The environmental parameters used in the model can only be related to the chemical parameters of the acid solution erosion chambers for the “wet” part (see Eq. 8). Therefore it was not feasible to run the erosion simulator by direct application of the environmental parameters supported by the model. We thus opted for the direct application of a computed geometrical erosion offset to the mesh. This offset is computed as shown in Section 2.3.
- The Nidaros slabs exhibited an unexpected swelling behaviour in both acid solution chambers; this has not yet been interpreted or modeled and thus can not be evaluated. Also during the second period (R02 to R03) of the accelerated erosion experiments marble stones showed also such a swelling behaviour, making things more complicated.
- To the best of our knowledge no model is for the time being available for the freeze-and-thaw with rain effect or the salt effect, and the experimental data are not sufficient for establishing such a model.

From the performed E-GE-3 experiments the ones following marble slabs / erosion chambers are exploitable:

- ES1 in H_2SO_4 aqua solution erosion chamber
- EL3 in $H_2SO_4 + HNO_3$ aqua solution erosion chamber

Let us first define some terms:

- δ_{model} represents the average amount of erosion predicted by the erosion model; this is considered constant for all vertices in the case of a homogeneous stone.
- δ_{exp} represents the average amount of erosion computed from the measurements taken before/after an erosion experiment (see Tables 12 and 13).
- $\delta_{model}(\mathbf{v})$ represents the amount of erosion predicted by the erosion model on a vertex \mathbf{v} .

- $\delta_{exp}(\mathbf{v})$ represents the amount of erosion computed from the measurements taken before/after an erosion experiment on a vertex \mathbf{v} .

Ideally we should evaluate two things:

- The compliance of the predicted δ_{model} with δ_{exp} .
- The compliance of the predicted $\delta_{model}(\mathbf{v})$ with $\delta_{exp}(\mathbf{v})$.

Since actually for solving the “common erosion” registration problem we used the experimentally computed mean erosion value δ_{exp} to displace the slab in the Z direction, the mean value of $\delta_{exp}(\mathbf{v})$ equals (or is too close) to the δ_{exp} .

As it was not practical to run the chemical erosion model (see Eq. 7), for the reasons outlined above, we opted for measuring the compliance of δ_{exp} with $\delta_{exp}(\mathbf{v})$, which essentially evaluates the compliance of the geometric part of the erosion model (see Eq 4). This was performed by applying the constant value δ_{exp} to all vertices and comparing it with the per-vertex values $\delta_{exp}(\mathbf{v})$.

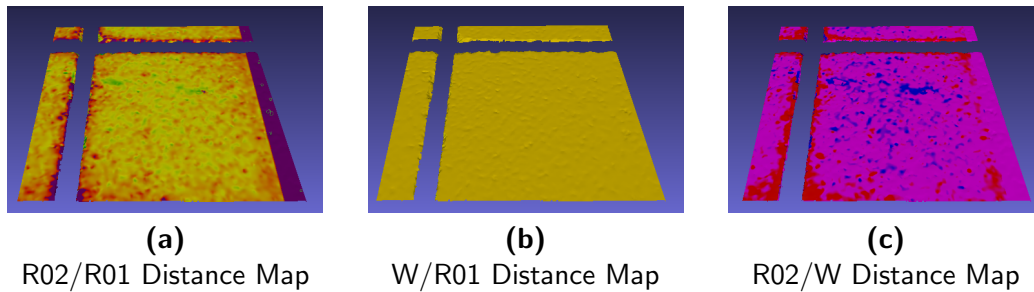


Figure 51: Distance maps between different meshes of the stone slab Elefsis Small 1 (ES1): **(a)** Distance of Round 1 mesh (R01) from Round 2 mesh (R02) mapped in the interval of $[-0.1mm \sim +0.1mm]$; **(b)** Distance of Erosion prediction mesh (W) from Round 1 mesh (R01) mapped in the interval of $[-0.1mm \sim +0.1mm]$; and **(c)** Distance of Round 2 mesh (R02) from Erosion prediction mesh (W) mapped in relative scale (red under-estimation/blue over-estimation).

Figures 51 and 52 depict the distance maps (i.e the $d_e(\mathbf{m}_i)$) between various meshes of Elefsis Small 1 and Elefsis Large 3, and consequently the experimental erosion measure (Figures 51 (a) and 52 (a)), the predicted erosion measure (Figures 51 (b) and 52 (b)), and the prediction error (Figures 51 (c) and 52 (c)) mapped on the initial meshes.

From the above, the following conclusions for the geometric model of the erosion can be drawn:

- The simulated erosion is smaller than the observed erosion close to the edges of the mesh.

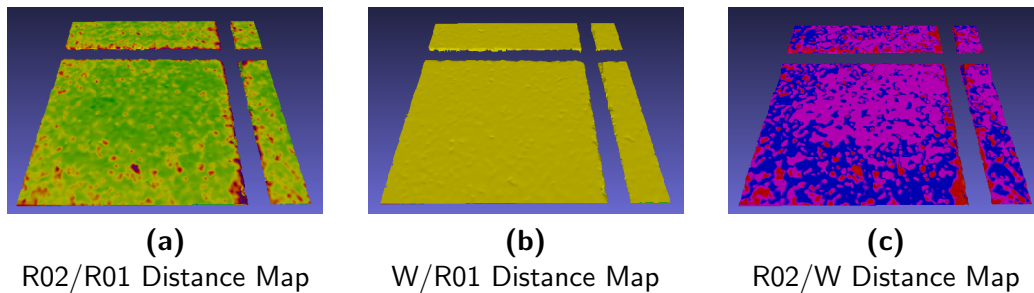


Figure 52: Distance maps between different meshes of the stone slab Elefsis Large 3 (EL3): **(a)** Distance of Round 1 mesh (R01) from Round 2 mesh (R02) mapped in the interval of $[-0.1mm \sim +0.1mm]$; **(b)** Distance of Erosion prediction mesh (W) from Round 1 mesh (R01) mapped in the interval of $[-0.1mm \sim +0.1mm]$; and **(c)** Distance of Round 2 mesh (R02) from Erosion prediction mesh (W) mapped in relative scale (red under-estimation/blue over-estimation).

- The overall geometric erosion prediction is close to the experimentally measured values.
- The experimentally measured values show a more random behaviour.

These are the reasons why the Erosion Simulator is enhanced with erosion processes such as “Random Offsetting” and “Smoothing/Roughening” erosion.

E-GESC-1 and E-GESC-2 experiments The objective of these experiments is the extraction of a physico-chemical model that predicts the erosion in relation with the mineral that is identified on the surface of a stone. According to the [Evaluation Plan \(D5.1\)](#), the erosion prediction should be modeled and the accuracy of the prediction against the experimental ground-truths should be evaluated.

Unfortunately, this modeling proved to be infeasible. This is also justified by the chemist and geologist we used as expert advisors, since the erosion processes are highly complicated having interrelated chemical and physical causals. As described in Section 2.3.5 the corresponding E-GESC experiments have been performed and the geometrical and physico-chemical data were measured on the surface of the Nidaros and Elefsis slabs subjected to accelerated erosion. The performed analysis through the mineral related erosion computations, didn’t show any “canonical” behaviour for the erosion that could be computationally modeled. The results of the per mineral erosion computations are presented in Table 16. Note that the column “rel” which represents the relative erosion for every mineral w.r.t the erosion that “Calcite” exhibits, doesn’t show any reliable behaviour.

2.5.3 C-WP3-2. Erosion prediction physico-chemical accuracy

The objective of these experiments is the extraction of a physico-chemical model that predicts the physico-chemical changes present in an erosion process, and the incorporation of this model into the Erosion Simulator. According to the [Evaluation Plan \(D5.1\)](#), the erosion prediction concerning the chemical composition of the eroded object should be investigated and the accuracy of the prediction against the experimental ground-truths should be evaluated.

Unfortunately, this modeling proved to be infeasible. This is also justified by the chemist and geologist we used as expert advisors, since the erosion processes are highly complicated having interrelated chemical and physical causals. As described in Section 2.3.5 the corresponding E-GESC experiments have been performed and the geometrical and physico-chemical data were measured on the surface of the Nidaros and Elefsis slabs subjected to accelerated erosion. The performed analysis (through the mineral composition and mineral transition matrices computations) of the physico-chemical data before and after erosion, didn't show any significant "canonical" behaviour that could be computationally modeled.

2.5.4 C-WP3-3. Erosion prediction geometric robustness

According to the [Evaluation Plan \(D5.1\)](#), erosion prediction geometric robustness in the presence of noise, holes, spikes and missing data will be examined against the existing or synthetically created input data. This investigation applies to all E-GE and E-GESC experiments.

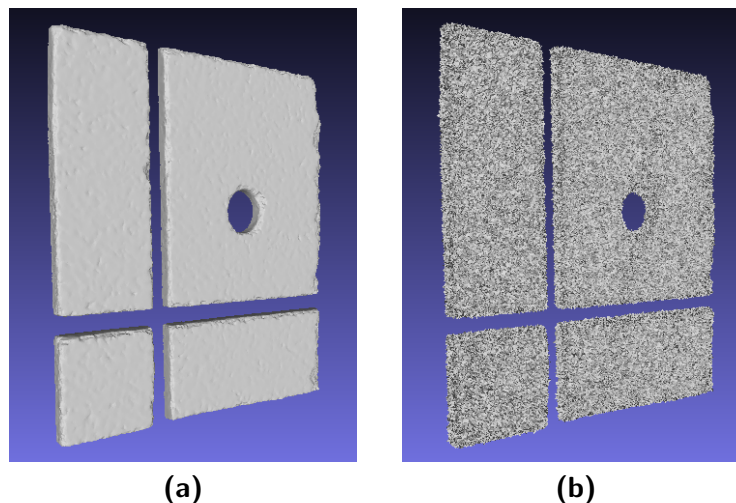


Figure 53: Depiction of EL3 surface mesh: **(a)** Scanned mesh exhibiting holes and missing areas; and **(b)** Noisy mesh derived from the scanned mesh by addition of Gaussian noise.

The scanned 3D meshes of the slabs include holes and missing data, e.g. cross groove and drilled hole in Figure 53 (a). In Figure 53 (d), extra Gaussian noise is added on the scanned mesh, using the random offsetting functionality (Operating mode: Mesh

Offsetting and Weathering model: Random offsetting) of the Erosion Simulator (see Section 2.4.6). Despite these, the erosion process of the simulator runs smoothly without any preprocessing.

2.5.5 C-WP3-4. Erosion prediction physico-chemical robustness

According to the [Evaluation Plan \(D5.1\)](#), erosion prediction physico-chemical robustness (in the presence of noise and missing data) will be measured from the physico-chemical accuracy deviation resulting from variations in the amounts of noise and missing data in the chemical composition. This applies to the E-GESC experiments.

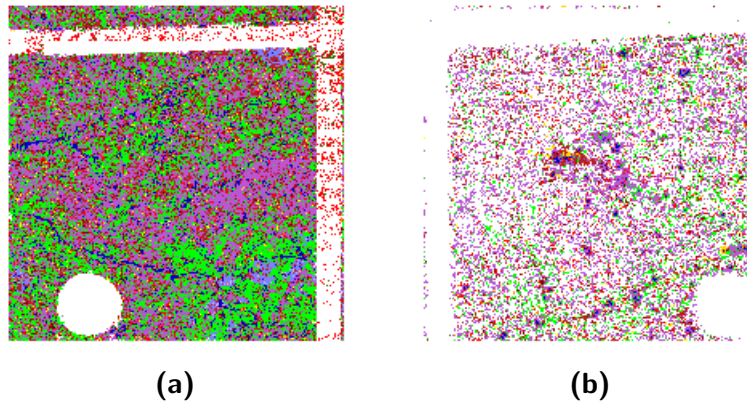


Figure 54: Depiction of QEMSCAN images containing missing and noisy data from Round 02 scans: **(a)** NBL1 - notice the missing data (white pixels), pores (blue pixels), and noisy data (not white pixels) in the grooves; and **(b)** NBL2 - notice the missing data (white pixels) due to the surface roughness.

The QEMSCAN data which contain the physico-chemical information (minerals) of the stone slabs include holes, missing data, pores and noise (see Figure 54). This issue is addressed at the registration phase of the 3D geometry scans with the QEMSCAN data. When missing data (white pixels or blue pixels) are detected on the mineral map a hole is created on the registered regular mesh. Of course this may lead in a case when the reconstructed mesh is not contiguous, consisting of islands of meshes, and of course in this situation, although the erosion simulation can run, the results are unreliable (see Figure 55).

2.5.6 C-WP3-5. Erosion prediction tolerance against object geometric resolution and scale variations

According to the [Evaluation Plan \(D5.1\)](#), two issues are to be investigated here. First, whether the simulator runs smoothly on meshes digitised at different resolutions and, second, the sensitivity of the results to changes in mesh resolution; this applies to all E-GE and E-GESC experiments.

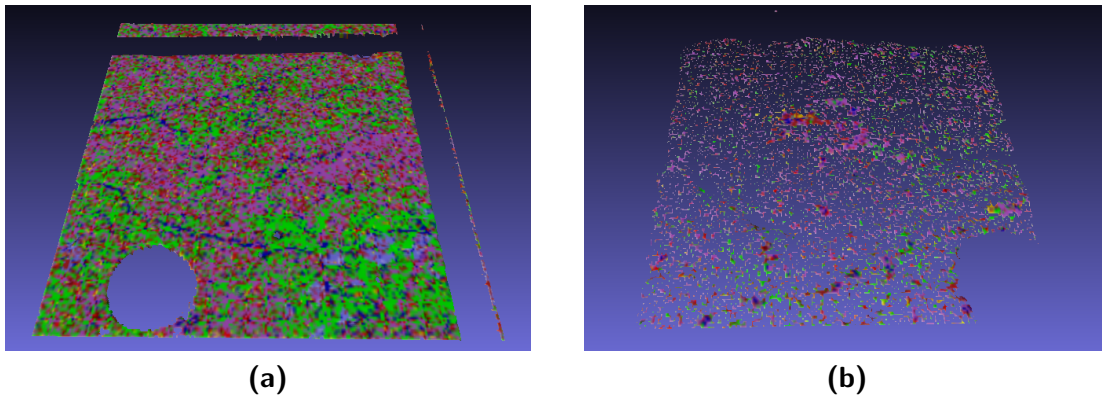


Figure 55: Depiction of physico-chemical mesh data from Round 02 QEMSCANs registered with the 3D surface scans: **(a)** NBL1 - notice the corrected resulting data from the combination of the QEMSCAN and the resampled mesh surface; and **(b)** NBL2 - notice the resulting missing data due to missing data of the QEMSCAN.

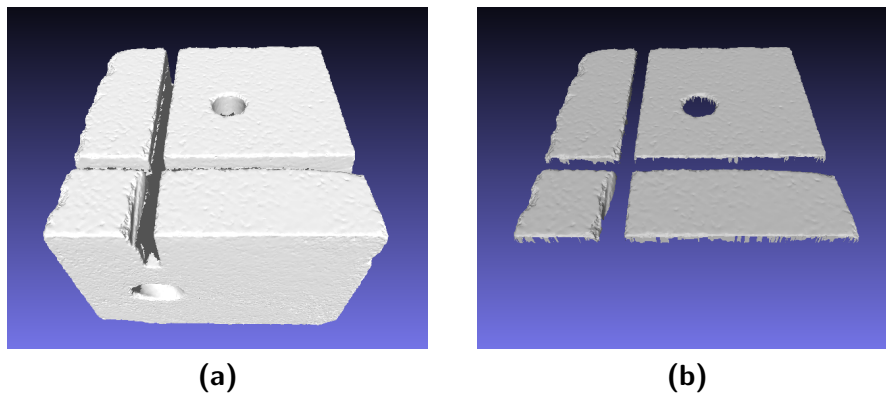


Figure 56: Depiction of mesh of the stone slab Elefsis Large 1 (EL1): **(a)** the complete scanned irregular mesh; and **(b)** the regularly resampled frontal area.

For the first case, the simulator ran with no problem on various complete irregular meshes acquired at different resolutions with mean-edge-length at $0.060 \sim 0.098\text{mm}$ (see Figures 56 (a) and 57 (a)) and on various regular meshes re-sampled at different resolutions with mean-edge-length at $0.035 \sim 0.050\text{ mm}$ (see Figures 56 (b) and 57 (b)) without any problems. These regular meshes are also used in combination with the QEMSCAN physico-chemical data.

For the second case, we evaluated the sensitivity of the results to changes in the mesh resolution; to this end, we regularly re-sampled the frontal meshes at two different resolutions (Figures 57 (a) and 57 (b)). The result of the erosion applied on a 1024×1024 regularly sampled mesh (mean-edge-length at 0.035 mm) and 256×256 regularly sampled mesh (mean-edge-length at 0.140 mm) is depicted in Figure 58 as a colored difference map. The simulator runs with no problem in the above mentioned cases.

Mesh folding is exhibited when extreme erosion values are applied on dense surface

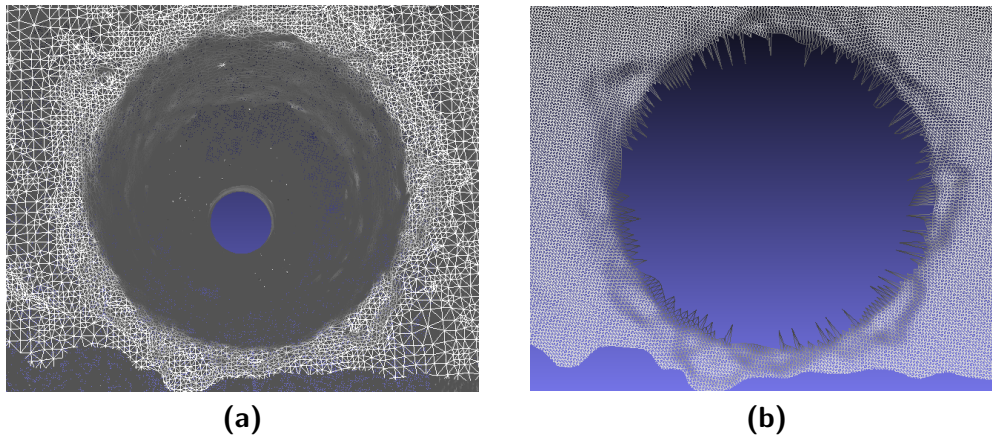


Figure 57: Detail of the mesh of the stone slab Elefsis Large 1 (EL1) near the hole area: (a) the initial irregular mesh; and (b) the regularly resampled area.

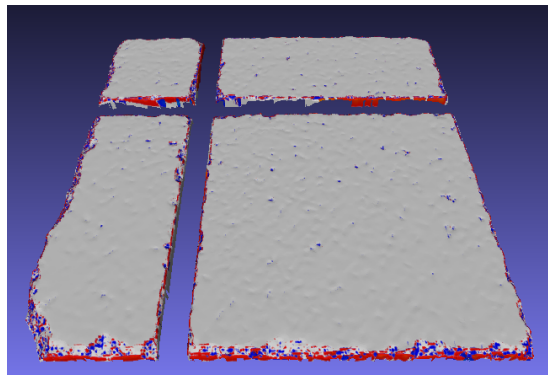


Figure 58: Difference map between the eroded meshes at 1024×1024 sample vertices and 256×256 sample vertices (blue under-estimation/red over-estimation).

meshes (see Figure 59). This is a very common problem appearing in mesh offsetting procedures, which is not completely tackled in existing literature. We are in progress to address this as a self-contained research issue by developing a separate correction tool.

2.5.7 C-WP3-6. Erosion prediction tolerance against object physico-chemical resolution and scale variations

The issue involved here, according to the [Evaluation Plan \(D5.1\)](#), is to investigate whether the simulator runs smoothly on meshes with registered physico-chemical data that come from different resolutions/scales; this applies to E-GESC experiments. Although available QEMSCANs come with different resolutions - at $100 \mu m$ and at $10 \mu m$ interpixel distance - (see Figure 28), the high resolution ones weren't exploited due to the lack of reference points necessary for the registration procedure with the available geometry scans. Thus, this kind of evaluation wasn't feasible. We also have to note here that the actual resolution of the $100 \mu m$ is $\approx 91 \mu m$. This value came up during the registration procedure of the QEMSCANs with the 3D geometry

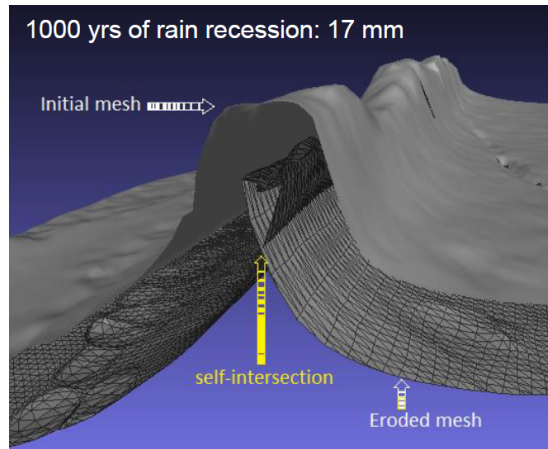


Figure 59: Mesh folding is exhibited when extreme erosion values are applied on dense surface meshes.

images of the meshes, using exact corresponding reference points, such as the center of the grooved cross and the center of the drilled hole.

2.5.8 C-WP3-7. Erosion prediction procedure complexity and absolute processing time evaluation

Erosion Simulator

According to the [Evaluation Plan \(D5.1\)](#), the erosion prediction algorithm complexity will be determined and the processing times will be experimentally measured; this applies to all E-GE and E-GESC experiments. The complexity of the current version of the erosion simulator is linear in the number of vertices of the mesh being eroded. Some typical running times on an Alienware computer (Intel Core i7 @ 3.6 GHz, 16 GB RAM) are given in Table 21.

Running times			
Stone	facets	vertices	t (sec)
EL3^(a)	295,643	149,451	3.01
EL3^(b)	1,960,187	983,698	18.38
ES1^(a)	278,244	140,690	2.77
ES1^(b)	1,296,290	652,069	12.18

Table 21: Comparison of the proposed erosion computation running times over Elefsis Large 3 (EL3) and Elefsis Small 1 (ES1) slabs: (a) on the regularly resampled frontal area; and (b) on the whole scanned irregular mesh

The current version of the erosion simulator is therefore near real-time for relatively small meshes, allowing the user to experiment with various scenaria.

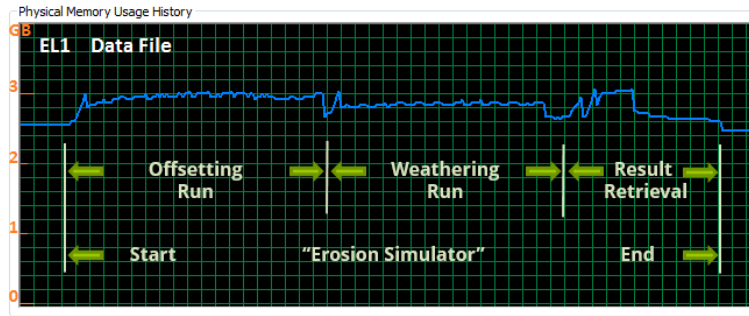


Figure 60: Memory usage of the Erosion Simulator for stone slab “EL1” for different operation modes.

The memory usage of the Erosion Simulator for the two modes of operation (offsetting mode and weathering mode) is depicted in Figure 60.

Stone Builder

The algorithm of the stone builder (see section 2.5.9) is implemented in a straight forward fashion. For each vertex we sample a new color the neighborhood is examined and converted into a 2D mask of maximum size $d_{mask} \times d_{mask}$. This mask is used for finding the best candidates within the example image of size $d_{image} \times d_{image}$. As this template matching corresponds to a filtering of the image with a mask an estimate of the complexity results in

$$T(n_s) = n_s d_{mask}^2 d_{image}^2 \quad (17)$$

where n_s refers to the numbers of vertices in the mesh. This shows that the algorithm is linear in the numbers of vertices n_s we wish to sample on the surface mesh. However, other important variables that influence the running time are the size of the example image (d_{image}^2 where we assume a squared image with $d_{image} \times d_{image}$ pixels) and the size of the used mask ($d_{mask} \times d_{mask}$). Therefore, increasing the mask-size or the example image results in a quadratic dependency on d_{mask} and d_{image} . Some heuristics we use, like an early abortion when looking for the best candidate-positions, do not influence the complexity, but make the algorithm more efficient.

2.5.9 C-WP3-8. Stone Builder’s synthetic stones consistency against real stone materials

In this section we evaluate the consistency of the results of the sampling methods we implemented in the stone builder module and which were briefly explained in section 2.4.7; of the two afore mentioned sampling methods. A chemical color-code measurement (QEMSCAN-image of Nidaros Bad Small 01) that is shown on the left side of figure 61 serves as example image. Note that the white background color

within the sample patch is not considered as material. The middle image of figure 61 shows a typical sampling result one obtains by sampling from the initial material distribution. A 2D result we obtain from the non-parametric sampling (neighborhood of $2*d+1 \times 2*d+1$ pixels with $d=3$) is shown on the right side of the figure 61. One

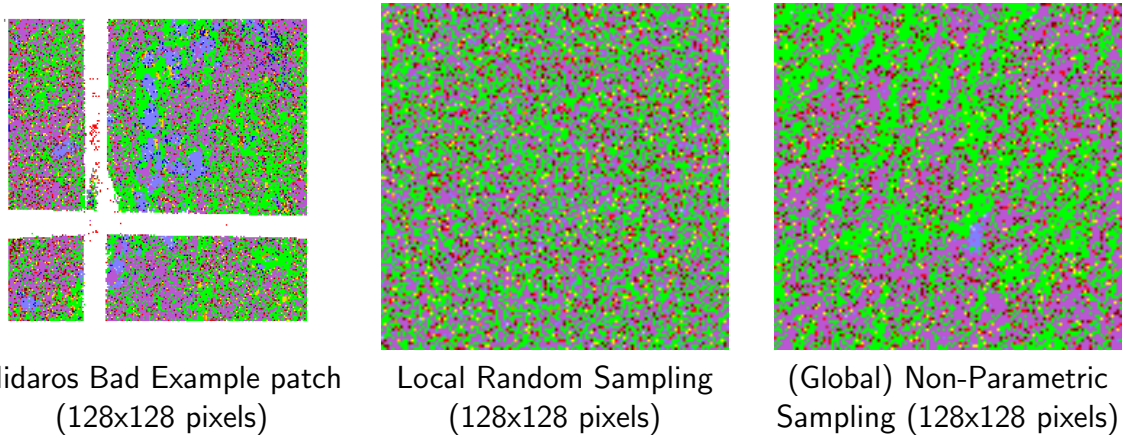


Figure 61: **Left:** Nidaros Bad texture example patch. QEMSCAN of one of one of the stone slabs (Nidaros Bad Small 01). **Middle:** Local random sampling from color distribution. **Right:** Non-parametric sampling results from this patch with a considered neighborhood of $2*d+1 \times 2*d+1$ pixels (here $d=3$).

can observe that the non-parametric sampling results in a visually more convincing texture, but looking at the material distribution (Table 22) one can observe that the non-parametric sampling changes the original material distribution. However, by design the random sampling preserves the material distribution but captures no longer range correlation of the material texture.

Mineral	Original Example	Random sampling	Non-parametric sampling
Pores	2.16%	2.12% ($\pm 0.1\%$)	1.48% ($\pm 0.1\%$)
Chlorite	36.31%	36.21% ($\pm 0.1\%$)	36.81% ($\pm 0.1\%$)
Smectite	1.09%	1.09% ($\pm 0.1\%$)	1.34% ($\pm 0.1\%$)
Biotite	3.17%	3.14% ($\pm 0.1\%$)	3.08% ($\pm 0.1\%$)
Others	1.95%	1.99% ($\pm 0.1\%$)	0.85% ($\pm 0.1\%$)
Dolomite	5.54%	5.56% ($\pm 0.1\%$)	1.21% ($\pm 0.1\%$)
Gypsum/Anhydrite	1.58%	1.57% ($\pm 0.1\%$)	1.06% ($\pm 0.1\%$)
Altered Mafics	40.50%	40.59% ($\pm 0.1\%$)	47.59% ($\pm 0.1\%$)
Calcite	0.29%	0.28% ($\pm 0.1\%$)	0.06% ($\pm 0.1\%$)
Heavy Minerals	4.28%	4.36% ($\pm 0.1\%$)	4.31% ($\pm 0.1\%$)
Siderite	0.37%	0.37% ($\pm 0.1\%$)	0.14% ($\pm 0.1\%$)
Pyrite	0.98%	0.99% ($\pm 0.1\%$)	0.36% ($\pm 0.1\%$)
Quartz	1.78%	1.73% ($\pm 0.1\%$)	1.70% ($\pm 0.1\%$)

Table 22: Distribution of the minerals corresponding to the sampling results shown for the Nidaros Bad stone material in figure 61. The random sampling (middle column) recreates the distribution but the initial statistic changes significantly for the non-parametric sampling approach (last column, $d=3$).

When we apply the non-parametric sampling approach to non regular meshes we obtain results like shown in Figure 62. For these the chemical example patches (QEMSCANs) from figure 61 and figure 63 were used for the sampling.

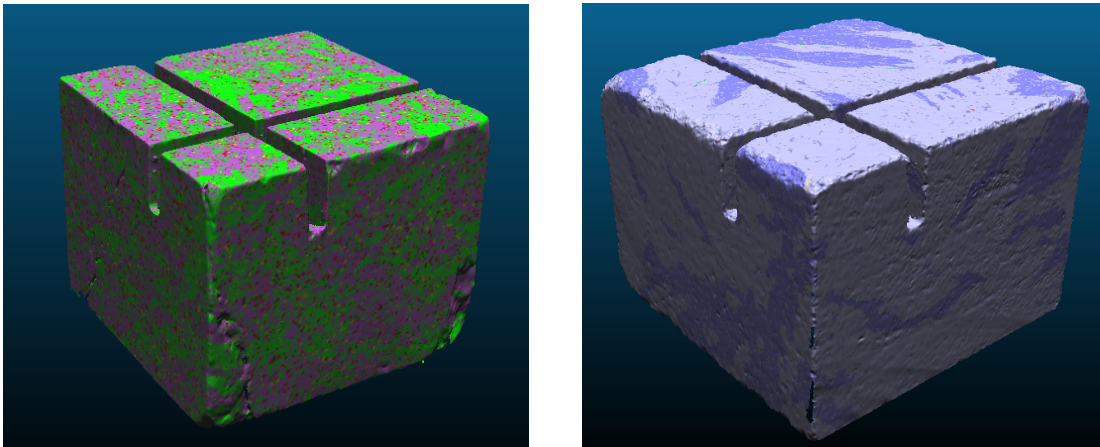


Figure 62: Physico-chemical QEMSCAN stone data from Nidaros (soapstone) and Elefsis (marble) synthetically generated on stone slab geometry meshes.

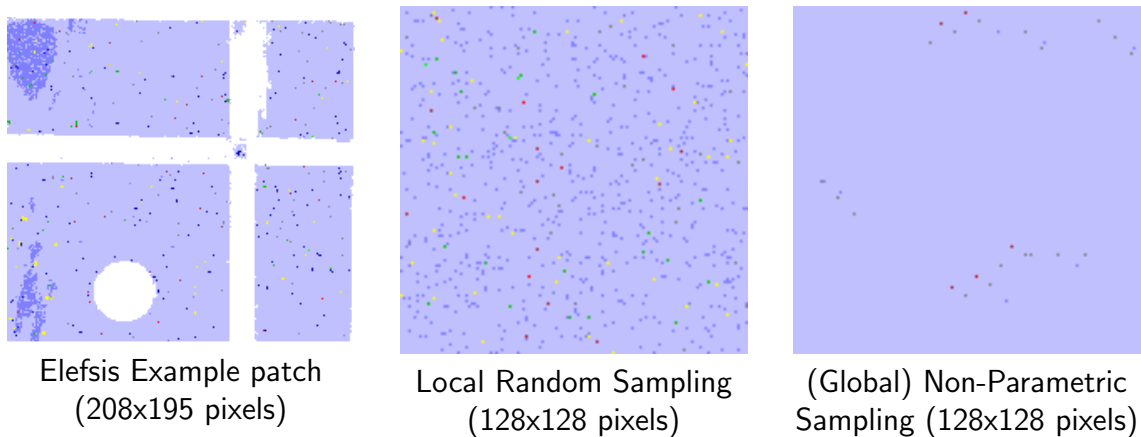


Figure 63: **Left:** Elefsis marble texture example patch (EL1 round 1). **Middle:** Local random sampling from color distribution. **Right:** Non-parametric sampling shows (apart from some random seeds) a uniform color from this patch with a considered neighborhood of $2*d+1 \times 2*d+1$ pixels (here $d=10$).

Local-Global properties

In order to evaluate the observations concerning the texture generation we use natural texture-images to investigate some properties of the local pixel-wise sampling and the global appearance of surfaces that result from the implemented non-parametric sampling approach. We first discuss and illustrate the advantages and disadvantages of the approaches using an arbitrary texture showing a fly agaric mushroom (*Amanita muscaria*).

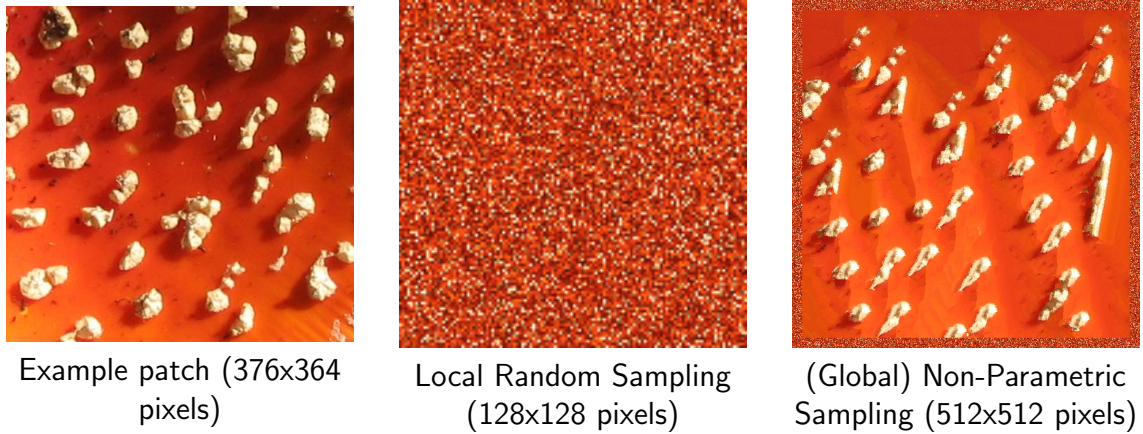


Figure 64: **Left:** Original color-image example patch. **Middle:** Local random sampling from color distribution. **Right:** Non-parametric sampling results from this patch with a considered neighborhood of $2*d+1 \times 2*d+1$ pixels (here $d=15$) that reproduces longer range correlations and lead to a global visual pattern.

Figure 64 shows the results of the two used sampling approaches. The middle image displays the result of a local pixel-wise random sampling and the right image shows the non-parametric sampling results when one considers a neighborhood of $2*d+1 \times 2*d+1$ pixels (here $d=15$). Comparing the rgb-channels of the color distributions one observes that the histogram of the random sampling approach (cf. figure 66) closely reproduces the original distribution (cf. figure 65) but the resulting image has lost all longer range patterns. The statistical distribution of the color values changes when the non-parametric sampling is applied (cf. figure 67), however the longer range patterns are reproduced. Here the neighborhood is chosen to be large enough ($d = 15 \rightarrow 31 \times 31$) to capture the longer range patterns in the original image.

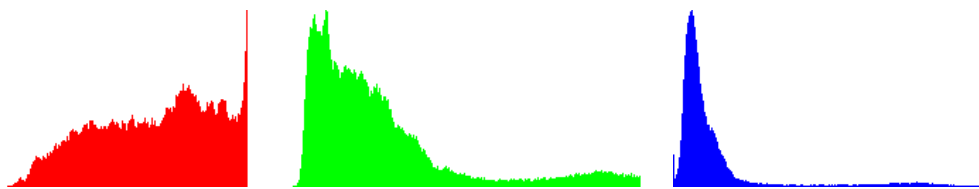


Figure 65: **Left:** Histogram of the rgb-channels of the original example patch.

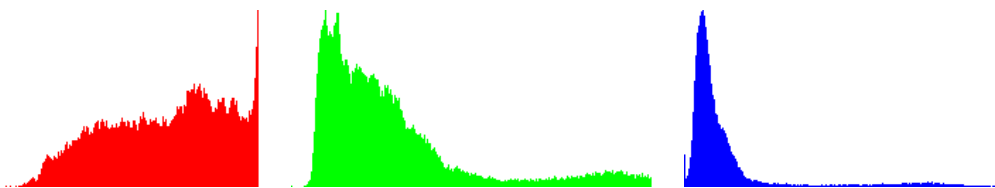


Figure 66: **Left:** Histogram of the rgb-channels of the random sampled image. As the sampling is based on the histogram of the original image the statistical distribution of the color values is preserved.

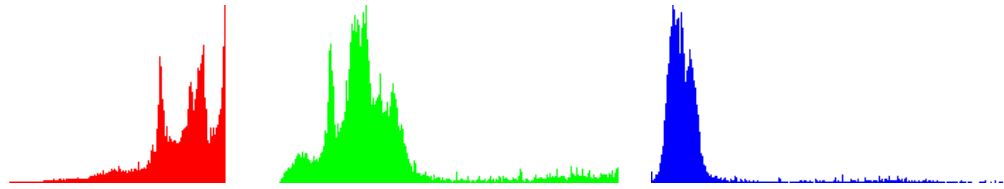


Figure 67: Left: Histogram of the rgb-channels of the image obtained by non-parametric sampling. The sampling influences the statistic distribution of the color values.

In agreement to the discussion above we observe the same behaviour when we apply the sampling methods to other examples. In the images shown in figure 68 and figure 69 we applied the sampling methods to texture images of stones from the Nidaros Cathedral (Respectively the two soapstone types we refer to as Nidaros Bad and Nidaros Good). Using these stone-images for texturing the Armadillo-mesh we obtain results that are shown in figure 70. In order to conclude for a correct distribution of the stone material we suggest to directly use the random sampling and for more illustrative purposes the non-parametric sampling approach result in visually more convincing stone material.

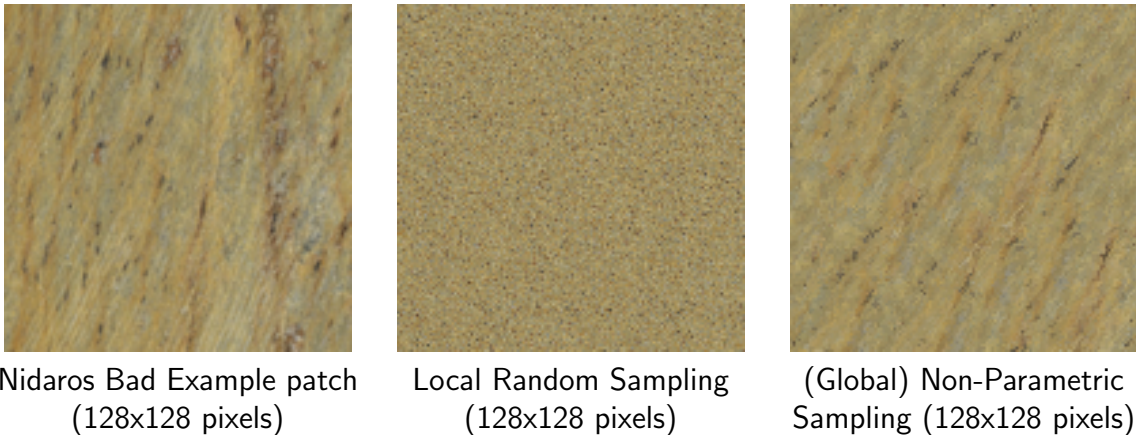


Figure 68: Left: Nidaros Bad texture example patch. **Middle:** Local random sampling from color distribution. **Right:** Non-parametric sampling results from this patch with a considered neighborhood of $2*d+1 \times 2*d+1$ pixels (here $d=10$).

2.5.10 Concluding Remarks

This report describes the evaluation of the implemented prototype software application that simulates surface mesh alterations of Cultural Heritage objects and allows therefore to imitate manifestations of stone degradation phenomena like surface recession. However, a realistic simulation of this type proved to be extremely challenging, both because of the large number of parameters involved and because of the difficulty involved in bench-marking these parameters with actual experimental data values.

Simulating the natural effects that contribute to erosion, which is rather chaotic and also a long term process, we tried to focus on the most important effects and tried to

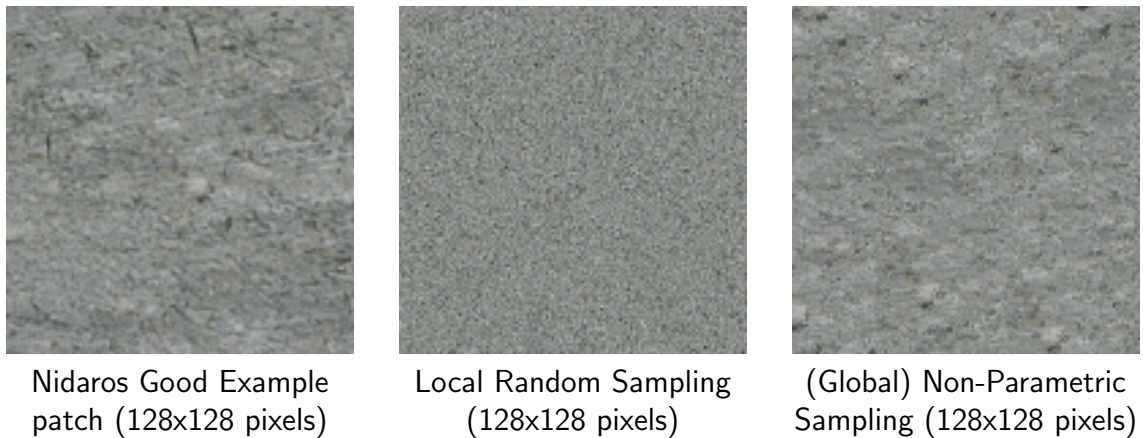


Figure 69: **Left:** Nidaros Good texture example patch. **Middle:** Local random sampling from color distribution. **Right:** Non-parametric sampling results from this patch with a considered neighborhood of $2*d+1 \times 2*d+1$ pixels (here $d=10$).

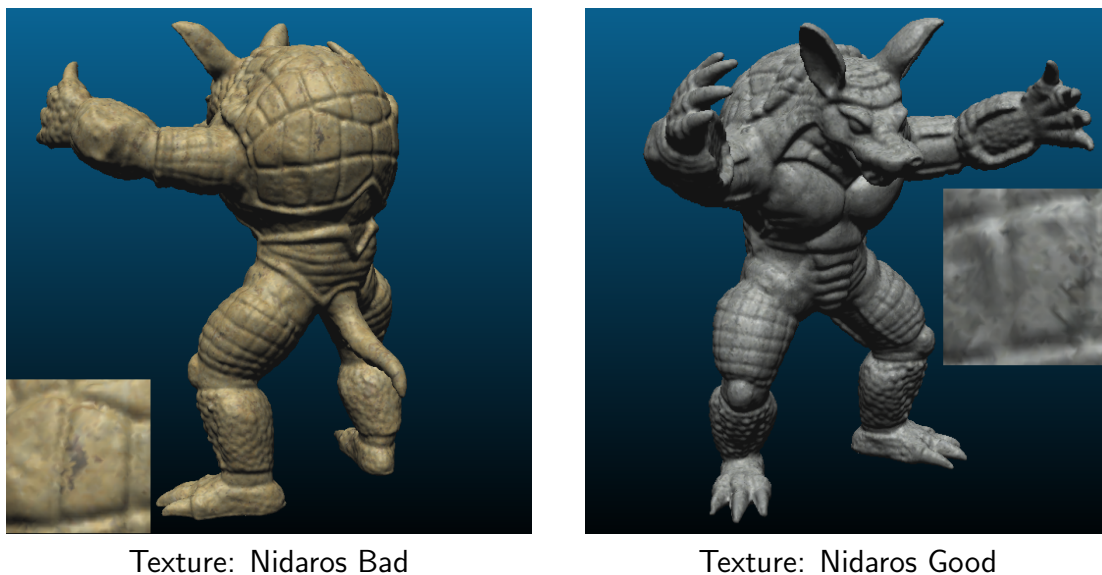


Figure 70: Sampling from a stone texture examples onto the Armadillo mesh along with a closeup view. **Left:** Nidaros Bad Texture **Right:** Nidaros Good Texture

simulate these experimentally in isolation for the specific stone types that were used at the two Cultural Heritage sites we are studying, i.e. Pentelic marble and two types of Grytdal soapstone.

Also, for the purpose of determining in reasonable time the degradation phenomena parameters that drive the erosion simulation, low-cost, small scale, automated erosion chambers for studying accelerated weathering effects on stones were successfully designed, constructed and used. The weathered stone samples were exhaustively characterized by employing a wide range of analytical techniques and approaches that have provided valuable information on the weathering processes and mechanisms.

Although the design of the “Erosion Simulator” application is concluded, there are still some issues that haven’t be addressed. These mostly come from the fact that the interpretation of the results from the accelerated weathering experiments on the marble and soapstone at macroscopic and microscopic levels are in many cases contradicting, and although we can infer that the investigation conducted has given an insight into the changes occurring during erosion/weathering of these stones, the difficulties for incorporating these qualitative results in a quantitative simulation model still remain.

Some of the challenges that we faced and have to be addressed in future work are the following:

- ICP registration is not sufficient. By minimising the overall registration error, it “misses” the possible erosion “common” to all points (compare section 2.4.5). For this reason, it is only possible to measure relative rather than absolute erosion values since there are no external fixed reference points.
- The implemented erosion model in the Erosion Simulator, is based on the erosion model for calcium carbonate stones exposed to acid rain polluted by SO_2 and NO_2 . Approximating the erosion mechanism for other stone types using a similar model was inconclusive, mainly due to the observed swelling of the soapstone.
- Some of the soapstone and marble slabs exhibited an unexpected swelling behaviour in both acid solution chambers; this has not yet been interpreted or modeled.
- The per-mineral recession rates of the stones exposed in the chemical erosion chambers seem quite chaotic and inconclusive. In addition the weak correlation makes it difficult to relate the per-mineral recession rates with the experimental parameters of the erosion chambers.
- The environmental parameters and real exposure times used by the model are partially related to the used solutions’ chemical parameters and the exposure times of the accelerated erosion chambers.

Table 23 summarizes the fulfilled evaluation criteria for WP3, according to the latest [Evaluation Plan \(D5.1\)](#).

2.6 Deviations and Corrections with respect to WP3 Evaluation Plan

The deviation reported in D5.4, which led to the building and operation of Erosion Chambers, was very worthwhile as it gave us large amounts of Erosion data under

controlled conditions. The Erosion experiments were completed in the autumn of 2015.

The deviation arising from the problem of registration and reported in D5.4 was addressed as follows:

- For the archaeological site data, the technique developed in section 2.4.5 of this report, indicated that there was no observable erosion.
- For the stone slabs, a registration correction technique via mass/volume computations (see section 2.3.2) was used.
- Further promising registration techniques, based on modifications of ICP and phase correlation, have also been studied and developed via Master's theses at NTNU. Their development will likely continue beyond the time-frame of PRESIOUS:
 - Vilius Kazakauskas, "Comparison of Large Surfaces from Scanned 3-D Objects", MSc thesis, NTNU, 2014.
 - Martin Stølen, "Out of Core Voxel Data Registration", MSc thesis, NTNU, 2015.
 - Kim Rune Solstad, "Comparing Datasets From Consecutively 3D-Scanned Objects", MSc thesis, NTNU, 2015.

The data from the Erosion Chambers aided our understanding of the erosion process and helped in the parameterization and benchmarking of the Erosion Simulator. We believe that the data is highly valuable for the research community in order to pursue further the study of stone erosion mechanisms and effects.

New deviations:

- Outside stones went missing, due to the lack of a "safety wireframe".
- Chambers permitting SO_2 and NO_2 in gas form were not allowed by the Chemistry Dept. for safety reasons. Using SO_2 and NO_2 dissolved in aqua solutions could not be used for fully evaluating the erosion model.

2.7 Open Problems and Further Work

Many open problems remain in the study and modeling of stone erosion. We summarize some of these below in the form of research questions:

- Is there an appropriate registration method for eroded surfaces that overcomes the drawback of canonical registration methods that minimize the overall registration error, thereby missing the "common" erosion?

- Can one construct a reliable mineral related erosion model for such “complicated” stones as soapstones?
- Soapstone slabs exhibited an unexpected swelling behaviour in acid solution chambers; how can this be interpreted and modeled?
- Can one model erosion due to the freeze-and-thaw with rain effect or the salt effect?

We hope that our erosion chamber data can help us and other researchers to address these issues.

Most of our stones placed in the natural environment went missing, due to weather, animal or human interventions; for future outside erosion experiments additional protection is necessary to keep stones in place.

In the case of the acid chamber experiments, an additional experiment with water only could be performed; this can be used as a reference when identifying the effects purely due to the acids.

	C-WP3-1	C-WP3-2	C-WP3-3	C-WP3-4	C-WP3-5	C-WP3-6	C-WP3-7	C-WP3-8
E-GE1	●		●		●		●	
E-GE2	●		●		●		●	
E-GE3	●		●		●		●	
E-GESC1	●	●	●	●	●	●	●	●
E-GESC2	●	●	●	●	●	●	●	●

● done; ● partially done; ● not done; ● cancelled.

E-GE1: Geometric surface data from Nidaros site

E-GE2: Geometric surface data from Elefsis site

E-GE3: Geometric surface data from the Nidaros and Elefsis stone slabs (soapstone & marble)

E-GESC1: Geometric and physico-chemical data of the Nidaros stone slabs (soapstone)

E-GESC2: Geometric and physico-chemical data of the Elefsis stone slabs (marble)

C-WP3-1: Erosion prediction accuracy against geometric ground-truths

C-WP3-2: Erosion prediction accuracy against physico-chemical ground-truths

C-WP3-3: Erosion prediction geometric robustness (in the presence of noise, holes and spikes, missing data)

C-WP3-4: Erosion prediction physico-chemical robustness (in the presence of noise or missing data)

C-WP3-5: Erosion prediction tolerance against object geometric resolution and scale variations

C-WP3-6: Erosion prediction tolerance against object physico-chemical resolution and scale variations

C-WP3-7: Erosion prediction procedure complexity and absolute processing time evaluation

C-WP3-8: Stone Builder's synthetic stones global and local consistency against real stone materials

Table 23: Updated WP3 Evaluation Table

3 Evaluation of WP4

3.1 Evaluation of Object Reassembly (Task 4.1)

In the first evaluation report we performed a complete assessment of the reassembly methodologies in terms of Effectiveness, Efficiency, Scalability, Discrimination, Robustness, Plausibility and User Input and our experiments were split in four categories. i) Pairwise matching, ii) Reassembly of a single object, iii) Reassembly of mixed objects and iv) Reassembly of heavily damaged fragments. The first category of experiments (pairwise matching) focused on the impact of erosion and demonstrated that the use of a distance metric using ℓ_p -norm can help the robustness of our algorithms (see D5.4, Section 3.1.1). Furthermore we discussed the memory and performance implications from the use of (signed) distance fields as the main data-structure for distance queries. The second category, focused on the assessment of multi-part reassembly. To better evaluate the quality of our results, we performed experiments both with archaeological and non-archaeological models. The latter were also scanned before fracturing in order to have a real reference for comparison. The robustness experiments tested our algorithms with mixed puzzles. In that case, fragments from multiple objects were used and in contrast to the second criterion, the expected result is multiple clusters of reassembled objects and potentially certain isolated fragments. Finally, the fourth set of experiments targeted heavily damaged fragments. Here the main focus was to assess the use of feature curves (f-curves) on the intact regions of fragments. In such scenarios, contact-based approaches fail to solve the problem as the required information is absent from the data, but the combination of contact surface and f-curves can provide a solution to the problem.

The shape-guided approach to the reassembly problem was first conceived and only suggested as a plausible and powerful tool in the PhD dissertation of Georgios Papaioannou back in 2001 (Fig. 71). Now in the PRESIOUS project, in 2015 we have the mature technology to conclude a major part of this ambitious research and have the first results that indicate the practical use of such a methodology. We have shown the great potential of feature curves extracted from the intact regions as a

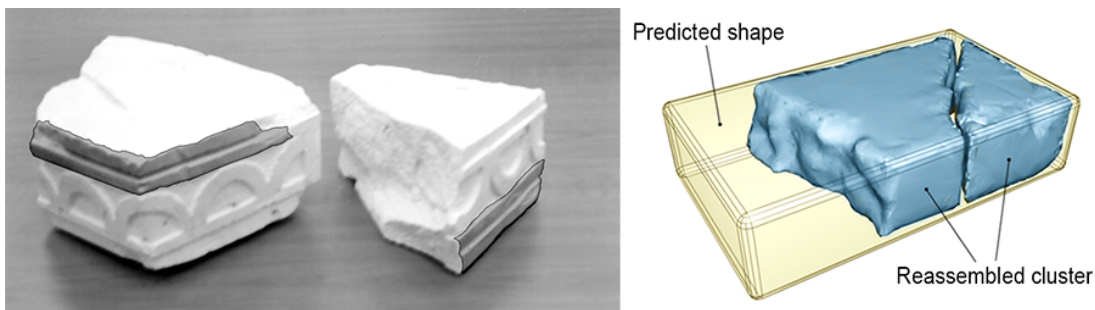


Figure 71: Figures from the PhD thesis of G. Papaioannou, 2001. Shape-guided reassembly was first suggested there as a viable methodology. The research and technology developed in PRESIOUS enabled the implementation of such a methodology in 2015.

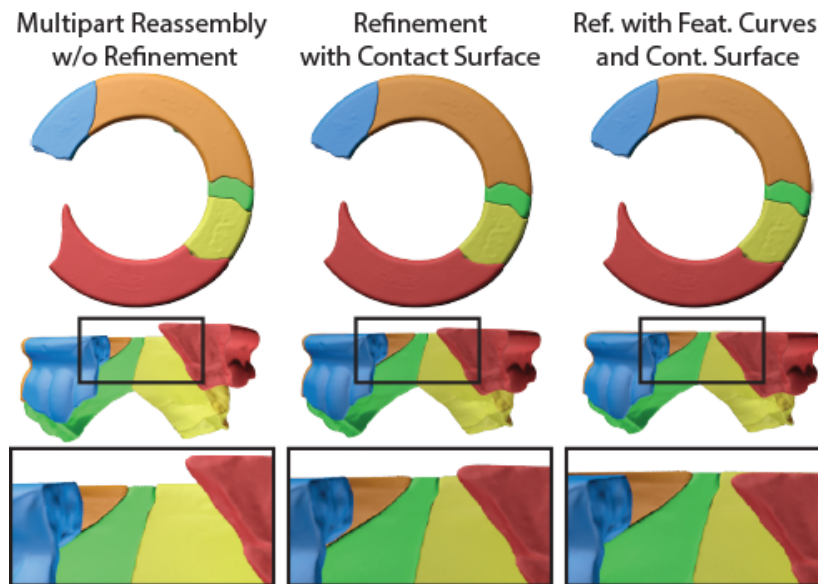


Figure 72: Object reassembly with large missing parts, before iterative refinement (left), using only contact area to refine the solution (middle) and using our combined approach taking advantage of feature curves and contact surface (right). While from the top view all results appear correct the side view shows a skew of the shape that is fixed with our approach. Contact surface refinement completed in 3.5sec. Combined surface and f-curve completed in 4.2sec.

tool for pairwise registration in the first evaluation report. In this second evaluation report, we present our first results on the two open topics regarding reassembly that were discussed in D5.4 Section 3.4 but not covered in the first report. The first one is multi-part registration utilizing both contact surface and feature curves and the second one is symmetry-based reassembly of disconnected fragments. Essentially, these two topics complete the shape-”guided” variant of the reassembly procedure and reflect work that was performed in year 3.

3.1.1 Multi-part reassembly utilizing contact surface and f-curves

Typical multi-part reassembly takes into consideration only the contact surface of the involved fragments. As expected and similar to the pair-wise problem, this approach can fail or even skew an existing good registration in cases where large parts of the reassembly are missing. In our new approach, when refining the placement of a fragment in an existing reassembly, we take into consideration both the matched surface *and the feature curves of the intact surface* of the fragment (See Fig. 72). We should note here that this added complexity on the standard algorithm has only a minor performance impact, as the feature curves points, represent a small fraction of the complete model point-set.

We have investigated cases where this new multi-part registration approach is mostly required and we have invariably confirmed that all assembled clusters that form a linear structure of connected fragments after the spanning tree calculation directly benefit

from it. The longer the formed sequences in terms of the number of participating pieces, the higher the propagated error becomes and therefore the need for additional alignment rules. Fig. 72 demonstrates another characteristic case of alignment error propagation and one that can significantly benefit from the use of f-curves; since the adjoining pieces do not form a closed loop, there is no way to validate and computationally correct the alignment using the surface only bundle adjustment. However, it is immediately apparent that the free ends of the cluster should retain a structural continuity, if extended. Enhancing the bundle adjustment with the f-curves inherently solves this issue as the extrapolated curves of either side register with the curves of the opposite side and become aligned.

3.1.2 Symmetry-based reassembly

The multi-part reassembly step produces objects that are the combination of multiple pairwise alignments, but often, some fragments or clusters of fragments are completely disconnected from the reassembly due to missing parts, bad contact area or the absence of other reliable features to relate and link them to a cluster (such as feature curves). In order to address those cases, we devised a symmetry-based methodology that exploits geometric priors to locate, align and evaluate potential matches of isolated fragments against a set of clustered fragments. The exact methodology is presented in Section 2.9 of the Reassembly and Object Repair Methodology Report (D4.4, public) and first results have been published in [APM15] and presented here.

Computer-generated, “predicted” information of the missing geometry is of little interest to the cultural heritage community in the case where large parts of an artefact are missing and no semantic priors are taken into consideration. But here, we steer the results of symmetry-based completion to a usable direction; using either one of the methods we developed in this project for symmetrical expansion (see below), or even user-supplied planes of symmetry, we generate the reconstructed complete object and use it as a geometric prior (guide shell) to match and align any disconnected fragments. Thus, the symmetrical expansion of the assembly generated so far is never included in the final solution but rather only assists our system in order to suggest potential matches of disjoint fragments, which can be easily inspected by the CH expert.

While symmetry detection is a well-researched area, only a few of the methods focus on objects with large missing data. In PRESIOUS we have developed two distinct approaches that address this problem. First we evaluated the use of the method developed by Sipiran et al. [SGS14b]. This method targeted completion problems (see Object Repair), which inherently include much more information. Although this approach worked for our test cases, it only addresses reflectional symmetry. At the time of our first tests, a second method by [MSAP] was ready, which detects global symmetries using surface registration and can handle smaller partial information as input. In essence the algorithm takes as input the existing geometrical information and using a special form of global registration that avoids overlap, fills the missing

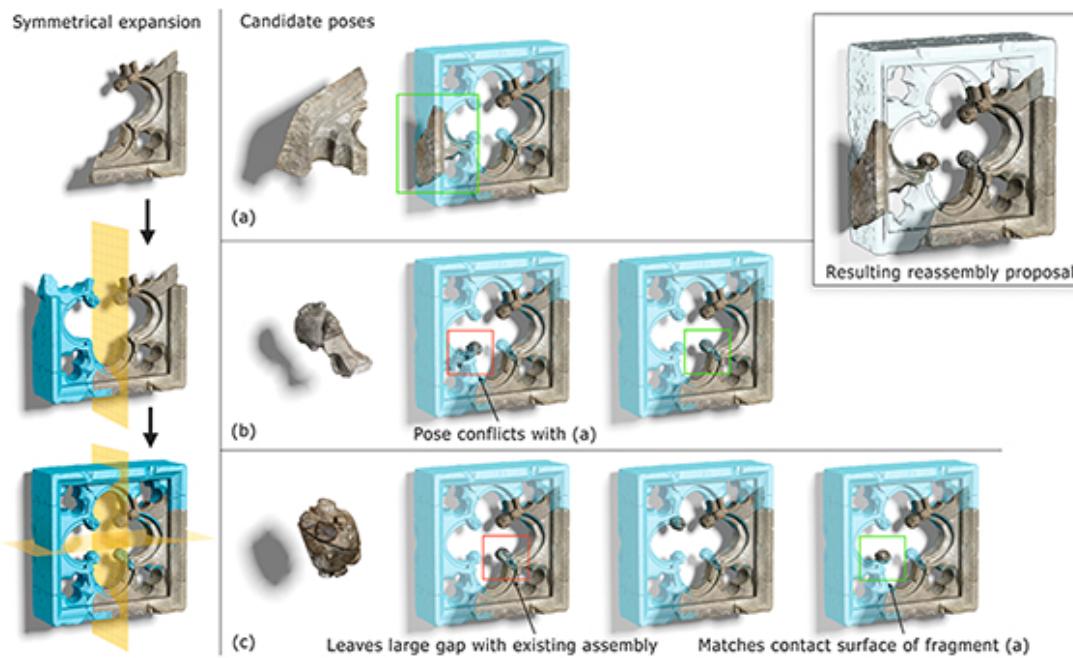


Figure 73: Symmetry-based fragment registration. Left: using the partial reassembly, we extract a symmetrical expansion of the object. Middle and right: Potential candidate poses for the disjoint parts (a),(b) and (c) are generated and filtered by the CH expert, to result in the final reassembly of the object.

information. This method can address rotational, translational and reflectional symmetry. We successfully tested this second algorithm with our partial fragment clusters and came up with similar results.

As explained in the paper, we had to modify an existing global registration algorithm (Super4PCS [MAM14b]) in order to obtain all the possible registration solutions and sort them according to their registration score. We then filter out similar results (based on their transformation matrix) and present to the user the k -best registrations (where k is specified by the user), after refining them using Sparse ICP. From this stage on, there is a selection cycle that heavily involves the CH expert to decide which potential matches make sense, despite the fact that from a computational perspective they are all high-ranking solutions. In the example of Fig. 73, the multi-part reassembly step resulted in one large cluster of fragments, two disconnected fragments and one small cluster of two fragments that was also disconnected from the rest of the reassembly. On the left of the figure, the large cluster is shown, along with evolution of the predicted shape of the entire object. This complementary part is subsequently used, in order to find plausible positions for the disconnected fragments as show in (a) and (b) and (c). In this particular example, part (a) was uniquely matched with significant overlap with the complementary shape only in one position. For part (b), two proposals with significant overlap were generated. The first conflicted with the unique solution for part (a) due to penetration and was rejected. The second placement of part (b) (outlined in green) was also found compatible with the existing geometry of the input reassembly. Finally, for part (c), three positions

were suggested: the first leaves a large gap between its fractured surface and the corresponding fracture on the existing reassembly, while the other two do not cause any problems. However, the third solution is also validated for match with part (a) and is accepted as the prevailing pose.

We should note here that as is, the algorithm operates successfully only on objects with a well-defined generalized symmetry. For *nearly-symmetric* objects, we would need to a) relax the Super4PCS constraints, b) introduce a non-rigid registration step both when generating the symmetrical expansion and at the final piece alignment with the expanded hull. This research however is beyond the timeframe of PRESIOUS but seems a promising direction, albeit a computationally hard one.

This methodology is not part of the VRMW, since it relies heavily on user interaction cycles. In the future we will try to consolidate meaningful rules for automatically discriminating invalid from reliable configurations of isolated fragments to decrease the interaction overhead. We also see a great potential for an Integrated-Action-style project to streamline the whole environment and include such functionality that requires a careful product-level redesign and a strong incorporation of usability testing. This belief is also bolstered by the overall VRMW evaluation as a system, as explained in Section 4.1.

3.2 Evaluation of Object Repair (Task 4.2)

In the first evaluation report we have assessed symmetry-based approaches for object retrieval. In this evaluation report, we planned to evaluate the applicability of partial shape retrieval methods for repair. As laid out in the methodology report, retrieval-based repair aims at 1) retrieving similar shapes from a template (or repair) repository matching partially to an incomplete input object and 2) aligning and merging the shapes.

For the evaluation, we created an encompassing synthetic benchmark data set. While we have used this data already in the first evaluation report to assess symmetry-based repair, we here give more details on the creation of that data, based on [GBS*15]. We then give results on the *success rate* for retrieving complete shapes in response to queries using fragments of these shapes. After that, we list deviations from the planned evaluation work and describe next steps.

3.2.1 Object Fracturing Methodology and Implementation

To generate data that can be used for benchmarking the effectiveness of 3D Retrieval and 3D Restoration methods on fractured CH Objects, we propose a method that produces artificial fragments from arbitrary, watertight input shapes. As discussed in e.g., [CYFW14], simulating physically correct fracturing in high resolution has severe drawbacks. Usually, the simulation is computed on top of a tetrahedral object repre-

sentation using a Finite Element Method (FEM) based approach. A large number of material and environmental parameters have to be provided to the model. This may be a difficult task to do even for experts, when the process needs to be applied to a larger number of shapes of different material, which in turn have been exposed to potentially different environmental conditions. Furthermore, FEM based fracturing simulation is already very expensive to compute for 3D objects with a medium level of detail that is clearly below high quality 3D CH models. According to [CYFW14], a simulation with models of reduced resolution yields significantly different characteristics than a simulation in higher resolutions.

However, for evaluation of retrieval and restoration methods, strictly correct physically fragments may not be needed, and heuristic methods may suffice. Many existing retrieval techniques do not rely on very detailed assumptions concerning the objects material or recurring, small-scale patterns in a shape that reflect certain physical effects under a given range of environmental conditions. In many cases, it can be expected that such techniques will have comparable effectiveness, regardless of the physical correctness as long as the overall characteristics of the shapes are similar enough.

In the field of digital movie production, alternate methods have been proposed to efficiently produce larger numbers of fracturings. While their results are often considered as very plausible by the audience, the methods are not based on sound physical models. We adapt a state of the art method [AMM12] that usually relies on a 3D Modeling artist to provide so-called *cutter objects* and details about their instantiation to control the generation of new fragments. In our case, the cutter object resembles a sphere where small-scale details have been transferred from real digitized breaking edges of a certain material by semi-automatic mesh geometry cloning [TSS*11]. Figure 74 (second from left) illustrates two instances of a cutter object we modeled. Note that when relying on the aforementioned technique, alternative cutter objects based on other examples of real breaking edges can be generated easily. To compute the fracturing, we randomize a number of cutter object instances and their spatial arrangement within configurable boundaries and apply them to a given input object.

Technically, after scale-normalization, the input and the cutter objects are converted to a hierarchical volumetric representation (Level Sets) before we rely on the implementation of the *Level Set Fracture Algorithm* as described in [AMM12]. To obtain disconnected sub-volumes within the Level Set, we generate new breaking edges by computing the intersection of the cutter object surface and the input object volume. The resulting Level Set is converted back to a mesh representation before its disconnected components – the newly obtained fragments of the input mesh – are split into separate manifold meshes. To reflect the fact that very small fragments usually cannot be recovered, or unambiguously associated to specific objects, we heuristically remove fragments that are smaller than a configurable threshold parameter. Next, all vertices of the remaining fragments are annotated according to their Hausdorff distance to the input object.

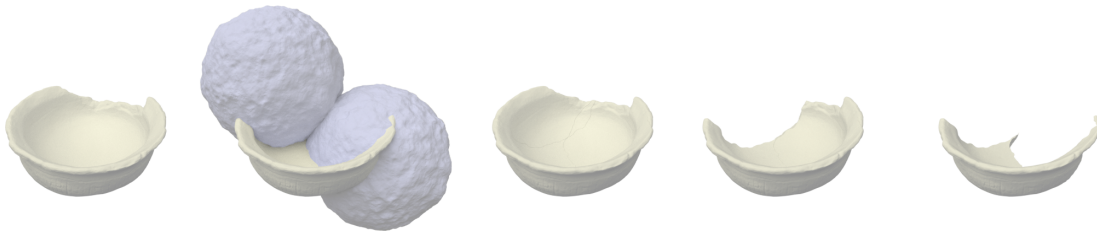


Figure 74: Illustration of our test data generation approach: Starting with an input CH object (left), an exchangeable cutter object is instanced multiple times (second from left). The intersection of the cutter surface and the CH object's volume results in new breaking edges that disconnect the object into fragments (middle). Subsequently, a randomized number of fragments are removed (right). In our approach, the number and position of cutter object instances as well as fragment removal are randomized within adjustable boundaries.

Subsequently, a random subset of larger fragments is removed. This process can be controlled by configurable parameters for the maximum number of removed and the minimal number of retained fragments. During Fragment removal, an optional test can ensure that all remaining fragments share at least a complimentary breaking edge with another remaining fragment, which could e.g., prove useful for the evaluation of retrieval or symmetry-based restoration methods. If the test fails, a different fragment is selected randomly until either the minimum number of fragments to be retained or the maximum number of fragments to be removed is reached. To ensure shared, complementary breaking edges, we a priori construct a connectivity graph based on spatially close vertices, annotated by high Hausdorff distance that belong to different fragments. We test for overall connectivity by counting the respective number of visited fragment nodes during breadth-first search when starting from each of the adjacent fragments. To coarsely approximate deformation of small-scale features (e.g., due to mechanical abrasion, or shot noise), a subsequent optional step can repeatedly introduce Gaussian noise or smoothing. Finally, to synthesize cracks, the remaining fragments can optionally be merged back into a single manifold using Poisson Reconstruction [KBH06]. For testing reassembly methods, this step can be disabled. In both cases, adjacent fragments result in artifacts that are on a visual level very similar to digitization of real cracks (Fig. 75).

The main control flow in our data generation method is implemented in Groovy Script, where individual parameters can be configured. Most individual steps are delegated to various binaries. The Randomized Level Set Fracturing technique is implemented in a C++ based command line application that relies on OpenVDB's Level Set Fracturing algorithm. Several of the remaining mesh processing operations are delegated to Meshlab-Server and Blender. An additional C++ based command line tool may optionally be used to preprocess the fractured and unfractured objects by a sequence of Scale-Normalization, Poisson Reconstruction and Uniform Remeshing. The generated benchmark data is provided under <http://fracture-benchmark.dbvis.de>.



Figure 75: Comparison of real and synthetically generated defects within an object: A part was missing already in the input object (right). Our approach removed an additional part (center front). Also note original cracks (back right, front left) and synthetic cracks (back left, right) next to each other. Our method allows creating rich fragment test cases for retrieval and restoration applications from existing 3D CH Models.

3.2.2 Fragment Benchmark Based on Hampson Collection

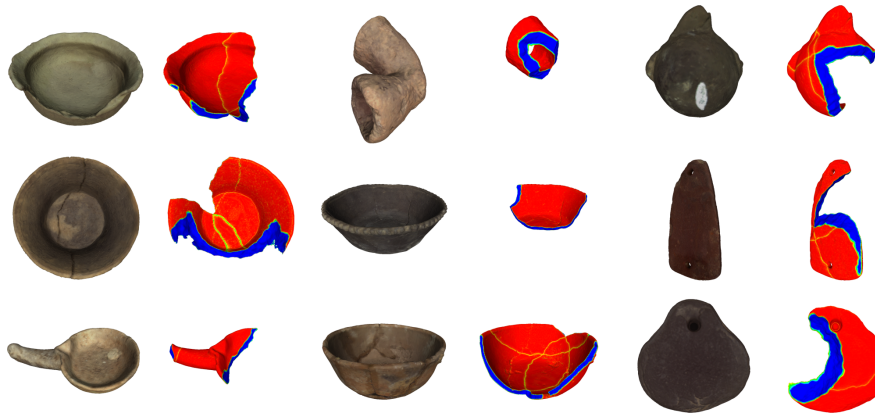


Figure 76: Original, digitized CH Objects from the Hampson Museum Dataset along with their artificially degraded counterparts. Fragment vertices are colored by Hausdorff distance to the input models. Note that only some of generated fragments have been randomly omitted whereas others are still included and cause cracks in the generated models (colored green to yellow, medium distance). Synthesized breaking edges are colored in blue (high distance).

To generate benchmark data based on our above describe methodology, we selected the freely available Hampson Museum Dataset provided by the University of Arkansas. The collection contains an encompassing set of American Indian clay pottery. The collection currently contains 445 objects, however not all of them are watertight and contain interior object geometry. Hence we manually selected a subset of 84 watertight models from this collection. We applied our fracturing approach as described above to create our *Hampson Fracture* data set. Specifically, we fixed the number of cutter objects to four instances. To exclude too small resulting fragments, we heuristically discarded fragments which contained less than one thousand vertices. From the resulting fragment set, we randomly omitted at most three fragments and retained at least one. No smoothing or Gaussian noise was applied, before the remaining fragments were merged by Poisson reconstruction. Figure 76 provides a

comparison of textured original models and the results of our data generation. In our benchmark, the fragment set represents the restoration/retrieval problem, while the underlying full object represents the ground truth.

3.3 Evaluation of Partial Shape Retrieval

We evaluate the performance of partial shape retrieval. The goal is to retrieve the correct unfractured counterpart for each synthetically fractured model (see Section 3.2.2). While this task can be considered roughly similar to partial retrieval, fractured queries do not contain holes and gaps but additional breaking edges where larger parts are missing. Using the generated data in this way, the obtained measures provide an indication of the invariance of a retrieval technique against defects encountered in fractured CH Objects.

We proposed partial retrieval based on Heat Diffusion features (see D4.4 Reassembly and object repair methodology report). Specifically, we explored application of Heat Kernel Signatures (HKS) [SOG09] and Scale Invariant HKS [BK10], both in combination with a soft-quantized Bag of Features with dictionary size of 256, trained on the unfractured objects. As a baseline technique, we included the DSR descriptor [Vra05], which is a global shape descriptor.

As distance function to retrieve the input models we use L_p norms where $p \in \{0.1, 0.3, 0.6, 0.9, 1, 2\}$ as well as statistical distance measures including χ^2 and Kullback-Leibler, Jeffrey and Jensen-Shannon Divergence.

We measure the *success rate* as the fraction of fractured objects, for which the correct unfractured object is ranked within the first n results, where $n \in \{1, 5, 10, 25\}$. While we have to note that the used approaches are not in particular designed for partial retrieval, we can observe interesting results (Fig. 77). Given existing experiments for global retrieval on these methods, it was not to be expected, that DSR outperforms HKS, which in turn is not clearly outperformed by SIHKS. Furthermore, it is interesting to see that for our fractured objects, the DSR descriptor is very sensitive to the choice of distance function. This contrasts our results of the same descriptors and distance functions when measuring R-Precision with other benchmarks, such as the well-known Princeton Shape Benchmark [SMKF04].

We note that this counter-intuitive result may be given due to our current implementation of the HKS and SIHKS descriptors. A refinement of our HKS-based retrieval workflow is in progress and we intent to publish the respective results in the future (see also Section 3.3.1).

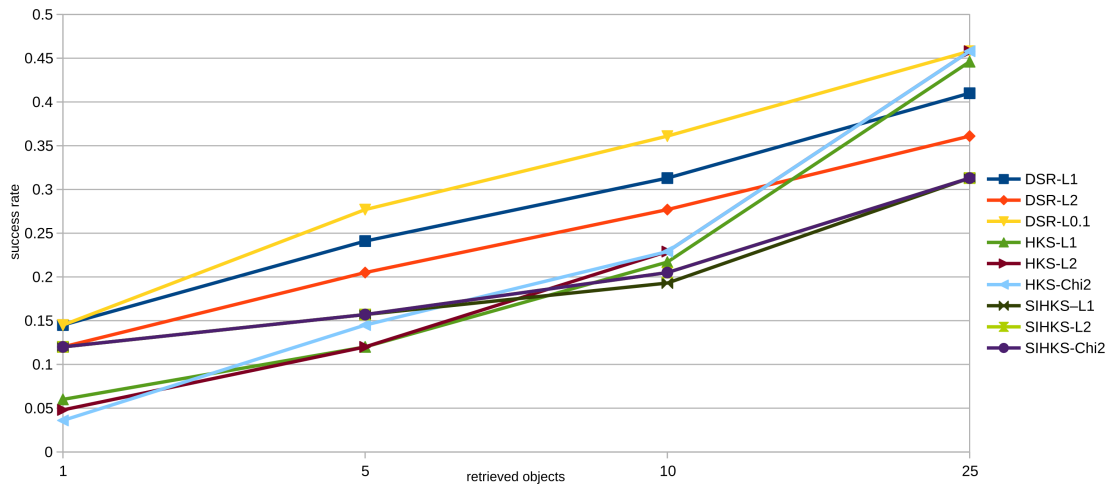


Figure 77: Fraction of successfully retrieved unfractured objects. We show the results for L_1 and L_2 and the respective best performing other distance measure tested.

3.3.1 Deviations and corrections with respect to WP4 task 4.2 evaluation plan

In the first evaluation report, we presented encompassing results on the symmetry-based approaches for shape completion. For the second evaluation report, we planned to evaluate retrieval-based approaches for shape repair. While extensive experiments were planned, due to a number of technical setbacks we could only perform a limited number of experiments as described above. Specifically, our HKS feature extraction pipeline performed slower than expected, and producing problems for feature extraction for many of the artificially created fractured objects. While we recently could speed up the feature extraction phase, in sum this led to a much smaller number of experiments we could perform. According to our current findings, have indication that Heat Diffusion approaches are suitable for partial retrieval in the setting of PRESIOUS. Future work needs to experimentally substantiate this approach.

4 Evaluation of WP5

4.1 Reassembly Pipeline Evaluation

We have evaluated the VRMW platform both internally, in order to detect bottlenecks and decide on the easiest ways to simplify the algorithms' parameterization, and with the help of a cultural heritage expert. Since the Reassembly-side of the VRMW will be made public via the web site of the AUEB Graphics Group and linked via the PRESIOUS project web site, a wider and open evaluation of the system will be sought after the final version release on M36.

Most of the internal testing was performed in the late part of Year 2 and is included in the first evaluation report. New functionality that was not tested in that report and is now part of the VRMW includes the use of feature curves, which is a totally transparent process for the VRMW-side of interaction, full-featured collection management, storage and export and the incorporation of manual constraints in the form of "links" for white- and black-listing certain fragment combinations. As the latter is a typical point-and-click interaction, we shall not discuss it here.

Since it is important for us to measure the impact of such a tool to the CH community and eventually streamline its functionality to end up with a practical and exploitable application, we have already demonstrated VRMW to an archaeologist collaborating with ATHENA-RC (not affiliated to the project, though) and gathered her feedback on the tools provided, the interface and output. The archaeologist saw the VRMW platform for the first time, so we were able to get a obtain a true (although limited) first impression of a user's reaction. This information had led to a final development cycle of the prototype with a few improvements that are presented below. We intent to pursue any opportunities for funding a production-grade system, taking into account collaboration functionality, potential linking to existing object databases etc, user profiles etc. To this end, we believe the feedback from the public release and dissemination of the current version of software is invaluable.

4.1.1 CH Expert's Feedback

Importance and Impact. As a tool it was greeted with enthusiasm, mainly because it provides a quick way to assess solutions but most importantly because it enables the extraction of information that is meaningful to the CH researcher and can provide metrics for backing up and documenting assemblies and interpretations of objects.

Interface. The first aspect of VRMW that drew the attention was the visualization of the fragments, which was deemed rich, realistic and easy to understand and work with. On the downside, the multitude of available options (for the technical demonstration) were daunting to an untrained CH expert and best be simplified or avoided in future release. The CH expert commented that from the CH perspective it might be better

if the procedures available were linearly laid out, thus enforcing a pipeline of steps, even knowing that this way access to a wider selection of tools at any time would be sacrificed. We believe that for a future production-grade reassembly system we should work in very close collaboration with CH experts and from a zero basis in order to rethink the interactivity in more simplified and streamlined manner.

Results and Reporting. The accuracy and exploitation of both contact surface and shape priors were welcomed. It was confirmed that caching of results does make sense for large collections and that the use of salient feature curves also is a reliable element for comparing fragments in many cases. In VRMW version that was demonstrated, reporting was limited to a textual listing of the fragment IDs and their combinations in the clusters along with the respective matching error. We learned that from the CH expert's point of view this information is not very helpful in documenting an assembled object, since more real-world measurements and facts are required to back up an interpretation, such as distance measurements, continuity metrics etc. Additionally, the association of clustered fragments with the respective pairwise measurements should be clear and easy to spot in a generated report. This led us redesign the report output functionality of a reassembly summary, as explained in the next section.

Measurements. Again, the CH expert explained that the relationship between two fragments should be expressed in a form that is more meaningful to a CH researcher, as the demonstrated VRMW version reported matching scores. On the other hand the distance tape tool that measures distances between arbitrary points on fragments was very intuitive and easy to use and a welcome complement as a research tool (Fig. 78). We changed the fragment-to-fragment compatibility measurement to an average distance between fragments as explained below.

4.1.2 VRMW Reassembly Improvements

Taking into consideration the feedback from the CH expert, we proceeded to modify a) the pairwise compatibility measure reported, b) the reporting format and information shown.

Pairwise Compatibility. For a given pair of fragments we report the **average distance** of their area of overlap, implemented as the Hausdorff distance between points, after filtering out distances longer than a predetermined threshold. The threshold corresponds to a distance beyond which we do not consider the surfaces to be in contact. Typically this is set to 0.5cm for the medium-sized objects in our experiments (fragments up to 80cm long). In essence, the filtered sets of corresponding points also help us measure the **contact area** of the fragments (if any). For the calculation of the average distance, we always use the current pose of the fragments and not the one that has been calculated by the reassembler, as the user may have tweaked the position after acquiring the reassembly result. This way, the reported measurements always reflect the current state of the experiment.

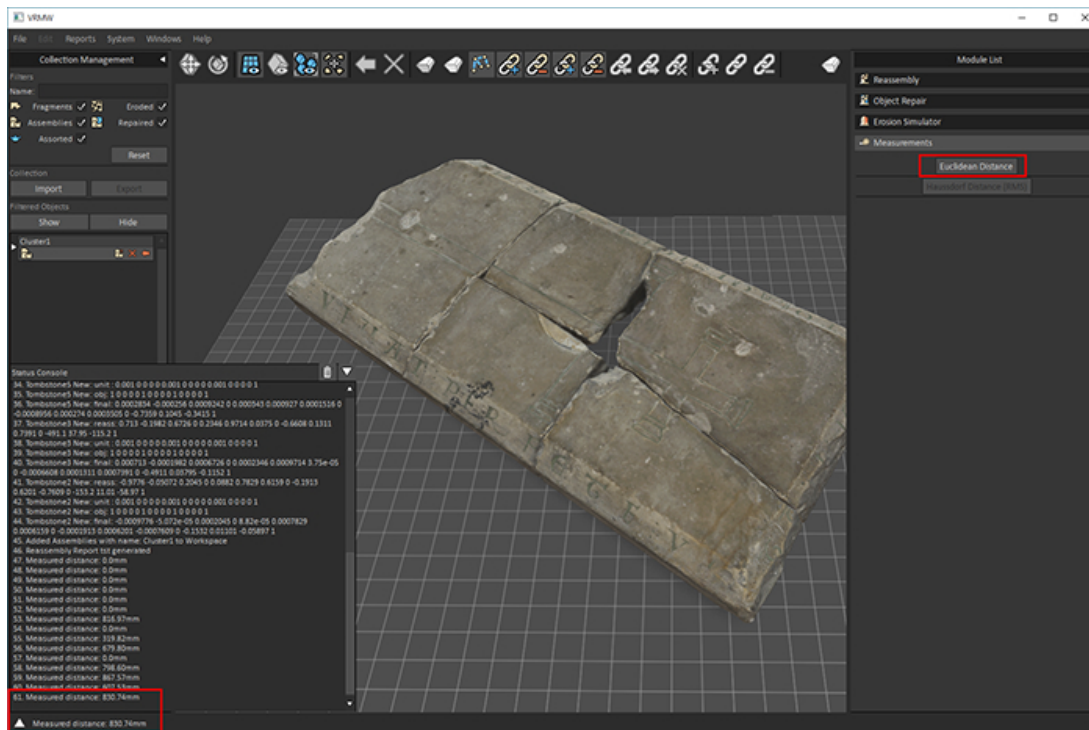


Figure 78: Measurements pane in the VRMW interface and results from the tape tool.

Reporting. In order to immediately associate results with the shape of the fragments involved, we have redesigned the report to include an annotated copy of the current view of the workspace. The new report, which is exported in HTML format (see Fig. 79), includes meaningful information for the pairs in the reassembly, such as average and median distance between fragments and their contact area. Using HTML as the output format makes it very easy to process, distribute and print the report from any browser.

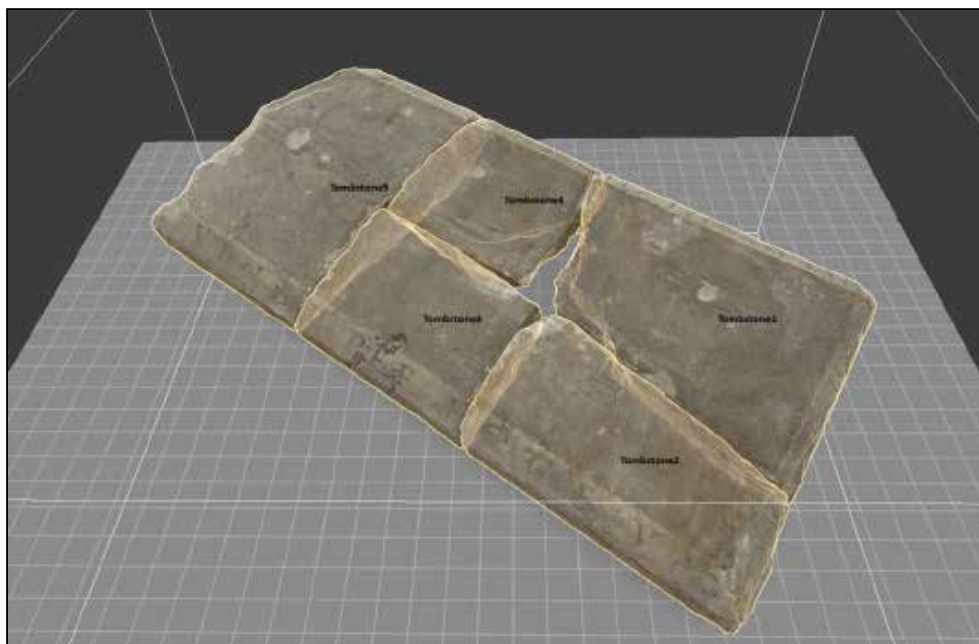
4.1.3 Evaluation of the Feature Curve Extraction Process

We have implemented a separate tool for pre-processing fragments and extracting the feature curves, which are then stored and later used at any time by the reassembler if detected along the fragment file. For the curve extraction we employed two different strategies, one semi-automatic and one user-assisted. We describe them in a nutshell in Section 2.4.2 of the Reassembly and Object Repair Methodology Report (D4.4) and discuss below why we selected the user-assisted approach to be used in the feature-curve-based alignment [APM15].

The semi-automatic method uses the *Mean Curvature H* at each vertex point at multiple scales via the sphere volume integral invariant (we omit the technical discussion here). The sphere volume integral is estimated in our experiments at 1% through 6% of the object's diagonal and we keep the median value for each point. We mark as feature the points the k_1 percentage of the extreme values of the entire

Reassembly Summary

Date: 10/2/2016 1:58 ii



Tombstone1 - Tombstone4

Average distance: 3.34mm
 Median distance: 2.66mm
 Matching area: 9704.48mm²

Tombstone1 - Tombstone5

Average distance: 3.34mm
 Median distance: 2.74mm
 Matching area: 38608.36mm²

Tombstone1 - Tombstone3

Average distance: 3.29mm
 Median distance: 2.63mm
 Matching area: 48769.82mm²

Tombstone1 - Tombstone2

Average distance: 3.17mm

Figure 79: Example of a reassembly summary report (1st page).

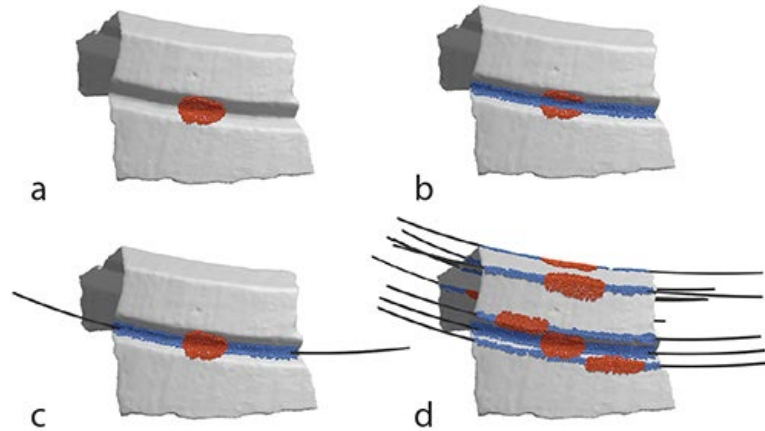


Figure 80: a) User selects a set of points, b) Extraction of feature points, c) Extrapolated points using the Quadratic B-Spline approximation of the feature, d) Extracted feature point sets and extrapolations. The model is comprised of 50K faces and the processing time required for the generation of the feature curves, given the user selection, requires 1.4 sec.

set of points. The resulting point set is subsequently split into feature point groups, in a greedy manner, by picking a random point and assigning neighboring points with similar descriptor values to the same cluster. Due to the presence of noise (or erosion in our cases) continuous features may be interrupted. In order to address this issue, we allow certain points (of lower descriptor values) in between interrupted clusters to be included for bridging gaps.

Common to both the semi-automatic and the user-guided approach, since we are only interested in features that span across multiple fragments, we keep features with at least one end near a fractured facet and discard the rest. Having extracted the feature point groups, we trace their trajectory using a parametric curve. Due to the underlying fluctuations of the surface, the generated point set can be noisy or sometimes incomplete. So we utilize a skeleton extraction method that results in points that can be easily approximated by uniform curves using least-squares fitting.

The feature selection process described above involves several assumptions about the qualitative characteristics of the erosion, the presence of ornate features or the expected smoothness of the geometry. More so, it considers that fragments have been segmented relatively accurately so that external surfaces are properly separated. Therefore despite the fact that the described methodology is robust enough, once the proper thresholds have been set, it is still required by the user to modify specific parameters in order to achieve the desired result.

On the other hand, by introducing a simple user-guided process, we actually sped up the overall process, while extracting all the desired features. The user selects a small portion of the fragment with a brush tool, which roughly includes the desired feature. Initially, using the median H of multiple scales for each point, we detect the

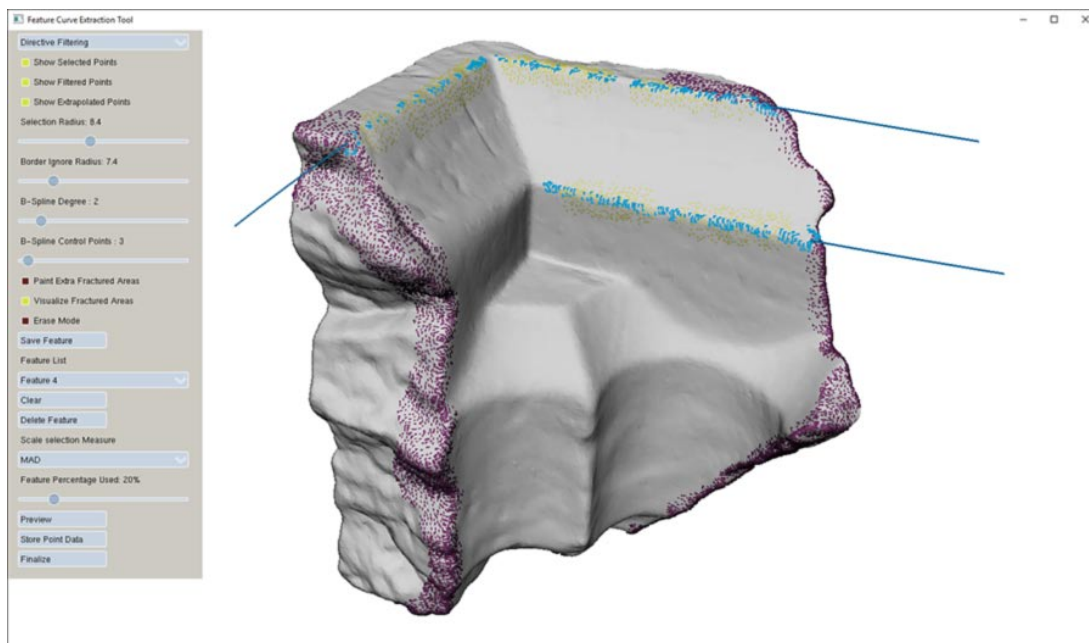


Figure 81: Feature curve extraction from an unsegmented mesh. In order to impose a stopping criterion on the salient point region expansion, the user can paint-select fracture points directly on the mesh (magenta points). In the example, feature curve extraction tool was run for fragment DoraEmbrasure3 (medium resolution) with parameters `-xL_dist 12 -fp_glimit 10`.

extrema over the selected area and subsequently extract the feature points. Using again a skeletonization on the feature points, we filter them and obtain the actual B-spline curve that locally describes the intended structure. Using extrapolation, we search for points with similar descriptor values that are close to the extension of the curve. The newly discovered points are added to the feature point group and the feature curve is re-evaluated. The process is repeated until no more points can join the feature set. The resulting feature curve is presented to the user, along with its extrapolated parts that will be used in the matching step (Fig. 80).

This user-guided process proved robust and enabled us to successfully extract features even when the separation and classification of regions as intact or fractured were not perfect and an automated process would probably fail. This is a valuable property, especially in the case of eroded fragments, where the boundaries between fractured and intact regions are often unclear.

The feature curve extraction tool can also work as a stand-alone tool for unsegmented meshes, although this is not recommended, since it imposes some extra manual work and has a probability of erroneously selecting points on fractured areas and thus requires more careful parameterization. In particular, in order to compensate for the lack of a segmentation, the user must select points neighbouring possible salient feature regions on broken areas in order to avoid including sharp features from these regions in the salient feature point set. This is done by painting these extra points at

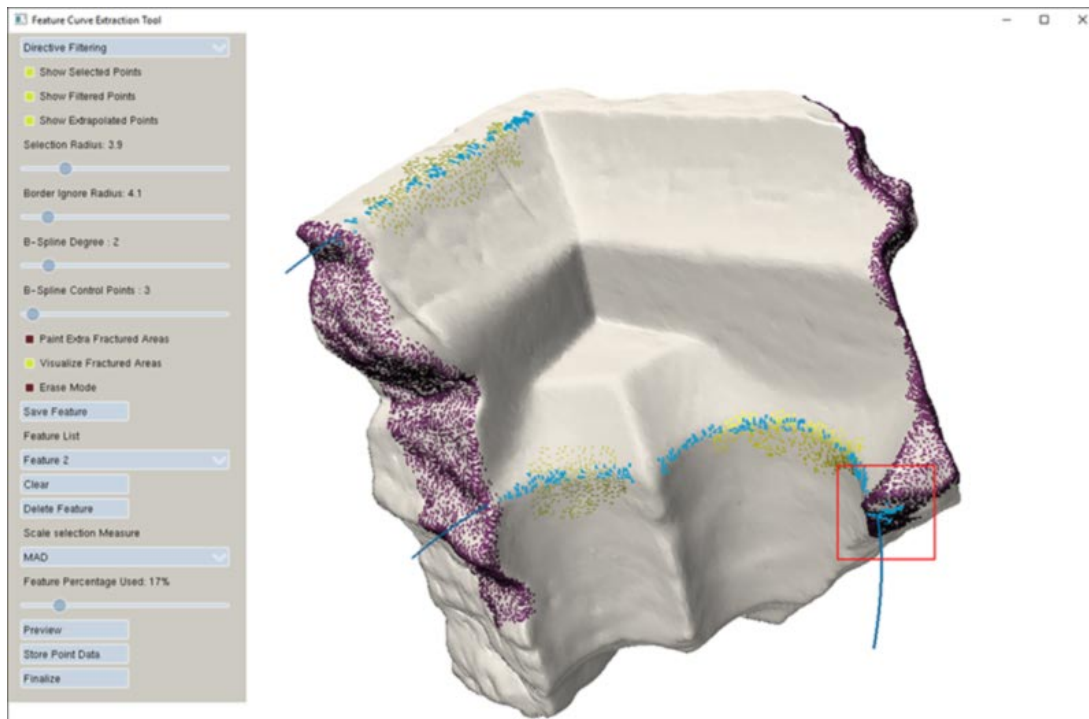


Figure 82: Feature curve extraction from an unsegmented mesh. In this example, since no true fractured/intact boundaries have been established, salient point regions may evolve in undesired regions that will skew the resulting curves (see highlighted area) and require more careful manual exclusion of points.

any time during the process, by toggling "Paint Extra Fractured Areas" (see Fig. 81). In contrast to the extraction of feature curves from previously segmented fragments, using raw meshes makes it much harder to discriminate salient points even, when manually excluding some of them and therefore the latter is not recommended as a standard procedure (see Fig. 82).

The user interface of the feature curve extraction tool itself is very responsive, with very fast feedback on all operations. Painting and selections instantly update the results in the 3D view and the only operation that may take more than one second for certain parameters is the result "Preview".

This section focuses on the evaluation of the complete pipeline of the predictive digitization methodology.

4.2 Evaluation of the complete WP2 pipeline

In this section we evaluate the complete predictive scanning pipeline in terms of accuracy, reliability and efficiency.

4.2.1 Overall accuracy of predictive scanning tool

To measure the accuracy of the predictive scanning process we compare the predicted 3D object with the 3D object that is acquired using conventional 3D scanning. We consider the second model as the *ground truth*, although it is worth noting that the digital acquisition process introduces a series of measurement and alignment errors. For the purposes of our experiments, we can consider that these errors are relatively small compared to the *prediction error*, which we want to measure.

Error Metrics

To measure the distance (d) between the predicted (P) and the ground truth (G) models, we compute the maximum RMS point-to-point distance in Euclidean space. In particular,

$$d = \max(d(P, G), d(G, P)),$$

where

$$d(A, B) = \sqrt{\sum_{x_i \in A, y_i \in B} \|x_i - y_i\|_2^2},$$

where y_i is the closest point to x_i .

Heatmap Visualization

To facilitate the visual inspection against the ground truth, we provide heatmap images that encode for every point in the predicted object the nearest distance to the ground truth object. Blue colours indicate a zero distance and red colors indicate the maximum distance between the prediction and the ground truth (this means that the colour-encoded distances are normalized).

Measurements

Figures 83, 84, 85 and 86 demonstrate the accuracy of our predictive scanning system when working on a pottery dataset. The input partial scans were obtained with Breuckmann Optoscan scanner and represent roughly 33% of the desired object. Figures 87, 88, 89 and 90 provide similar information for input partial scans obtained with Microsoft Kinect V2 for Windows sensor.

Discussion

The RMSE in all examples has been kept to reasonably low levels. It is worth noting that this is not a zero-residual problem, since the partial scan is not a perfect subset of the ground truth object, due to the sampling and alignment errors of the digitisation process. As expected, predictive scanning is more accurate for high-quality input partial scans. Still, predictive scanning is relatively robust to low-quality input partial scans, with a mean RMSE in the same order of magnitude.

Furthermore, visual inspection of the results indicates that the quality of the predicted objects is acceptable, without any major artefacts or distortions.

	retrieval	k-sparse	relaxation	poisson	registration	blending
HM124	11	10	5	14	21	4
HM189	11	9	2	14	18	4
HM333	9	8	3	17	15	4
HM465	9	11	2	18	27	5

Table 24: Time expenses in seconds for each component of the predictive scanning pipeline for different input scans. The total execution time for the complete pipeline is slightly higher than the sum times in each column due to some additional disk I/O time and visualization overhead, which is not included in the measurements. Registration numbers include both rigid and non-rigid alignment. The Poisson reconstruction is performed in MeshLab server.

4.2.2 Efficiency of predictive digitization platform

Table 24 shows the runtime in seconds for each component of the predictive scanning process. Considering that the conventional high-resolution scanning procedure requires about 20 minutes for each object, the proposed pipeline significantly reduces the overall digital acquisition time. This makes our predictive scanning procedure especially appealing for large-scale digitisation projects.

4.2.3 Discussion by archaeologist

The technologies developed within WP2 could contribute and be useful tools in facilitating archaeological and/or museum work in various stages of the cycle of the cultural object, that starts with its discovery (excavation) and ends with its presentation and communication to the scientific community and the public (publication, exhibition).

In particular, as regards to the PDP, both partial retrieval and model reshaping can contribute to the archaeological and museological procedure. Beginning with the excavation, the PDP could be used as a tool in order to be decided how to continue the research in a particular area, since it can provide to the excavator a tentative shape of the partially unearthed object.

PDP also enables the full presentation of the object through the created 3D model and that way it would contribute to two stages: a) study and b) presentation. This is important if we consider that access to the objects is often an issue. This is either because they can be in storerooms with limited access or located in places where the objects are not entirely visible. The latter is often the case with the objects exhibited in Museum Galleries.

Retrieval of pottery models as a standalone tool could also be useful for the identification and categorization of the object, and in this particular case of a vase. That way the study (a significant next stage to the cycle of the object) of the vase would be facilitated, while at the same time model reshaping could help in a better understanding.

The developed 3D model would be a suggestion for the scholar (archaeologist, art historian, museum curator etc) to accept or reject a tentative categorization of the object (e.g. shape, type) and at the same time to facilitate its presentation to the scientific community and the general public.

The evaluation of the PDP, through its use from the archaeological point of view shows that it can be used in order to make easier our work, since: (i) the search resulted in accurate predicted models in most of the cases-some of them were sufficiently accurate to be presented, while there were others sufficient enough for presentation and for study purposes, (ii) in cases of known ground truth, the predicted object is similar to the shape of the actual object, (iii) the time required by the overall pipeline is significantly reduced, when comparing to the time required for the manual scanning process of the complete object, (iv) the graphical user interface is realistic and easy to understand and work with.

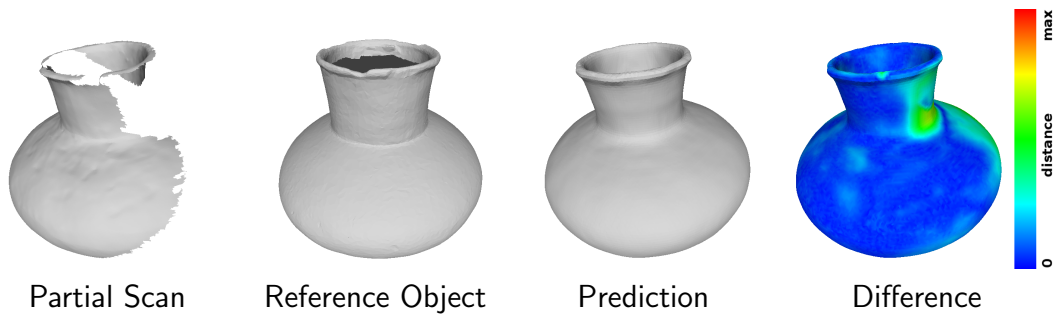


Figure 83: Predictive scanning results on the HM591 object, obtained with Breuckmann Optoscan scanner. $RMSE = 2.40mm$.

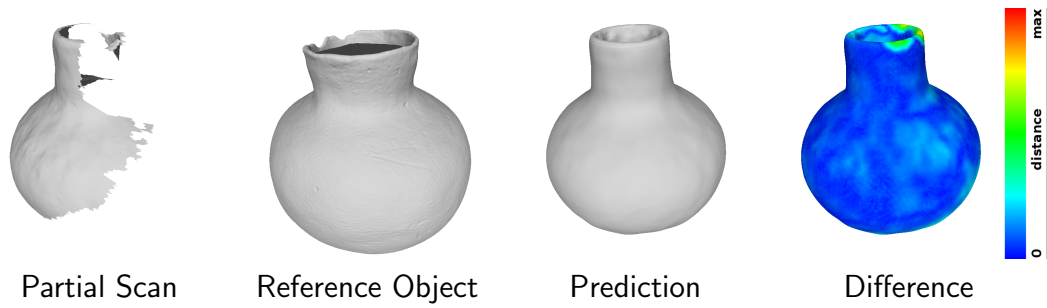


Figure 84: Predictive scanning results on the HM536 object, obtained with Breuckmann Optoscan scanner. $RMSE = 2.43mm$.

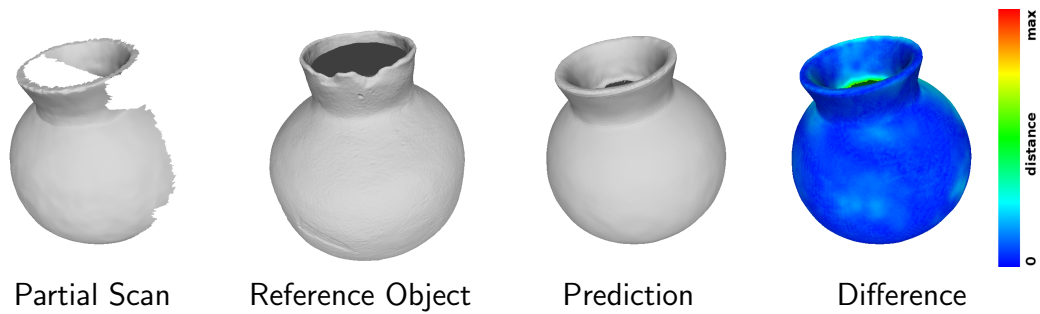


Figure 85: Predictive scanning results on the HM465 object, obtained with Breuckmann Optoscan scanner. $RMSE = 2.56mm$.

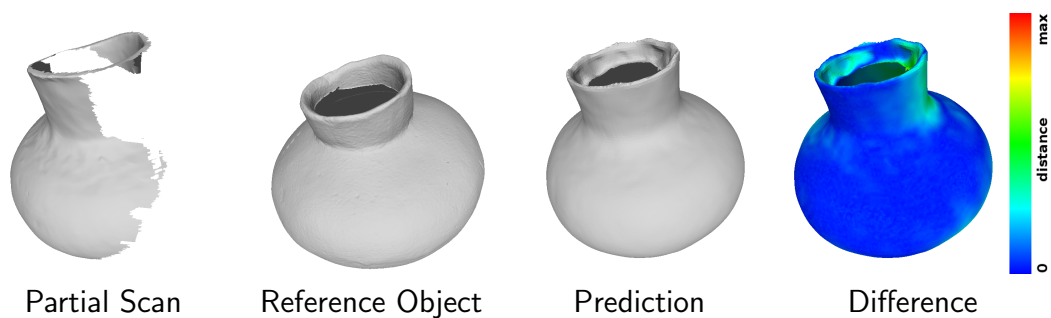


Figure 86: Predictive scanning results on the HM124 object, obtained with Breuckmann Optoscan scanner. $RMSE = 4.98mm$.

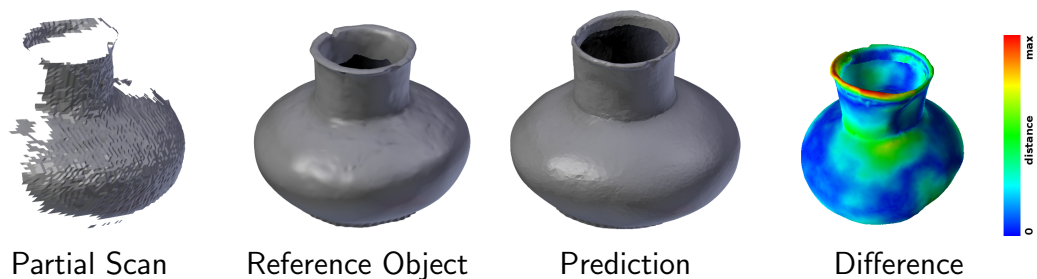


Figure 87: Predictive scanning results on the HM591 object, obtained with Microsoft Kinect V2 for Windows sensor. $RMSE = 2.69mm$.

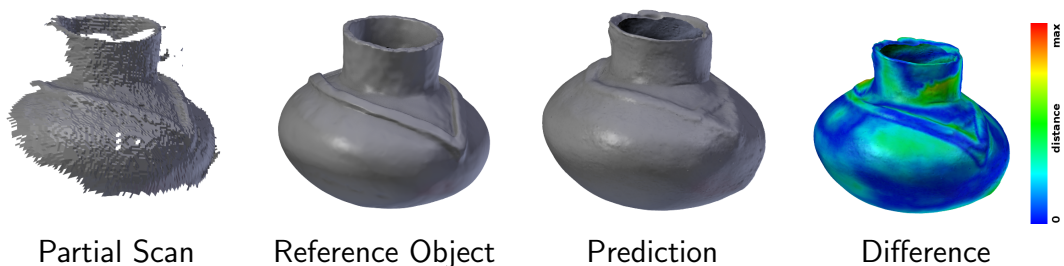


Figure 88: Predictive scanning results on the HM326 object, obtained with Microsoft Kinect V2 for Windows sensor. $RMSE = 3.01mm$.

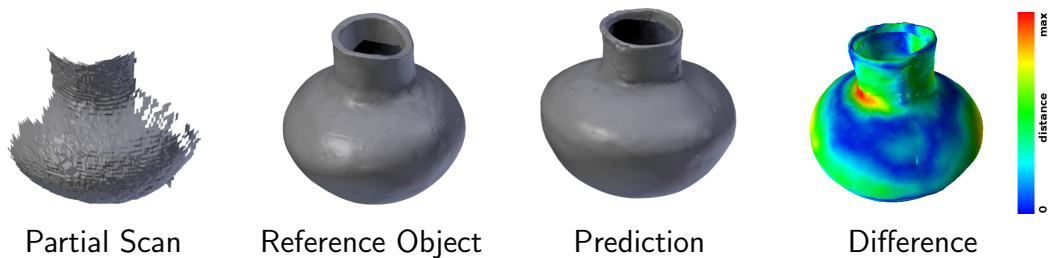


Figure 89: Predictive scanning results on the HM124 object, obtained with Microsoft Kinect V2 for Windows sensor. $RMSE = 3.11mm$.



Figure 90: Predictive scanning results on the HM438 object, obtained with Microsoft Kinect V2 for Windows sensor. RMSE = 6.95mm.

References

- [AIC15] AICON 3D SYSTEMS: <http://aicon3d.com/start.html>, 2015.
- [AMM12] ALDEN M., MELICH G., MUSETH K.: Efficient and Seamless Volumetric Fracturing. *SIGGRAPH Talk* (2012).
- [APM15] ANDREADIS A., PAPAIOANNOU G., MAVRIDIS P.: Generalized digital reassembly using geometric registration. *Proc. Digital Heritage* (2015).
- [Ard15] ARDUINO LLC: <http://www.arduino.cc/>, 2015.
- [BK10] BRONSTEIN M. M., KOKKINOS I.: Scale-invariant heat kernel signatures for non-rigid shape recognition. In *Proceedings of the IEEE Computer Society Conference on Computer Vision and Pattern Recognition* (2010), pp. 1704–1711.
- [BM92] BESL P. J., MCKAY N. D.: A method for registration of 3-D shapes. *IEEE Trans. Pattern Anal. Mach. Intell.* 14, 2 (Feb. 1992), 239–256.
- [BR93] BAEDECKER P. A., REDDY M. M.: The erosion of carbonate stone by acid rain: Laboratory and field investigations. *Journal of Chemical Education* 70, 2 (1993), 104–108.
- [CM02] CAO Y., MUMFORD D.: Geometric structure estimation of axially symmetric pots from small fragments. In *In Proc. Signal Processing, Pattern Recognition, and Applications* (2002).
- [CYFW14] CHEN Z., YAO M., FENG R., WANG H.: Physics-inspired adaptive fracture refinement. *ACM Transactions on Graphics* 33 (2014), 1–7.
- [EL99] EFROS A., LEUNG T.: Texture synthesis by non-parametric sampling. In *In International Conference on Computer Vision* (1999), pp. 1033–1038. URL: [ErosionPaper/EfrosLeung1999TextureSynthesisByNonparametricSampling.pdf](#).

- [GB99] GAURI K. L., BANDYOPADHYAY J. K.: Carbonate Stone, Chemical Behaviour, Durability and Conservation. *John Wiley & Sons, Inc.*, 1999. (1999).
- [GBS*15] GREGOR R., BAUER D., SIPIRAN I., PERAKIS P., SCHRECK T.: Automatic 3D object fracturing for evaluation of partial retrieval and object restoration tasks - Benchmark and application to 3D cultural heritage data. In *Eurographics Workshop on 3D Object Retrieval* (2015), Eurographics Association. Peer-reviewed full paper. [doi:10.2312/3dor.20151049](https://doi.org/10.2312/3dor.20151049).
- [KBH06] KAZHDAN M., BOLITHO M., HOPPE H.: Poisson surface reconstruction. *Symposium on Geometry Processing* (2006).
- [MAM14a] MELLADO N., AIGER D., MITRA N. J.: Super 4pcs fast global pointcloud registration via smart indexing. *Computer Graphics Forum* 33, 5 (2014), 205–215.
- [MAM14b] MELLADO N., AIGER D., MITRA N. J.: Super 4pcs fast global pointcloud registration via smart indexing. *Computer Graphics Forum* 33, 5 (2014), 205–215.
- [MAP15a] MAVRIDIS P., ANDREADIS A., PAPAIOANNOU G.: Efficient sparse icp. *Computer Aided Geometric Design* 35–36 (2015), 16–26.
- [MAP15b] MAVRIDIS P., ANDREADIS A., PAPAIOANNOU G.: Fractured Object Reassembly via Robust Surface Registration. In *EG 2015 - Short Papers* (2015), Bickel B., Ritschel T., (Eds.), The Eurographics Association. [doi:10.2312/egsh.20151005](https://doi.org/10.2312/egsh.20151005).
- [MBT*98] MOROPOULOU A., BISBIKOU K., TORFS K., VAN GRIEKEN R., ZEZZA F., MACRI F.: Origin and growth of weathering crusts on ancient marbles in industrial atmosphere. *Atmospheric Environment* 32, 6 (1998), 967–982.
- [MSAP] MAVRIDIS P., SIPIRAN I., ANDREADIS A., PAPAIOANNOU G.: Object completion using k-sparse optimization. *Computer Graphics Forum* 34, 7, 13–21.
- [Rob15] ROBERTSON CGG: <http://www.robertson-cgg.com/>, 2015.
- [SGS14a] SIPIRAN I., GREGOR R., SCHRECK T.: Approximate symmetry detection in partial 3d meshes. *Computer Graphics Forum (proc. Pacific Graphics)* 33 (2014), 131–140.
- [SGS14b] SIPIRAN I., GREGOR R., SCHRECK T.: Approximate Symmetry Detection in Partial 3D Meshes. *Computer Graphics Forum* (2014). [doi:10.1111/cgf.12481](https://doi.org/10.1111/cgf.12481).

- [SMKF04] SHILANE P., MIN P., KAZHDAN M. M., FUNKHOUSER T. A.: The princeton shape benchmark. In *2004 International Conference on Shape Modeling and Applications (SMI)* (2004), pp. 167–178.
- [SOG09] SUN J., OVSJANIKOV M., GUIBAS L.: A Concise and Provably Informative Multi-Scale Signature Based on Heat Diffusion. *Computer Graphics Forum* 28, 5 (July 2009), 1383–1392.
- [Sto97] STOREMYR P.: *The stones of Nidaros: an applied weathering study of Europe's northernmost medieval cathedral*. PhD thesis, Norwegian University of Science and Technology (NTNU), 1997.
- [TSS*11] TAKAYAMA K., SCHMIDT R., SINGH K., IGARASHI T., BOUBEKEUR T., SORKINE O.: GeoBrush: Interactive mesh geometry cloning. *Computer Graphics Forum* 30, 2 (2011), 613–622.
- [Vra05] VRANIC D. V.: DESIRE: a composite 3d-shape descriptor. In *Proceedings of the 2005 IEEE International Conference on Multimedia and Expo, ICME 2005, July 6-9, 2005, Amsterdam, The Netherlands* (2005), pp. 962–965.
- [Y CJ*96] YERRAPRAGADA S., CHIRRA S., JAYNES J., LI S., BANDYOPADHYAY J., GAURI K.: Weathering rates of marble in laboratory and outdoor conditions. *Journal of Environmental Engineering*, 122(9):856–863 (1996).
- [YJCG94] YERRAPRAGADA S., JAYNES J., CHIRRA S., GAURI K.: Rate of weathering of marble due to dry deposition of ambient sulfur and nitrogen dioxides. *Analytical Chemistry*, 66(5):655–659 (1994).